N°d'ordre NNT : **2019LYSEI063**

THESE de DOCTORAT DE L'UNIVERSITE DE LYON
opérée au sein de
l'INSA de Lyon

Ecole Doctorale N° EDA162
(Mécanique, Energétique, Génie Civil, Acoustique)

Spécialité de doctorat : Génie Mécanique

Soutenue publiquement le 05 septembre 2019, par :

Yuanyuan ZHANG

Friction Prediction for Rough Surfaces in an Elastohydrodynamically Lubricated Contact

---

Devant le jury composé de :

CAYER-BARRIOZ	Juliette	Directrice de recherche CNRS ECL	Présidente
EVANS	Pwt	Professeur Cardiff University	Rapporteur
KŘUPKA	Ivan	Professeur Brno University of Technology	Rapporteur
VENNER	Cornelis. H	Professeur University of Twente	Examinateur
BIBOULET	Nans	Maître de Conférences INSA Lyon	Examinateur
LUBRECHT	Antonius. A	Professeur INSA Lyon	Directeur de thèse

Département FEDORA – INSA Lyon - Ecoles Doctorales – Quinquennal 2016-2020

SIGLE	ECOLE DOCTORALE	NOM ET COORDONNEES DU RESPONSABLE
CHIMIE	**CHIMIE DE LYON** **http://www.edchimie-lyon.fr** Sec. : Renée EL MELHEM Bât. Blaise PASCAL, 3e étage **secretariat@edchimie-lyon.fr** INSA : R. GOURDON	M. Stéphane DANIELE Institut de recherches sur la catalyse et l'environnement de Lyon IRCELYON-UMR 5256 Équipe CDFA 2 Avenue Albert EINSTEIN 69 626 Villeurbanne CEDEX **directeur@edchimie-lyon.fr**
E.E.A.	**ÉLECTRONIQUE, ÉLECTROTECHNIQUE, AUTOMATIQUE** **http://edeea.ec-lyon.fr** Sec. : M.C. HAVGOUDOUKIAN **ecole-doctorale.eea@ec-lyon.fr**	M. Gérard SCORLETTI École Centrale de Lyon 36 Avenue Guy DE COLLONGUE 69 134 Écully Tél : 04.72.18.60.97 Fax 04.78.43.37.17 **gerard.scorletti@ec-lyon.fr**
E2M2	**ÉVOLUTION, ÉCOSYSTÈME, MICROBIOLOGIE, MODÉLISATION** **http://e2m2.universite-lyon.fr** Sec. : Sylvie ROBERJOT Bât. Atrium, UCB Lyon 1 Tél : 04.72.44.83.62 INSA : H. CHARLES **secretariat.e2m2@univ-lyon1.fr**	M. Philippe NORMAND UMR 5557 Lab. d'Ecologie Microbienne Université Claude Bernard Lyon 1 Bâtiment Mendel 43, boulevard du 11 Novembre 1918 69 622 Villeurbanne CEDEX **philippe.normand@univ-lyon1.fr**
EDISS	**INTERDISCIPLINAIRE SCIENCES-SANTÉ** **http://www.ediss-lyon.fr** Sec. : Sylvie ROBERJOT Bât. Atrium, UCB Lyon 1 Tél : 04.72.44.83.62 INSA : M. LAGARDE **secretariat.ediss@univ-lyon1.fr**	Mme Emmanuelle CANET-SOULAS INSERM U1060, CarMeN lab, Univ. Lyon 1 Bâtiment IMBL 11 Avenue Jean CAPELLE INSA de Lyon 69 621 Villeurbanne Tél : 04.72.68.49.09 Fax : 04.72.68.49.16 **emmanuelle.canet@univ-lyon1.fr**
INFOMATHS	**INFORMATIQUE ET MATHÉMATIQUES** **http://edinfomaths.universite-lyon.fr** Sec. : Renée EL MELHEM Bât. Blaise PASCAL, 3e étage Tél : 04.72.43.80.46 **infomaths@univ-lyon1.fr**	M. Luca ZAMBONI Bât. Braconnier 43 Boulevard du 11 novembre 1918 69 622 Villeurbanne CEDEX Tél : 04.26.23.45.52 **zamboni@maths.univ-lyon1.fr**
Matériaux	**MATÉRIAUX DE LYON** **http://ed34.universite-lyon.fr** Sec. : Stéphanie CAUVIN Tél : 04.72.43.71.70 Bât. Direction **ed.materiaux@insa-lyon.fr**	M. Jean-Yves BUFFIÈRE INSA de Lyon MATEIS - Bât. Saint-Exupéry 7 Avenue Jean CAPELLE 69 621 Villeurbanne CEDEX Tél : 04.72.43.71.70 Fax : 04.72.43.85.28 **jean-yves.buffiere@insa-lyon.fr**
MEGA	**MÉCANIQUE, ÉNERGÉTIQUE, GÉNIE CIVIL, ACOUSTIQUE** **http://edmega.universite-lyon.fr** Sec. : Stéphanie CAUVIN Tél : 04.72.43.71.70 Bât. Direction **mega@insa-lyon.fr**	M. Jocelyn BONJOUR INSA de Lyon Laboratoire CETHIL Bâtiment Sadi-Carnot 9, rue de la Physique 69 621 Villeurbanne CEDEX **jocelyn.bonjour@insa-lyon.fr**
ScSo	**ScSo*** **http://ed483.univ-lyon2.fr** Sec. : Véronique GUICHARD INSA : J.Y. TOUSSAINT Tél : 04.78.69.72.76 **veronique.cervantes@univ-lyon2.fr**	M. Christian MONTES Université Lyon 2 86 Rue Pasteur 69 365 Lyon CEDEX 07 **christian.montes@univ-lyon2.fr**

*ScSo : Histoire, Géographie, Aménagement, Urbanisme, Archéologie, Science politique, Sociologie, Anthropologie

Abstract

The friction of interfacial surfaces greatly influences the performance of mechanical elements. Friction has been investigated experimentally in most studies. In this work, the friction is predicted by means of numerical simulation under an elastohydrodynamic lubrication (EHL) rough contact condition.

The classical Multigrid technique performs well in limiting computing time and memory requirements. However, the coarse grid choice has an important influence on code robustness and code efficiency to solve the rough problem. In the first part of this work, a coarse grid construction method proposed by Alcouffe et al. is implemented in the current time-independent EHL Multi-Grid code. Then this modified solver is extended to transient cases to solve the rough contact problem.

The friction curve is usually depicted as a function of "Λ ratio", the ratio of oil film thickness to root-mean-square of the surface roughness. However this parameter is less suitable to plot friction variations under high pressure conditions (piezoviscous elastic regime). In the second part of this work, the friction coefficient is computed using the modified EHL code for many operating conditions as well as surface waviness parameters. Simulation results show that there is no single friction curve when the old parameter "Λ ratio" used. Based on the Amplitude Reduction Theory, a new scaling parameter depends on operating condition and waviness parameters is found, which can give a unified friction curve for high pressure situation.

For more complex rough surfaces, a power spectral density (PSD) based method is proposed to predict friction variations in the third part of this work. The artificial surface roughness is employed to test the rapid prediction method firstly. Good agreement is found between the full numerical simulation and this rapid prediction. Then the rapid prediction method is applied to analyze the friction variation of measured surface roughness. A comparison is also made between predictions and experiments.

Both the new scaling parameter and the friction increase predicted by the PSD method show good engineering accuracy for practical use.

Keywords: *Elastohydrodynamic lubrication, Numerical simulation, Piezoviscous elastic regime, Amplitude Reduction Theory, Friction variation*

Résumé

Le frottement à l'interface des surfaces influence les performances des éléments mécaniques. Le frottement a été étudié expérimentalement dans la plupart des études. Dans ce travail, le frottement est prédit à l'aide d'une simulation numérique dans des conditions de contact rugueux avec une lubrification élastohydrodynamique (EHL).

La technique classique Multigrille fonctionne bien pour limiter le temps de calcul et les besoins en mémoire. Cependant, le choix de la grille grossière a une influence importante sur la robustesse du code et son efficacité pour résoudre le problème brut. Dans la première partie de ce travail, une méthode de construction de grille grossière proposée par Alcouffe et al. est implémenté dans le code EHL Multigrille indépendamment du temps. Ensuite ce solveur modifié est étendu aux cas transitoires pour résoudre le problème de contact avec rugosité.

La courbe de frottement est généralement représentée en fonction du « Λ ratio », le rapport entre l'épaisseur du film d'huile et la valeur moyenne quadratique de la rugosité de la surface. Cependant, ce paramètre est moins approprié pour tracer les variations de frottement dans des conditions de haute pression (régime élasto piézo-visqueux). Dans la deuxième partie de ce travail, le coefficient de frottement est calculé à l'aide du code EHL modifié pour de nombreuses conditions de fonctionnement ainsi que pour les paramètres d'ondulation de surface. Les résultats de la simulation montrent qu'il n'y a pas de courbe de frottement unique lorsque l'ancien paramètre « Λ ratio » est utilisé. En se basant sur la théorie de la réduction d'amplitude, un nouveau paramètre de dimensionnement qui dépend des conditions de fonctionnement et des paramètres d'ondulation est trouvé, ce qui peut donner une courbe de frottement unique pour les situations de haute pression.

Pour les surfaces rugueuses plus complexes, une méthode basée sur la densité spectrale de puissance (PSD) est proposée pour prédire les variations de frottement dans la troisième partie de ce travail. La rugosité artificielle de la surface est utilisée pour tester d'abord la méthode de prédiction rapide. Un bon accord est trouvé entre la simulation numérique complète et cette prédiction rapide. La méthode de prédiction rapide est ensuite appliquée pour analyser la variation de frottement de la rugosité de surface mesurée. Une comparaison est également faite entre les prédictions et les expériences.

Le nouveau paramètre d'échelle et l'augmentation du frottement prédite par la méthode PSD montrent une bonne précision technique pour une utilisation pratique.

Mots clés: *Lubrification élastohydrodynamique, Simulation numérique, Régime élasto piézo-visqueux, Théorie de réduction d'amplitude, Variation de frottement*

Contents

List of Figures

List of Tables

Nomenclature

A_d	dimensionless deformed amplitude in the center of the contact	
A_i	dimensionless initial amplitude	
a_h	the radius of the contact area $a_h = \sqrt[3]{3wR_x/(2E')}$	m
C^{2D}	2d power spectral density	m^4
C^{iso}	2d power spectral density of an isotropic surface	m^4
E_1, E_2	elastic moduli of the two contact bodies	Pa
E'	reduced modulus of elasticity $2/E' = (1-\upsilon_1^2)/E_1 + (1-\upsilon_2^2)/E_2$	Pa
f	the friction force induced by the shearing of the lubricant	N
F	the dimensionless friction force	
G	dimensionless material parameter $G = \alpha E'$	
G_e	elastic shear modulus	Pa
G_∞	the limiting elastic shear modulus	Pa
h	film thickness	m
H	dimensionless film thickness $H = hR_x/a_h^2$	
h_0	mutual approach	m
H_0	dimensionless mutual approach	
h_c	central film thickness	m
Hc	dimensionless central film thickness for a smooth case $Hc = h_c R_x/a_h^2$	
Hc_{rough}	dimensionless central film thickness for a rough case	
hx, hy	dimensionless mesh sizes on the fine grid	
Hx, Hy	dimensionless mesh sizes on the coarse grid	
I_H^h	interpolation operator	
I_h^H	restriction operator	
L_x, L_y	lengths of final topography	m
L^l	coarse grid operator on the lth level	
L	dimensionless material parameter (Moes) $L = G(2U)^{0.25}$	
M	2d dimensionless load parameter (Moes) $M = W_2(2U)^{-0.75}$	

p	pressure	Pa
p_s	pressure for smooth cases	Pa
p_h	Hertzian pressure	Pa
δp	pressure fluctuations	Pa
ΔP	dimensionless pressure fluctuations $\Delta P = \delta p / p_h$	
q_x, q_y	wavenumbers in x and y directions respectively	1/m
q_r	roll-off wavenumber	1/m
R_q	root mean square of the surface roughness	m
R_x	reduced radius of curvature in x : $1/R_x = 1/R_{1x} + 1/R_{2x}$	m
R_y	reduced radius of curvature in y : $R_y = R_x$	m
r	wavelength ratio used to describe the surface anisotropy $r = \lambda_x / \lambda_y$	
rr	undeformed surface roughness	m
rr^d	deformed surface roughness	m
RR	dimensionless surface roughness $RR = rr \cdot R_x / a_h^2$	
SRR	slide to roll ratio	
t	time	s
T	dimensionless time $T = t\bar{u}/a_h$	
ΔT	dimensionless time step	
u_1, u_2	velocities of lower surface and upper surface respectively	m/s
u_r	mean velocity of contact surfaces $u_r = 0.5 \times (u_1 + u_2)$	m/s
U	dimensionless speed parameter $U = (\eta_0 u_r)/(E' R_x)$	
ΔU	slide-to-roll ratio $\Delta U = \delta u / u_r = (u_1 - u_2)/u_r$	
U_{rat}	slip parameter $U_{\mathrm{rat}} = u_1 / u_r$	
v_1, v_2	Poisson ratios of the two contact bodies	
w	normal load	N
W_2	2d dimensionless load parameter $W_2 = w/(E' R_x^2)$	
x	coordinate in the rolling direction	m
X	dimensionless coordinate $X = x/a_h$	
y	coordinate perpendicular to x	m
Y	dimensionless coordinate $Y = y/a_h$	

z	pressure viscosity index	
α	pressure viscosity index	$1/\mathrm{Pa}$
$\bar{\alpha}$	dimensionless viscosity index $\bar{\alpha} = \alpha p_h$	
τ	shear stress induced by the shearing of the lubricant	Pa
τ_0	the Eyring stress	Pa
τ_L	the limiting shear stress	Pa
∇_2	dimensionless wavelength parameter $\nabla_2 = (\lambda/a_h)\sqrt{M/L}$	
$\bar{\lambda}$	dimensionless speed parameter	
λ_t	the time constant for the fluid	
λ_x, λ_y	wavelength in x, y direction	m
η	viscosity	$\mathrm{Pa \cdot s}$
η_0	the atmospheric viscosity	$\mathrm{Pa \cdot s}$
$\bar{\eta}$	dimensionless viscosity $\bar{\eta} = \eta/\eta_0$	
ρ	density of the lubricant	$\mathrm{Kg \cdot m^{-3}}$
ρ_0	atmospheric density of the lubricant	$\mathrm{Kg \cdot m^{-3}}$
$\bar{\rho}$	dimensionless density $\bar{\rho} = \rho/\rho_0$	
θ_2	dimensionless new lambda ratio parameter	
θ_2^*	dimensionless new lambda ratio parameter for purely longitudinal rough surfaces	
$\dot{\gamma}$	strain rate	$1/\mathrm{s}$
μ	friction coefficient	
σ	standard deviation of surface roughness	m

Abbreviations

ART	Amplitude Reduction Theory
EHL	Elastohydrodynamic Lubrication
FFT	Fast Fourier Transform
PSD	Power Spectral Density

Superscripts

d	deformed
h	the fine grid
H	the coarse grid

iso	isotropic
l	the lth level

Subscripts

a, b	inlet, outlet
i, d	initial, deformed
r, s	rough, smooth
st	start
x, y	space domain
q_x, q_y	frequency domain

Chapter 1

Introduction

Contents

1.1 Background

Energy is the most important of all resources, which is needed to support economic and social progress and build a better quality of life. According to the report of IEEJ Outlook 2019 (Institute of Energy Economics, Japan), the world primary energy consumption will continue growing from 2018 to 2050. Most of this growth comes from non-OECD (non-Organization for Economic Cooperation and Development) countries, where demand is driven by strong economic growth (shown in Figure 1.1). Fossil energy like oil, coal and natural gas are still the largest energy source of the world, and the reserves of fossil energy are limited. Meanwhile, the over-consumption of fossil fuel leads to the over-release of carbon dioxide (CO_2), methane, oxynitride (NO_x) and particulates into the air, which disturb the natural balance of the atmosphere. The rapid rise in the carbon dioxide contributes to the serious global warming problem. NASA (National Aeronautics and Space Administration) reported that the global surface temperature has been persistently increasing since the late 19th century (shown in Figure 1.2). An investigation from the U.S. Energy Information Administration (EIA) shows that the industrial and transportation sectors have consumed the most energy (shown in Figure 1.3) as well as produced the most CO_2 emissions (show as Table 1.1).

However, a substantial amount of energy is not put to useful purposes. Researches [1–4] show that a considerable amount of energy in industrial and transportation is consumed to overcome friction. For instance, energy consumed to overcome friction over the total energy consumption in heavy-duty vehicles is 33%, in paper machines is 32%, in passenger cars is 33% and in mineral mining industry is 40%. Recently, the increasing environment awareness requires efforts to improve energy efficiency and reduce CO_2 production. Correct lubrication between engineering provides sufficient separation of the roughness present on the contact surfaces, which contributes to reducing friction losses. Better understanding and control of friction in mechanical components has the potential to offset large energy savings and CO_2 emission reduction [5]. Studies [6–8] estimated that with the implementing advanced tribological technologies, such as using new contact surface, materials, lubricants, energy losses due to friction and wear could potentially be reduced by 40% in the long term (15 years) and by 18% in the short term (8 years)and CO_2 emissions globally can also reduced by 1,460 $MtCO_2$ (million tonnes CO_2) in the short term and by 3,140 $MtCO_2$ in the long term.

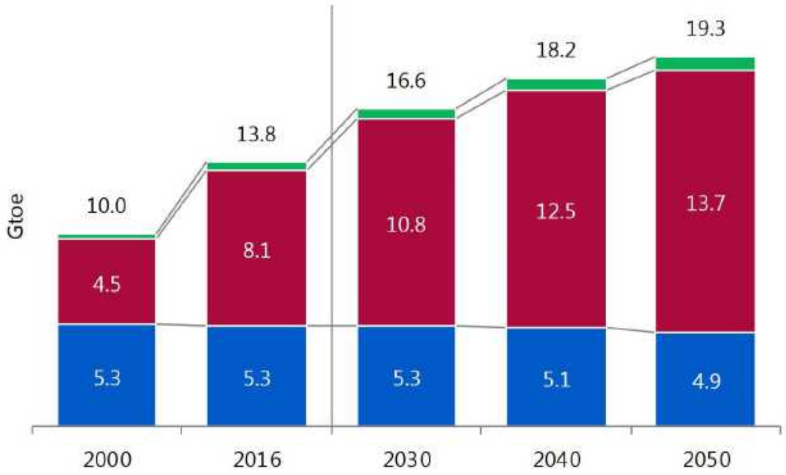

Figure 1.1: World primary energy consumption (red column: Non-OECD, blue column: OECD). (Source: IEEJ Outlook 2019 and Scenario)

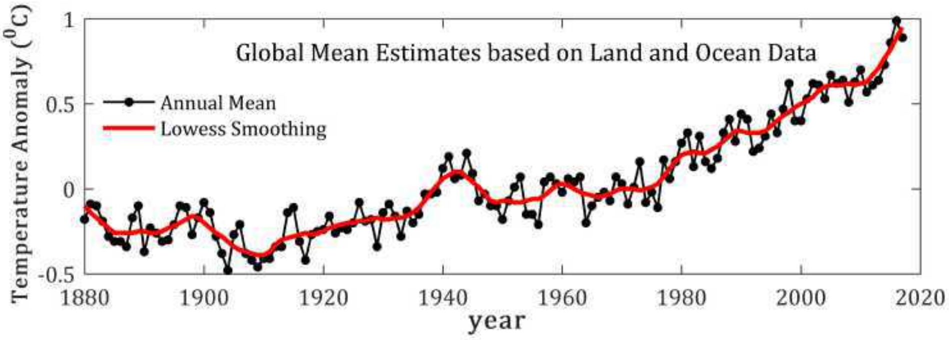

Figure 1.2: The variation of mean global surface temperature relative to 1880-2017. (Source: NASA/GISS)

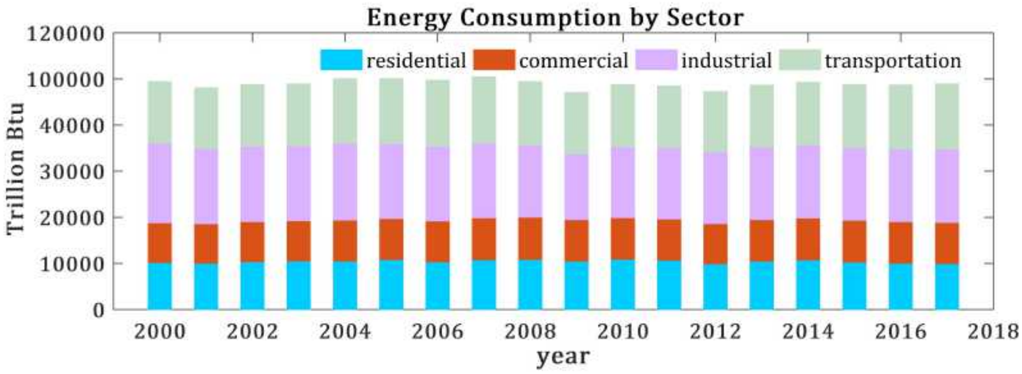

Figure 1.3: Total consumption by End-Use Sector, from 2000 to 2017. (Source: Data from the U.S. Energy Information Administration)

Hence, understanding the mechanisms of friction and improving frictional behavior between engineering contact surfaces still remains an important issue in today's research, not only for meeting the increasing requirements of energy efficiency and CO_2 emissions reduction but also for providing a theoretical tool in element design and optimization.

Table 1.1: U.S. CO_2 emissions from end-use sectors, 2008-2017. (Source: U.S. Energy Information Administration, August 2018 Monthly Energy Review)

Units: million metric tons

	year									
end-use sector	2008	2009	2010	2011	2012	2013	2014	2015	2016	2017
transportation	1898	1832	1848	1817	1779	1805	1823	1848	1886	1902
industrial	1608	1400	1508	1498	1489	1508	1511	1456	1428	1409
residential	1234	1127	1210	1149	1043	1100	1115	1037	982	956
commercial	1075	1007	1025	990	932	958	970	932	894	875

1.2 Literature review

Elastohydrodynamic lubrication (EHL) is the type of lubrication for frictional pairs having elastic contact under very high pressure and forming lubricant film in non-conformal contacts, such as rolling bearings, gears, human synovial joints and so on [9]. Lubricant film and surface roughness play an important role for improving reliability and effectiveness of mechanical parts as well as reducing friction losses. The majority of the published work on the influence of surface roughness on friction has been experimental, the minority of theoretical work has been done on friction prediction. This section represents the literature review on the methods to solve the rough EHL contact problem as well as friction in rough EHL contacts.

1.2.1 Methods to solve the rough contact problem

Typically, the EHL model consists of five equations [10], in which the Reynolds equation Equation 1.1 is a partial differential equation and the film thickness equation Equation 1.2 contains an integral term, both equations are required to be solved simultaneously, making these equations very complex. There are many approaches that can be used to solve this EHL model: the inverse method [11], the Newton-Raphson method [12], the homotopy method [13], the finite element method [14], the Multigrid method [15,16] and the Navier-Stokes approach [17]. So far, the Multigrid algorithm has been considered as one of the most efficient methods and applied frequently to EHL problems.

$$\frac{\partial}{\partial x}\left(\frac{\rho h^3}{12\eta}\frac{\partial p}{\partial x}\right)+\frac{\partial}{\partial y}\left(\frac{\rho h^3}{12\eta}\frac{\partial p}{\partial y}\right)-u_r\frac{\partial(\rho h)}{\partial x}=0 \tag{1.1}$$

$$h(x,y)=h_0+\frac{x^2}{2}+\frac{y^2}{2}-rr(x,y)+\frac{2}{\pi^2}\int_{-\infty}^{+\infty}\int_{-\infty}^{+\infty}\frac{P(x',y')}{\sqrt{(x-x')^2+(y-y')^2}}dx'dy' \tag{1.2}$$

Where p represents the pressure, h denotes the film thickness, h_0 is the mutual approach and $u_r = (u_2 + u_2)/2$ is the mean velocity of two contact surfaces. ρ and η are the density and viscosity of the lubricant, respectively. The x axis is aligned with the direction of the mean velocity $\bar{u}$, and the y axis is perpendicular to the x direction.

In engineering, no surface is perfectly smooth, the order of magnitude of the surface roughness is often the same as or greater than that of the film thickness predicted by smooth contact conditions [18]. Therefore, the surface roughness should be considered. Generally, there are two methods to treat the rough lubrication problem numerically.

One approach is called the "stochastic" method. Early work was conducted on the hydrodynamic lubrication (HL) problem. Theoretical analysis of the implementation of the stochastic theory on rough HL contact problem was described by Christensen [19, 20]. Then Patir and Cheng [21, 22] proposed an average flow model to determine the effects of surface roughness on rough-lubricated contacts. In this model the Reynolds equation is simplified as an average Reynolds equation using a independent flow factor (shown in Figure 1.4). Since the pioneering studies on the "average flow model", a number of authors have extended and generalized this work. Tripp [23] re-computed the flow factors using a perturbation expansion of the pressure in a nominal parallel film. When small roughness amplitude is considered, the flow factors calculated in Reference [23] agree well with that of Patir and Cheng [21]. Hu and Zheng [24] studied the influence of boundary conditions, grid systems and statistics of rough surfaces on the flow factors. Lunde and Tonder [25] calculated the flow factors for an isotropic rough bearing and found that the boundary conditions of the selected bearing part can not affect the flow passing through. Subsequently, Zhu and Cheng [26] extended the flow factors method in the point EHL contact problem. Some authors [27, 28] applied the flow factors to deal with the cavitation problem. Letalleur et al. [29] studied the flow factors for two rough cases: smooth-rough stationary case and rough-rough unstationary case. Sahlin et al. [30] developed a novel method using a homogenization technique to compute the flow factors. However, in stochastic model, roughness asperities are mainly treated as rigid.

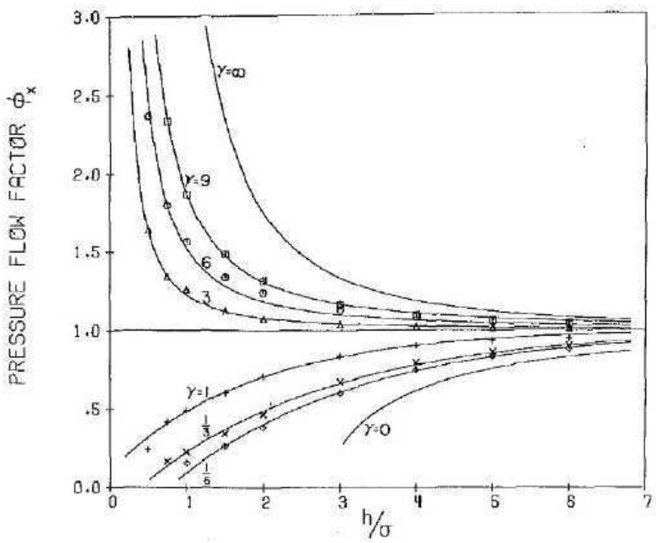

Figure 1.4: Pressure flow factors. (Source: Reference [21])

Another way is to incorporate the surface roughness term $rr(x, y, t)$ in the film thickness equation (shown as Equation 1.2) and to solve the system of equations directly. Due to the limitation of computation of speed and storage space, preliminary research [31–35] studied the steady state line rough contact problem, where the surface roughness is time-independent and one-dimensional model was considered. Later on, the stationary two dimensional rough contact problem [36–39] were carried out. With the increasing development of computational technique, transient cases were studied by many authors [40–51]. Based on the previous studies on transient rough contact problem, Venner and Lubrecht et al. [52–60] published a series of papers on the "Amplitude Reduction Theory" describing the relation between the surface roughness deformation and operating conditions. They found that under very high pressure situations (piezoviscous elastic regime), the surface roughness will deform, and this deformation depends on operating conditions. A master curve (shown in Figure 1.5) describes this relation quantitatively. Then Šperka et al. [61] verified the "Amplitude Reduction Theory" by measuring the deformed surface roughness on an optical test rig, the comparison of the measured results and the predicted results can be found in Figure 1.6. Recently, some extension work on the rough contact problem were addressed [62–65]. One of the most important studies about the influence of surface roughness on friction will be represented in the next subsection.

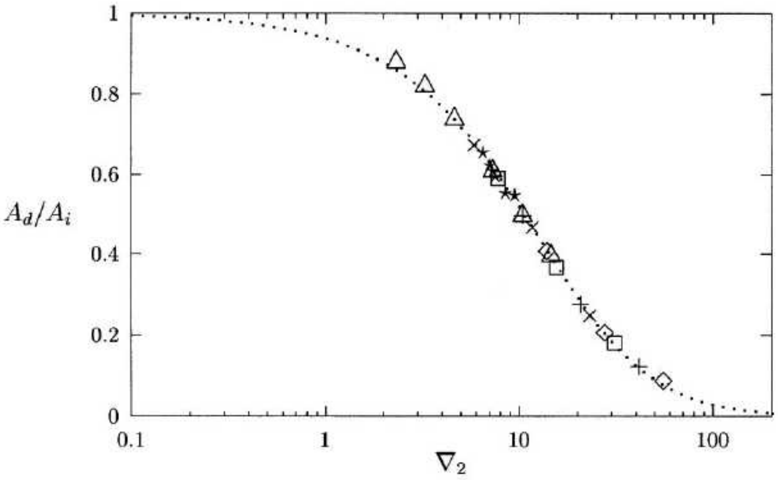

Figure 1.5: Relative amplitude as a function of ∇_2 under pure rolling, where ∇_2 is dimensionless wavelength parameter, A_i and A_d are amplitude of surface roughness and deformed surface roughness respectively. (Source: Reference [58])

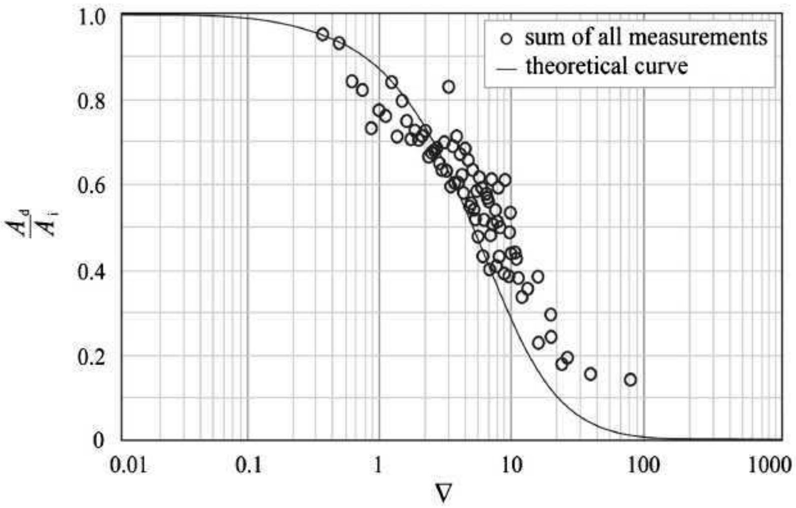

Figure 1.6: Results obtained from measurements compared with theoretical attenuation curve defined by [56]. (Source: Reference [61])

The surface roughness term $rr(x, y)$, which is often considered to be the same order of magnitude as the oil film thickness, incorporated in Equation 1.2 makes the coefficient $(\rho h^3)/(12\eta)$ in the Reynolds equation jump orders of magnitude, which leads to a significant variation in EHL equations. From a mathematical point of view, the coefficient $(\rho h^3)/(12\eta)$ is continuous, while in the numerical simulation, the coefficient causes a strong discontinuity in discrete

Reynolds equation. Work by Alcouffe et al [66] proposed an efficient way to overcome the above discontinuity through constructing the coarse grid in a Multi-grid code. The present work employs the Multigrid techniques [10] to solve the rough contact problem. In addition, the idea provided by Alcouffe et al [66] is also applied to improve the code robustness and code efficiency.

1.2.2 Friction in rough EHL contact problem

Most heavily loaded machine elements are working under elastohydrodynamically lubricated conditions. Understanding the frictional behavior in such contacts plays an important role for reducing friction, preventing wear as well as improving service life. To reveal the relation between fluid properties and friction, research has been conducted as follows: Crook [67] used a disc machine for measuring frictional traction. It was shown that the rolling friction (the traction due to rolling) is independent of load and simply proportional to the film thickness in the elasto-hydrodynamic regime. Johnson and Cameron [68] measured traction in a rolling contact disc machine and results showed that the traction first increases and then decreases when the sliding speed increases. Johnson and Roberts [69] observed the visco-elastic behavior of film thickness through measuring shear forces on a rolling-contact test rig. Evans and Johnson [70] constructed traction maps depending upon pressure, temperature as well as shear rate for different fluids, where different areas represent different traction behavior. Zhang et al. [71] studied the elliptical contact between rib face and roller end in tapered roller bearings by means of a full numerical simulation. They found that the elastic deformation has a non-negligible influence on the friction coefficient. Yu and Medley [72] studied the influence of lubricant additives on friction via a side-slip disc machine. They concluded that the limiting shear stress, which is a useful parameter for predicting friction, is affected by the lubricant additives. Jacod et al. [73] predicted the coefficient of friction over a wide range of operating conditions and obtained a single generalized friction curve based on a full numerical simulation for a non-Newtonian EHL contact model. Vicente et al. [74] explored friction in rolling-sliding, soft-EHL contacts numerically and experimentally. Numerical calculations of the Couette friction are in good agreement with measured results. Very recently, Liu et al [75] calculated the friction coefficient in a gear contact interface numerically, based on a thermal starved EHL model. They found that the maximum friction coefficient appears at the engaging-in point where a considerable slide-to-roll ratio exists. Björling et al. [76] measured the friction under EHL conditions on a ball-on-disc test rig for aged and fresh oils. Results showed that there is no difference in friction. In addition, Zhang [77] measured the EHL friction for a wide range of base fluids and compared the friction values for five different operating conditions. The study underlined the importance of molecular structure of the base fluid in determining the EHL friction.

Studies [78–80] showed that surface roughness has a significant impact on the friction behavior of lubricated surfaces. A useful tool to investigate the frictional behavior between rough surfaces is the classical Stribeck curve, showing the friction coefficient is a function of a ratio of the averaged oil film thickness to the combined surface roughness. The original research about the Stribeck curve dates back to the 19th century. In 1879, Thurston gave precise values of the friction coefficient and he was probably the first person to report that the friction coefficient passed through a minimum as the load increased [81, 82]. Twenty years later, Stribeck [83, 84] systematically published results of a carefully conducted and wide-ranging series of experiments on journal bearings, which are frequently referred to as 'the Stribeck curve' (shown in Figure 1.7). G$\ddot{u}$mbel [85] organised Stribeck's experimental results in a single curve by plotting the friction against the parameter $\eta\omega/\bar{p}$, where η is the lubricant viscosity, ω is the angular velocity of the shaft and $\bar{p}$ is the load per unit length. At the same time, Hersey [86] conducted experiments on journal bearings and plotted the friction coefficient against the load, speed, temperature, viscosity and rate of oil supply. He showed that hydrodynamic friction should be a function of $\eta n/p$ in which n is the rotational speed and p is the pressure. Many years later, Wilson and Barnard [87] replotted the Stribeck curve by introducing a new variable i.e. zn/p, where the lower-case z stands for the lubricant viscosity. Subsequently, McKee [88] provided a similar dimensionless group ZN/P. Vogelpohl et al. [89] incorporated the boundary and fluid friction coefficient and showed a transition from the hydrodynamic lubrication regime to the mixed lubrication regime. All of the work mentioned above is performed under low pressure conditions, in the isoviscous rigid regime [90].

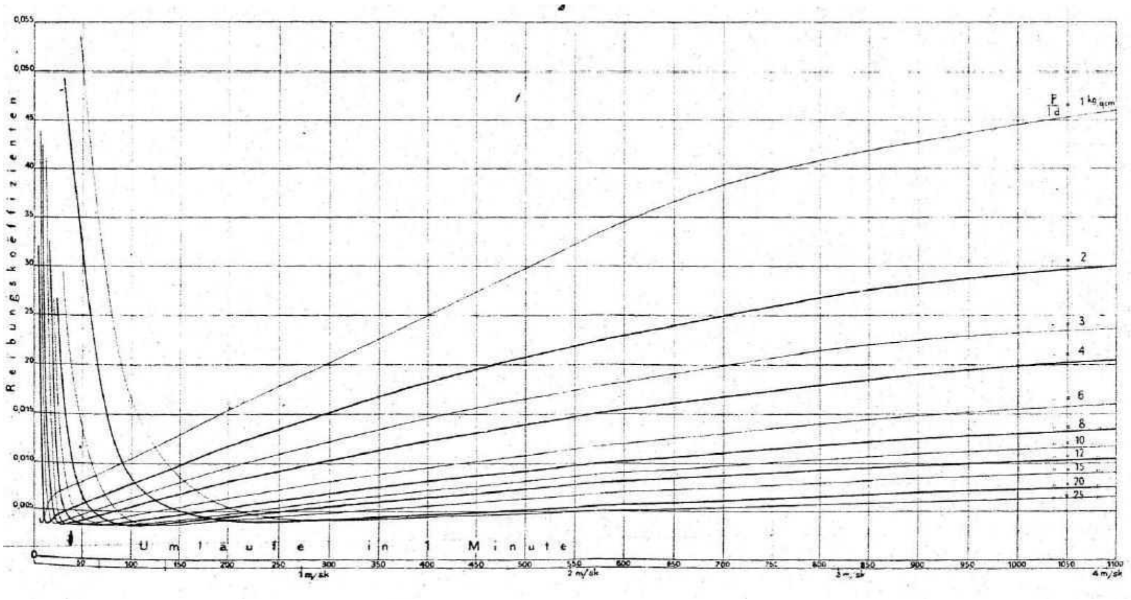

Figure 1.7: Friction coefficient versus speed for different loads. (Source: Ref. [83])

The situation for non-conforming contacts, such as those occurring in rolling element bearings, gears and cams, is somewhat different [91]. Shotter [92] experimentally showed that the friction increases with the surface roughness. Tallian and his co-workers [93, 94] proposed a ratio $|\xi_0|$ between the elastohydrodynamic film thickness and the composite root mean square roughness to represent the mixed elastodydrodynamic regime ($1 < |\xi_0| < 4$). Poon [95] was concerned with the transition from the boundary to the mixed regime with a dimensionless parameter $1 \leqslant \xi \leqslant 2$ and the transition from mixed to full EHL region with $2 < \xi \leqslant 2.4$ by using electrical-conductivity measurements. Bair and Winer [96] plotted the reduced traction coefficient as a function of a lambda ratio by performing sliding-rolling experiments. They found that when the lambda ratios is less than 2 the contact moves into the mixed regime. In general, the Stribeck curve can be divided into three regimes [97]: $\lambda > 3$ represents the full-film regime, $1 \leqslant \lambda \leqslant 3$ is the mixed EHL regime and $\lambda < 1$ indicates the boundary regime. However, study [98] shows that this lambda ratio is not a suitable parameter to determine lubrication states especially when some aspects such as non-Newtonian, thermal and transient effects are considered. Transition locations from mixed to boundary lubrication regime or from full-film to mixed lubrication regime are still ambiguous. Therefore, an appropriate grouping including the speed, film thickness and roughness is required. Schipper [99] suggested a so-called Lubrication number L' , which takes viscosity, speed and pressure into consideration, to detect the variation of the friction coefficient. Recently, Gelinck [100] extended Johnson's model [101] to calculate the coefficient of friction for the whole mixed EHL regime. Lu and Khonsari [102] examined the behavior of the Stribeck curve theoretically and experimentally on a journal bearing and found a good agreement. Wang et al. [103] presented a numerical approach developed on the basis of deterministic solutions of mixed lubrication to evaluate sliding friction. Meanwhile, they measured the sliding friction on a commercial test rig. Both results were plotted against sliding velocities and also showed good agreement. Kalin [104] investigated changes of the Stribeck curve when one or two surfaces in the contact are non-fully wetted. Afterwards, Kalin [105] tested the variations of the friction coefficient with diamond-like carbon coatings (DLC). Zhang [106] developed a numerical approach assuming the asperity interaction friction is proportional to the contact area to predict the mixed EHL friction coefficient. Bonaventure [107] and his co-authors conducted rolling-sliding experiments with random surface roughness, they found that the onset of ML occurs at a higher entrainment product $\eta_0 u_e$ (in which η_0 is inlet viscosity and u_e is entrainment speed) and a relevant roughness scalar parameter was obtained to predict the onset position.

Most of the work on Stribeck curve was done by experiments. Current study employs the Amplitude Reduction Theory [53] to study the frictional behavior in piezoviscous elastic regime [108] by means of numerical simulation.

1.3 Research aims and Outlines

1.3.1 Research aims

Long term successful operation of mechanical devices greatly depends on correct lubrication of the mechanical elements to provide sufficient separation of the roughness present on the contact surfaces. However, lubrication provides another important role, reducing friction between rough contact surfaces.

The objective of the present research project is to develop an efficient and robust Multi-Grid-based algorithm to study the frictional behavior between rough contact surfaces. Current MultiGrid codes show the required efficiency, but are not sufficiently robust to treat the rough surface problem in a general way. Difficulties may lie in the following aspects:

(i) The efficient construction of the coarse grid of EHL Multi-Grid model to guarantee the code robustness and code efficiency of impact, rough surface EHL contact problems.

(ii) Tests of the increased robustness of the new EHL Multi-Grid solver.

(iii) Implementation applied to test the code robustness and code efficiency of rough surface EHL contact problems.

(iv) The extension of the developed Multi-Grid lubrication code to transient contact problems.

(v) The computation of the friction coefficient of rough contact surfaces.

(vi) The unification of friction curves that differ according to operating conditions.

(vii) The extension of the lambda ratio parameter predicting the transition from mixed to full-film regimes.

1.3.2 Outlines

According to the research aims listed in the previous sub-section. The layout of this thesis is as follows:

Chapter 1: This chapter first emphasizes the important role of friction played in energy consumption and environmental issues. Subsequently, a literature review on the methods to solve rough contact problems and friction in rough contact problems is illuminated. The objective and structure of the present thesis are given in the last section.

Chapter 2: This chapter represents the numerical model and algorithm for solving the transient rough EHL contact problem. The governing equations for transient EHL model are introduced first. Then the method proposed by Alcouffe et al [66] is employed to construct transfer operators as well as coarse grid operator. Finally the Multi-Grid method [10] is implemented.

Chapter 3: In this chapter, lubricant rheological models are illustrated in the first place. The relative friction coefficient, an indicator for the full-film-mixed lubrication regime transition, is proposed in methodology section. Then the relative friction coefficient is calculated numerically for isotropic as well as anisotropic harmonic surface roughness respectively. Finally, a single friction curve is obtained using a new "lambda ratio" parameter.

Chapter 4: A rapid analytical prediction method using the power spectral density [109] is proposed to study a more complex surface topography in this chapter, firstly. Then an artificial surface roughness is employed to test this rapid prediction method. Finally, the prediction method is applied to predict friction for measured rough surfaces.

Chapter 5: The main results of current work are summarized and recommendations of future work are also made.

Chapter 2

Numerical model

Contents

2.1 Introduction

Multi-grid methods have been used successfully to treat Elastohydrodynamic lubrication (EHL) problems in the past [110–112]. However, when taking the surface roughness into account, film thickness and viscosity jump violently, both of them are strongly discontinuous parameters in discrete equations and will influence code robustness and code efficiency. The paper by R. Alcouffe [66] proposed an efficient way to solve this problem through constructing the coarse grid in a Multi-grid code. In this chapter, the Multigrid method is applied to solve the transient EHL model, and the algorithm outlined in Reference [66] is also implemented.

2.2 Transient EHL model

2.2.1 Governing equations

The lubrication of rough surfaces in EHL contacts is inherently a highly transient process. Study [40] shows that the surface roughness induced by the transient effect has a remarkable influence on the pressure and film thickness profiles. For the time-dependent problem [10], the Reynolds equation is given as:

$$\underbrace{\frac{\partial}{\partial x}\left(\frac{\rho h^3}{12\eta}\frac{\partial p}{\partial x}\right)+\frac{\partial}{\partial y}\left(\frac{\rho h^3}{12\eta}\frac{\partial p}{\partial y}\right)}_{\text{poiseuille}}-\underbrace{u_r\frac{\partial(\rho h)}{\partial x}}_{\text{couette}}-\underbrace{\frac{\partial(\rho h)}{\partial t}}_{\text{transient}}=0 \tag{2.1}$$

with $p = 0$ on the boundaries and the cavitation condition $p \geqslant 0$ everywhere. Where p is the pressure, h is the film thickness whose expression is shown as Equation 2.2 and $u_r = (u_1 + u_2)/2$ is the mean velocity (u_1 and u_2 are the velocities of two contact surfaces respectively). The direction of the x axis is as same as that of the mean velocity u_r, the y axis is perpendicular to x axis and t is time.

The equation used to describe the gap between the two contact bodies is the film thickness equation:

$$h(x,y,t) = h_0(t) + \frac{x^2}{2R_x} + \frac{y^2}{2R_y} - rr(x,y,t) + \underbrace{\frac{2}{\pi E'}\int_{-\infty}^{+\infty}\int_{-\infty}^{+\infty}\frac{p(x',y',t)}{\sqrt{(x-x')^2+(y-y')^2}}dx'dy'}_{\text{elastic deformation}} \tag{2.2}$$

in which $rr(x,y,t)$ stands for surface roughness. R_x and R_y represent the reduced radius of curvature in x and y direction respectively. h_0 denotes the rigid body approach. E' is called the reduced elastic modulus and its expression can be found below. The elastic deformation term is calculated with the approach named *multilevel multi-integration* [10, 113].

$$\frac{2}{E'} = \frac{1-\upsilon_1^2}{E_1} + \frac{1-\upsilon_2^2}{E_2}$$

and E_1 and E_2 are the elastic moduli of the two contact bodies. υ_1 and u_2 are the Poisson ratios.

In order to have a load balance. The integral of the pressure distribution should be equal to the applied load w.

$$\int_{-\infty}^{+\infty}\int_{-\infty}^{+\infty} p(x',y',t)dx'dy' = w(t) \tag{2.3}$$

In the Reynolds equation (2.1), ρ is the density and η is the viscosity of the lubricant. Both of them are functions of pressure. A simply density pressure relation is given by Dowson and Higginson [114]:

$$\rho(p) = \rho_0 \frac{5.9\times10^8 + 1.34p}{5.9\times10^8 + p} \tag{2.4}$$

where ρ_0 is the atmospheric density. The simplest viscosity pressure relation is proposed by Barus [115]:

$$\eta(p) = \eta_0 \exp(\alpha p) \tag{2.5}$$

in which η_0 is the atmospheric viscosity and α is the pressure viscosity coefficient. However, this exponential Barus equation usually predicts a higher viscosity value when the pressure is very large. A more realistic relation is derived by Roelands [116]:

$$\eta(p) = \eta_0 \exp[(\ln(\eta_0) + 9.67)(-1 + (1 + \frac{p}{p_0})^z)] \tag{2.6}$$

where η_0 is the atmospheric viscosity and z is the pressure viscosity index, typically $z = 0.6$ and $p_0 = 1.98\times10^8$ Pa.

2.2.2 Dimensionless equations and parameters

To simplify the equation system and generalize the EHL model, the equations described above are made dimensionless using dimensionless variables based on the Hertzian dry contact solution [117]. For the dry point contact case, the pressure distribution profile required for contact deformation reads:

$$p(x,y) = \begin{cases} p_h\sqrt{1-(x/a_h)^2-(y/a_h)^2} & \text{if } x^2+y^2 \le a_h^2 \\ 0 & \text{otherwise} \end{cases} \tag{2.7}$$

with a_h the radius of the contact area:

$$a_h = \sqrt[3]{\frac{3wR_x}{2E'}} \tag{2.8}$$

and p_h is referred to as the *Hertzian pressure*:

$$p_h = \frac{3w}{2\pi a_h^2}. \tag{2.9}$$

Then the dimensionless variables are introduced to simplify the EHL model:

$$\boxed{\begin{array}{ll} X = x/a_h & Y = y/a_h \\ P = p/p_h & H = hR_x/a_h^2 \\ \bar{\eta} = \eta/\eta_0 & \bar{\rho} = \rho/\rho_0 \\ T = u_r t/a_h & \bar{\alpha} = \alpha p_h \end{array}} \tag{2.10}$$

Substituting the dimensionless variables in Equation 2.1 yields:

$$\frac{\partial}{\partial X}\left(\frac{\bar{\rho}H^3}{\bar{\eta}\bar{\lambda}}\frac{\partial P}{\partial X}\right) + \frac{\partial}{\partial Y}\left(\frac{\bar{\rho}H^3}{\bar{\eta}\bar{\lambda}}\frac{\partial P}{\partial Y}\right) - \frac{\partial(\bar{\rho}H)}{\partial X} - \frac{\partial(\bar{\rho}H)}{\partial T} = 0 \tag{2.11}$$

with $X \in [X_a, X_b]$ and $Y \in [-Y_a, Y_a]$. Where $\bar{\lambda} = (12u_r\eta_0 R_x^2)/(a^3 p_h)$. And the boundary conditions are $P(X_a, Y_a) = P(X_a, Y) = P(X_b, Y) = P(X, Y_a) = P(X, -Y_a) = 0$. The cavication condition is $P(X, Y, T) \geq 0$.
The dimensionless film thickness equation becomes:

$$H(X,Y,T) = H_0(T) + \frac{X^2}{2} + \frac{Y^2}{2} - RR(X,Y,T) + \frac{2}{\pi^2}\int_{-\infty}^{+\infty}\int_{-\infty}^{+\infty}\frac{P(X',Y',T)}{\sqrt{(X-X')^2+(Y-Y')^2}}dX'dY' \tag{2.12}$$

where $H_0(T)$ is determined by the dimensionless force balance equation:

$$\int_{-\infty}^{+\infty}\int_{-\infty}^{+\infty} P(X',Y',T)dX'dY' = \frac{2\pi}{3} \tag{2.13}$$

The dimensionless density equation for a compressible lubricant reads:

$$\bar{\rho}(P) = \frac{5.9\times 10^8 + 1.34 p_h P}{5.9\times 10^8 + p_h P} \tag{2.14}$$

The dimensionless forms of viscosity equations are:

$$\textit{Barus:} \qquad \bar{\eta} = \exp(\bar{\alpha}P) \tag{2.15}$$

and

$$\textit{Roelands:} \qquad \bar{\eta} = \exp((\ln(\eta_0) + 9.67)(-1 + (1 + \frac{p_h}{p_0}P)^z)). \tag{2.16}$$

Beside the dimensionless variables mentioned in Equation 2.10, two dimensionless numbers are often used to reduce the number of parameters, they are referred as Moes dimensionless parameters [118, 119]. For point contact they are defined as [119]:

$$M = \frac{w}{E'R_x^2}\left(\frac{2\eta_0 u_r}{E'R_x}\right)^{-3/4} \tag{2.17}$$

and

$$L = \alpha E'(\frac{2\eta_0 u_r}{E' R_x})^{1/4}. \tag{2.18}$$

For convenience, the Moes parameters can be used to re-write the parameters $\bar{\alpha}$ and $\bar{\lambda}$:

$$\begin{aligned} \bar{\lambda} &= (\frac{128\pi^3}{3M^4})^{1/3} \\ \bar{\alpha} &= \frac{L}{\pi}(\frac{3M}{2})^{1/3} \end{aligned} \tag{2.19}$$

Hamrock and Dowson [120] introduced three parameters to simplify the study of film thickness. For point contact they are written as:

$$\begin{aligned} W &= \frac{w}{E' R_x^2} \\ U &= \frac{\eta_0 u_r}{E' R_x} \\ G &= \alpha E' \end{aligned} \tag{2.20}$$

2.3 The finite difference scheme

The second-order self-adjoint elliptic partial differential equation considered by Alcouffe [66] is

$$-\nabla \cdot (D(x,y,t)\nabla U(x,y,t)) + \sigma(x,y,t)U(x,y,t) = f(x,y,t) \qquad (x,y) \in \Omega \tag{2.21}$$

Compared to this equation, the Reynolds equation is of the same type with $U = P$, $\sigma = 0$, $D = -(\bar{\rho}H^3)/(\bar{\eta}\bar{\lambda})$ and $f = \partial(\bar{\rho}H)/\partial X + \partial(\bar{\rho}H)/\partial T$. Rearranging the Reynolds equation (2.11) yields:

$$-\frac{\partial}{\partial X}(D\frac{\partial P}{\partial X}) - \frac{\partial}{\partial Y}(D\frac{\partial P}{\partial Y}) = \frac{\partial(\bar{\rho}H)}{\partial X} + \frac{\partial(\bar{\rho}H)}{\partial T} \qquad (X,Y) \in \Omega \tag{2.22}$$

In the present work, the calculation domain Ω is a rectangle $[X_a, X_b] \times [-Y_a, Y_a]$. This domain is covered with a uniform grids with a system of straight lines parallel to the coordinate axes. The mesh size in the two directions is $hx = (X_b - X_a)/N_x$ and $hy = 2 \times Y_a/N_y$, in which N_x and N_y are the number of mesh points in both directions.

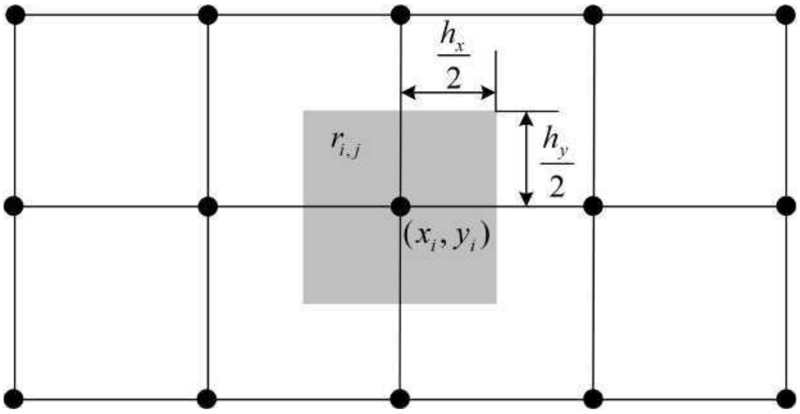

Figure 2.1: Mesh point (x_i, y_j) and it's related mesh region $r_{i,j}$

To derive the difference scheme, a mesh region $r_{i,j}$ (shown as Figure 2.1) defined by the lines $x = x_i - h_x/2$, $x = x_i + h_x/2$, $y = y_j - h_y/2$ and $y = y_j + h_y/2$ for each mesh point (x_i, y_j) is selected. In terms of each mesh point (x_i, y_j), $P(x_i, y_j, t_k) := P_{i,j,k}$ is unknown, now integrating Equation 2.22 over the corresponding mesh region $r_{i,j}$:

$$-\int_{r_{i,j}}\int [\frac{\partial}{\partial X}(D\frac{\partial P}{\partial X}) + \frac{\partial}{\partial Y}(D\frac{\partial P}{\partial Y})]dxdy = \int_{r_{i,j}}\int [\frac{\partial(\bar{\rho}H)}{\partial X} + \frac{\partial(\bar{\rho}H)}{\partial T}]dxdy \tag{2.23}$$

According to Green's Theorem [121], Equation 2.23 can be expressed as:

$$-\int_{c_{i,j}} [(D\frac{\partial P}{\partial X})dy - (D\frac{\partial P}{\partial Y})dx] = \int_{r_{i,j}}\int [\frac{\partial(\bar{\rho}H)}{\partial X} + \frac{\partial(\bar{\rho}H)}{\partial T}]dxdy \tag{2.24}$$

where $c_{i,j}$ is the boundary of $r_{i,j}$ and the integration path along this boundary is anticlockwise. Supposing $f(x_i, y_j, t_k) := f_{i,j,k}$, the double integrals of the right hand side of Equation 2.24 can be simply approximated by means of

$$\int_{r_{i,j}}\int f(x,y,t)dxdy \doteq f_{i,j,k}\cdot a_{i,j}. \tag{2.25}$$

where $a_{i,j} = hx\cdot hy$ is the area of the rectangle region $r_{i,j}$ shown in Figure 2.2.

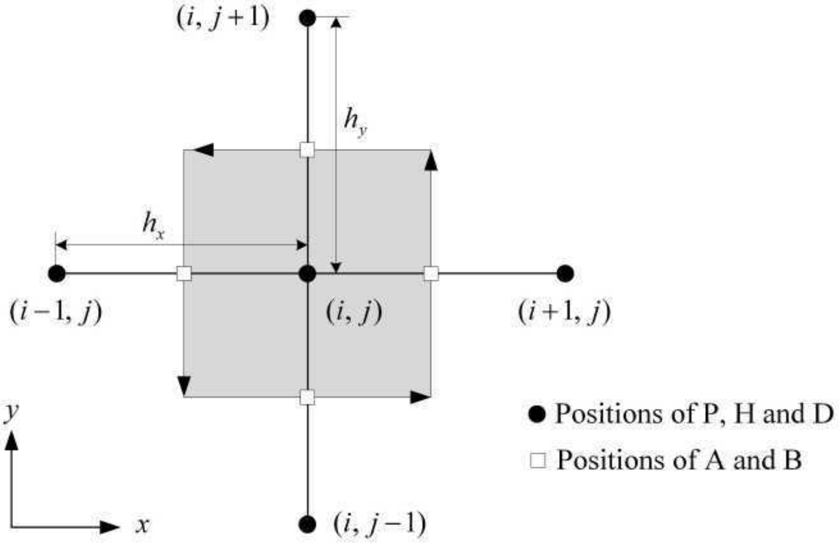

Figure 2.2: Mesh point (i, j).

Referring again to Figure 2.2, the line integal of Equation 2.24 over the four boundaries of $r_{i,j}$ is approximated by means of central differences as:

$$\begin{aligned}-\int_{c_{i,j}} [(D\frac{\partial P}{\partial X})dy - (D\frac{\partial P}{\partial Y})dx] \doteq (hy)[D_{i+1/2,j,k}(\frac{P_{i,j,k} - P_{i+1,j,k}}{hx}) \\ + D_{i-1/2,j,k}(\frac{P_{i,j,k} - P_{i-1,j,k}}{hx})] \\ + (hx)[D_{i,j+1/2,k}(\frac{P_{i,j,k} - P_{i,j+1,k}}{hy}) \\ + D_{i,j-1/2,k}(\frac{P_{i,j,k} - P_{i,j-1,k}}{hy})]\end{aligned} \tag{2.26}$$

Rewriting Equation 2.26 and combining Equation 2.25 gives:

$$\begin{aligned}A_{i,j,k}(P_{i,j+1,k}-P_{i,j,k})+A_{i,j-1,k}(P_{i,j-1,k}-P_{i,j,k})+\\ B_{i,j,k}(P_{i+1,j,k}-P_{i,j,k})+B_{i,j-1,k}(P_{i-1,j,k}-P_{i,j,k})=F_{i,j,k}\end{aligned} \tag{2.27}$$

where

$$A_{i,j,k}=-(\frac{1}{2})(\frac{hx}{hy})(D_{i,j,k}+D_{i,j+1,k})$$

$$B_{i,j,k}=-(\frac{1}{2})(\frac{hy}{hx})(D_{i,j,k}+D_{i+1,j,k})$$

$$F_{i,j,k}=(hx\cdot hy)f_{i,j,k}$$

In terms of $f_{i,j,k}$, the same discrete schemes used in Reference [10] is adopted. At this point, the right hand side of Equation 2.27 can be taken as:

$$\begin{aligned}F_{i,j,k}\doteq hy(1.5\bar{\rho}_{i,j,k}H_{i,j,k}-2\bar{\rho}_{i-1,j,k}H_{i-1,j,k}+0.5\bar{\rho}_{i-2,j,k}H_{i-2,j,k})\\ +\frac{hx\cdot hy}{ht}(1.5\bar{\rho}_{i,j,k}H_{i,j,k}-2\bar{\rho}_{i,j,k-1}H_{i,j,k-1}+0.5\bar{\rho}_{i,j,k-2}H_{i,j,k-2})\end{aligned} \tag{2.28}$$

where ht is the mesh size in time domain. A more detailed derivation of the above difference scheme can be found in Reference [122].

2.4 Transfer operators

Intergrid transfers are used for connecting the fine grid with the coarse grid. After a number of relaxations the error on the fine grid is smooth enough to be approximate on the coarse grid. Hence a restriction operator I_h^H is needed to transfer the approximated solution $\underline{\widetilde{P}}^h$ and the residual $\underline{r}^h$. When the low frequency errors have been eliminated on the coarse grid, it is necessary to define a new error $\underline{v}^h$ ($\underline{v}^h=\underline{P}^h-\underline{\widetilde{P}}^h$) on the fine grid to correct the fine grid approximate solution $\underline{\widetilde{P}}^h$. The classical bi-linear interpolation works quite well for most load cases. However when D jumps by orders of magnitude, Alcouffe [66] proposed a more efficient interpolation operator and this type of operator allows $D\nabla P$ to be continuous over the whole calculation domain and gives a more reasonable physical representation on the coarse grid [123].

2.4.1 Interpolation

Having defined the coefficients A and B in Equation 2.27, it is time to define the interpolation operator. In matrix form, the interpolation can be represented as:

$$\underline{v}^h=I_H^h\underline{v}^H \tag{2.29}$$

where $\underline{v}^h$ and $\underline{v}^H$ are the fine grid and coarse grid error vectors respectively. I_H^h is the interpolation operator and the superscripts h and H stand for the fine grid and the coarse grid respectively. The new coarse grid construction method proposed by Alcouffe et al. [66] is used here, the interpolation process will be illustrated as follows:
The first step is to interpolate the fine grid points (black points shown in Figure 2.3 (b)) coinciding with the coarse grid points (green points shown in Figure 2.3 (a)):

$$v^h_{iF,jF,k}=v^H_{iC,jC,k} \tag{2.30}$$

where v^h is the error on the fine grid, and v^H is the error on the coarse grid. Subscripts (iF, jF, k) and (iC, jC, k) are applied for illustrate the mesh points on the fine grid and on the coarse grid at the k^{th} time step respectively.
The second step is to obtain the middle points, represented as blue dots in Figure 2.3 (c), on the fine grid. Along horizontal lines, the expression for middle points is:

$$v^h_{iF+1,jF,k} = \frac{(B^h_{iF,jF,k} v^H_{iC,jC,k} + B^h_{iF+1,jF,k} v^H_{iC+1,jC,k})}{(B^h_{iF,jF,k} + B^h_{iF+1,jF,k})} \tag{2.31}$$

A similar expression can be derived for vertical lines, which reads:

$$v^h_{iF,jF+1,k} = \frac{(A^h_{iF,jF,k} v^H_{iC,jC,k} + A^h_{iF,jF+1,k} v^H_{iC+1,jC,k})}{(A^h_{iF,jF,k} + A^h_{iF,jF+1,k})} \tag{2.32}$$

Finally, the central point represented as a red point in Figure 2.3 (d) on the fine grid, which is obtained as:

$$\begin{aligned} v^h_{iF+1,jF+1,k} = {} & (A^h_{iF+1,jF+1,k} v^h_{iF+1,jF+2,k} + A^h_{iF+1,jF,k} v^h_{iF+1,jF,k} + \\ & B^h_{iF,jF+1,k} v^h_{iF,jF+1,k} + B^h_{iF+1,jF+1,k} v^h_{iF+1,jF+1,k}) / \\ & (A^h_{iF+1,jF+1,k} + A^h_{iF+1,jF,k} + B^h_{iF,jF+1,k} + B^h_{iF+1,jF+1,k}) \end{aligned} \tag{2.33}$$

The above pointwise description (from Equation 2.30 to Equation 2.33) can be replaced by the matrix expression Equation 2.29, in which the matrix is large and complex. A simply way to describe this matrix is by using a stencil notation. As was shown in Figure 2.4, in the interpolation process, the stencil provides weighting factors for dividing the coarse grid value in point (iC, jC, k) to the coinciding fine grid point (iF, jF, k) as well as its 8 adjacent points. Observing those pointwise expressions, the contribution of the coarse grid point to the 9 corresponding fine grids can be written as a stencil I^h_H in Equation 2.34.

$$I^h_H = \begin{bmatrix} NW^h_{iF,jF,k} & N^h_{iF,jF,k} & NE^h_{iF,jF,k} \\ W^h_{iF,jF,k} & C^h_{iF,jF,k} & E^h_{iF,jF,k} \\ SW^h_{iF,jF,k} & S^h_{iF,jF,k} & SE^h_{iF,jF,k} \end{bmatrix} \tag{2.34}$$

where

$C^h_{iF,jF,k} = 1,$

$$N^h_{iF,jF,k} = \frac{A^h_{iF,jF,k}}{A^h_{iF,jF,k} + A^h_{iF,jF+1,k}}, \qquad E^h_{iF,jF,k} = \frac{B^h_{iF,jF,k}}{B^h_{iF,jF,k} + B^h_{iF+1,jF,k}},$$

$$S^h_{iF,jF,k} = \frac{A^h_{iF,jF-1,k}}{A^h_{iF,jF-2,k} + A^h_{iF,jF-1,k}}, \qquad W^h_{iF,jF,k} = \frac{B^h_{iF-1,jF,k}}{B^h_{iF-1,jF,k} + B^h_{iF-2,jF,k}},$$

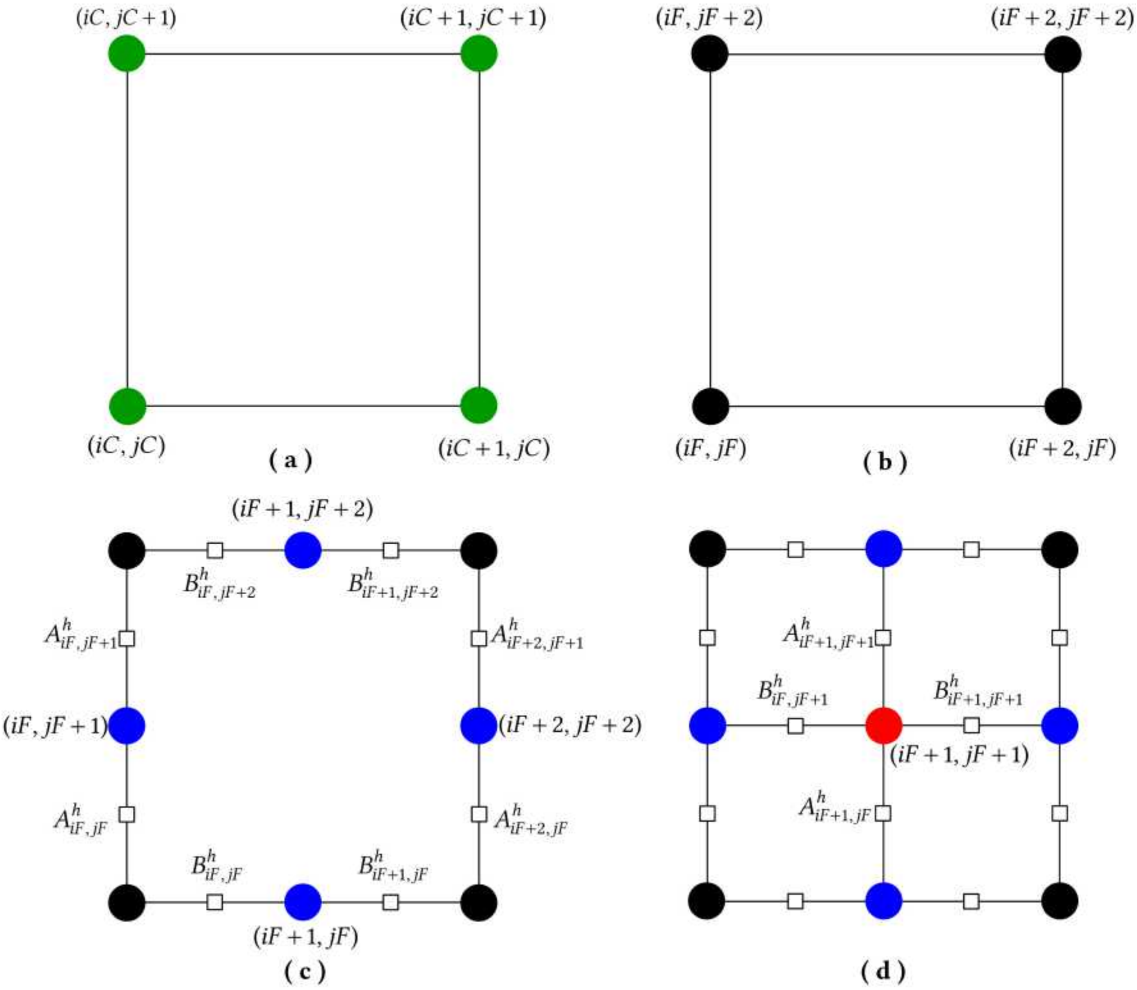

Figure 2.3: Interpolation process (green points: coarse grid points, black dots: fine grid points, blue dots: middle points on the fine grid, red point: central point on the fine grid).

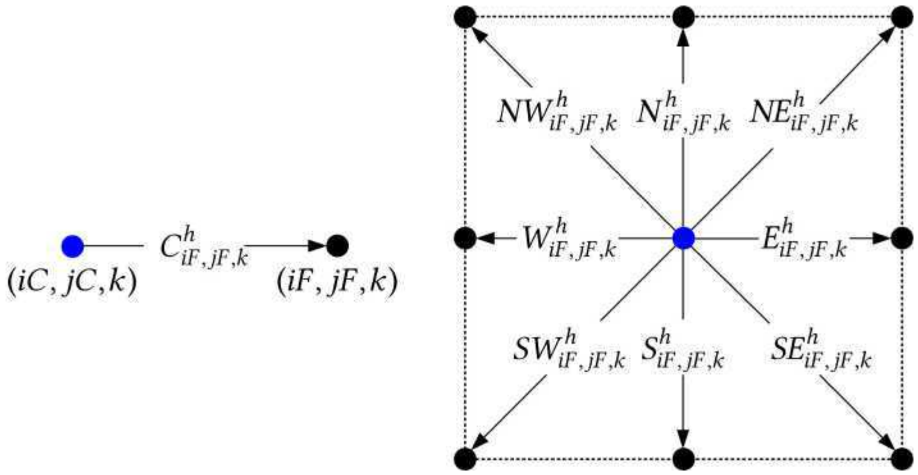

Figure 2.4: Weighting factors for the interpolation (blue points: coarse grid points, black dots: fine grid points).

$$
\begin{aligned}
NE^h_{iF,jF,k} = {} & \frac{[B^h_{iF,jF+1,k}A^h_{iF,jF,k}/(A^h_{iF,jF,k}+A^h_{iF,jF+1,k})]}{A^h_{iF+1,jF+1,k}+A^h_{iF+1,jF,k}+B^h_{iF+1,jF+1,k}+B^h_{iF,jF+1,k}} \\
& + \frac{[B^h_{iF,jF,k}A^h_{iF+1,jF,k}/(B^h_{iF,jF,k}+B^h_{iF+1,jF,k})]}{A^h_{iF+1,jF+1,k}+A^h_{iF+1,jF,k}+B^h_{iF+1,jF+1,k}+B^h_{iF,jF+1,k}},
\end{aligned}
$$

$$
\begin{aligned}
NW^h_{iF,jF,k} = {} & \frac{[B^h_{iF-1,jF+1,k}A^h_{iF,jF,k}/(A^h_{iF,jF,k}+A^h_{iF,jF+1,k})]}{A^h_{iF-1,jF+1,k}+A^h_{iF-1,jF,k}+B^h_{iF-2,jF+1,k}+B^h_{iF-1,jF+1,k}} \\
& + \frac{[B^h_{iF-1,jF,k}A^h_{iF-1,jF,k}/(B^h_{iF-1,jF,k}+B^h_{iF-2,jF,k})]}{A^h_{iF-1,jF+1,k}+A^h_{iF-1,jF,k}+B^h_{iF-2,jF+1,k}+B^h_{iF-1,jF+1,k}},
\end{aligned}
$$

$$
\begin{aligned}
SE^h_{iF,jF,k} = {} & \frac{[B^h_{iF,jF-1,k}A^h_{iF,jF-1,k}/(A^h_{iF,jF-1,k}+A^h_{iF,jF-2,k})]}{A^h_{iF+1,jF-1,k}+A^h_{iF+1,jF-2,k}+B^h_{iF,jF-1,k}+B^h_{iF+1,jF-1,k}} \\
& + \frac{[B^h_{iF,jF,k}A^h_{iF+1,jF-1,k}/(B^h_{iF,jF,k}+B^h_{iF+1,jF,k})]}{A^h_{iF+1,jF-1,k}+A^h_{iF+1,jF-2,k}+B^h_{iF,jF-1,k}+B^h_{iF+1,jF-1,k}},
\end{aligned}
$$

$$
\begin{aligned}
SW^h_{iF,jF,k} = {} & \frac{[B^h_{iF-1,jF-1,k}A^h_{iF,jF-1,k}/(A^h_{iF,jF-1,k}+A^h_{iF,jF-2,k})]}{A^h_{iF-1,jF-1,k}+A^h_{iF-1,jF-2,k}+B^h_{iF-2,jF-1,k}+B^h_{iF-1,jF-1,k}} \\
& + \frac{[B^h_{iF-1,jF,k}A^h_{iF-1,jF-1,k}/(B^h_{iF-1,jF,k}+B^h_{iF-2,jF,k})]}{A^h_{iF-1,jF-1,k}+A^h_{iF-1,jF-2,k}+B^h_{iF-2,jF-1,k}+B^h_{iF-1,jF-1,k}}.
\end{aligned}
$$

2.4.2 Injection

In general, the restriction operator matrix is the transposed matrix of the interpolation operator [10]:

$$I^H_h = (I^h_H)^T \tag{2.35}$$

In order to derive the restriction operator, a basis function $e^l_{i,j}$ whose value is 1 at the point (i, j) on the lth grid is employed.

$$W^H = (I^H_h W^h)_{(iC,jC)} = [(I^h_H)^T W^h]_{(iC,jC)} = \sum_{iF}\sum_{jF} \frac{\langle I^h_H e^H_{iC,jC}, e^h_{iF,jF}\rangle}{\langle e^H_{iC,jC}, e^H_{iC,jC}\rangle} W^h_{iF,jF} \tag{2.36}$$

in which W^H and W^h are vectors of unknowns on the coarse and fine grid respectively. In terms of the orthogonal basis $e^l_{i,j}$, the dot products are $\langle e^H_{iC,jC}, e^H_{iC,jC}\rangle$ = HxHy and $\langle e^h_{iF,jF}, e^h_{iF,jF}\rangle$ = hxhy.

Supposing the vectors of unknowns on coarse grid and on fine grid are marked as $W^H = [u^H_{iC,jC,k}]$ and $W^h = [u^h_{iF-1,jF+1,k}, u^h_{iF-1,jF,k}, u^h_{iF-1,jF-1,k}, u^h_{iF,jF+1,k}, u^h_{iF,jF,k}, u^h_{iF,jF-1,k}, u^h_{iF+1,jF+1,k}, u^h_{iF+1,jF,k}, u^h_{iF+1,jF-1,k}]$. According to Equation 2.36, one can obtain:

$$
\begin{aligned}
u^H_{iC,jC,k} = \frac{hx\cdot hy}{Hx\cdot Hy}(& C^h_{iF,jF,k}u^h_{iF,jF,k} + NW^h_{iF,jF,k}u^h_{iF-1,jF+1,k} + SW^h_{iF,jF,k}u^h_{iF-1,jF-1,k} \\
& + SE^h_{iF,jF,k}u^h_{iF+1,jF-1,k} + NE^h_{iF,jF,k}u^h_{iF+1,jF+1,k} + N^h_{iF,jF,k}u^h_{iF,jF+1,k} \\
& + S^h_{iF,jF,k}u^h_{iF,jF-1,k} + W^h_{iF,jF,k}u^h_{iF-1,jF,k} + E^h_{iF,jF,k}u^h_{iF+1,jF,k}).
\end{aligned}
\tag{2.37}
$$

Hence, the stencil of the restriction operator I_h^H is:

$$I_h^H = \frac{hx \cdot hy}{Hx \cdot Hy} \begin{bmatrix} nw^h_{iF,jF,k} & n^h_{iF,jF,k} & ne^h_{iF,jF,k} \\ w^h_{iF,jF,k} & c^h_{iF,jF,k} & e^h_{iF,jF,k} \\ sw^h_{iF,jF,k} & s^h_{iF,jF,k} & se^h_{iF,jF,k} \end{bmatrix} \tag{2.38}$$

where

$$c^h_{iF,jF,k} = 1,$$

$$n^h_{iF,jF,k} = \frac{A^h_{iF,jF,k}}{A^h_{iF,jF,k} + A^h_{iF,jF+1,k}}, \qquad e^h_{iF,jF,k} = \frac{B^h_{iF,jF,k}}{B^h_{iF,jF,k} + B^h_{iF+1,jF,k}},$$

$$s^h_{iF,jF,k} = \frac{A^h_{iF,jF-1,k}}{A^h_{iF,jF-2,k} + A^h_{iF,jF-1,k}}, \qquad w^h_{iF,jF,k} = \frac{B^h_{iF-1,jF,k}}{B^h_{iF-1,jF,k} + B^h_{iF-2,jF,k}},$$

$$\begin{aligned} ne^h_{iF,jF,k} = {} & \frac{[B^h_{iF,jF+1,k} A^h_{iF,jF,k} / (A^h_{iF,jF,k} + A^h_{iF,jF+1,k})]}{A^h_{iF+1,jF+1,k} + A^h_{iF+1,jF,k} + B^h_{iF+1,jF+1,k} + B^h_{iF,jF+1,k}} \\ & + \frac{[B^h_{iF,jF,k} A^h_{iF+1,jF,k} / (B^h_{iF,jF,k} + B^h_{iF+1,jF,k})]}{A^h_{iF+1,jF+1,k} + A^h_{iF+1,jF,k} + B^h_{iF+1,jF+1,k} + B^h_{iF,jF+1,k}}, \end{aligned}$$

$$\begin{aligned} nw^h_{iF,jF,k} = {} & \frac{[B^h_{iF-1,jF+1,k} A^h_{iF,jF,k} / (A^h_{iF,jF,k} + A^h_{iF,jF+1,k})]}{A^h_{iF-1,jF+1,k} + A^h_{iF-1,jF,k} + B^h_{iF-2,jF+1,k} + B^h_{iF-1,jF+1,k}} \\ & + \frac{[B^h_{iF-1,jF,k} A^h_{iF-1,jF,k} / (B^h_{iF-1,jF,k} + B^h_{iF-2,jF,k})]}{A^h_{iF-1,jF+1,k} + A^h_{iF-1,jF,k} + B^h_{iF-2,jF+1,k} + B^h_{iF-1,jF+1,k}}, \end{aligned}$$

$$\begin{aligned} se^h_{iF,jF,k} = {} & \frac{[B^h_{iF,jF-1,k} A^h_{iF,jF-1,k} / (A^h_{iF,jF-1,k} + A^h_{iF,jF-2,k})]}{A^h_{iF+1,jF-1,k} + A^h_{iF+1,jF-2,k} + B^h_{iF,jF-1,k} + B^h_{iF+1,jF-1,k}} \\ & + \frac{[B^h_{iF,jF,k} A^h_{iF+1,jF-1,k} / (B^h_{iF,jF,k} + B^h_{iF+1,jF,k})]}{A^h_{iF+1,jF-1,k} + A^h_{iF+1,jF-2,k} + B^h_{iF,jF-1,k} + B^h_{iF+1,jF-1,k}}, \end{aligned}$$

$$\begin{aligned} sw^h_{iF,jF,k} = {} & \frac{[B^h_{iF-1,jF-1,k} A^h_{iF,jF-1,k} / (A^h_{iF,jF-1,k} + A^h_{iF,jF-2,k})]}{A^h_{iF-1,jF-1,k} + A^h_{iF-1,jF-2,k} + B^h_{iF-2,jF-1,k} + B^h_{iF-1,jF-1,k}} \\ & + \frac{[B^h_{iF-1,jF,k} A^h_{iF-1,jF-1,k} / (B^h_{iF-1,jF,k} + B^h_{iF-2,jF,k})]}{A^h_{iF-1,jF-1,k} + A^h_{iF-1,jF-2,k} + B^h_{iF-2,jF-1,k} + B^h_{iF-1,jF-1,k}}. \end{aligned}$$

Subsequently, the solution P^H and the residual r^H on the coarse grid are restricted as:

$$\begin{aligned} P^H_{iC,jC,k} &= I^H_h P^h_{iF,jF,k} \\ &= \frac{hx \cdot hy}{Hx \cdot Hy}[c^h_{iF,jF,k}P^h_{iF,jF,k} + n^h_{iF,jF,k}P^h_{iF,jF+1,k} + s^h_{iF,jF,k}P^h_{iF,jF-1,k} \\ &+ w^h_{iF,jF,k}P^h_{iF-1,jF,k} + e^h_{iF,jF,k}P^h_{iF+1,jF,k} + nw^h_{iF,jF,k}P^h_{iF-1,jF+1,k} \\ &+ sw^h_{iF,jF,k}P^h_{iF-1,jF-1,k} + se^h_{iF,jF,k}P^h_{iF+1,jF-1,k} + ne^h_{iF,jF,k}P^h_{iF+1,jF+1,k}]. \end{aligned} \tag{2.39}$$

Special attention is needed when restricting the residual r^h. The factor $(hx \cdot hy)/(Hx \cdot Hy)$ in Equation 2.38 is used to restrict functions mathematically, which is not used to restrict flows physically. For Reynolds equation, the restriction operator I^H_h must be replaced by J^H_h when restricting the right hand side of the discrete Reynolds equation [124] .

$$J^H_h = \frac{Hx \cdot Hy}{hx \cdot hy} I^H_h = \begin{bmatrix} nw^h_{iF,jF,k} & n^h_{iF,jF,k} & ne^h_{iF,jF,k} \\ w^h_{iF,jF,k} & c^h_{iF,jF,k} & e^h_{iF,jF,k} \\ sw^h_{iF,jF,k} & s^h_{iF,jF,k} & se^h_{iF,jF,k} \end{bmatrix} \tag{2.40}$$

yielding:

$$r^H_{iC,jC,k} = J^H_h r^h_{iF,jF,k}. \tag{2.41}$$

2.5 Coarse grid operator

After defining the transfer operators, the coarse grid operator will be described here. The coarse grid operator is formed by a restriction equation:

$$J^H_h(L^h v^h) = J^H_h r^h \tag{2.42}$$

In which $v^h = I^h_H v^H$ and equation 2.42 can be represented as:

$$J^H_h L^h I^h_H (v^H) = J^H_h r^h \tag{2.43}$$

Thus, the coarse grid operator can be defined as:

$$L^H = J^H_h L^h I^h_H \tag{2.44}$$

Assuming the stencil of L^l at point (i,j) on level l and at k^{th} time step is:

$$L^l = \begin{bmatrix} L^l_{nw}(i,j,k) & L^l_n(i,j,k) & L^l_{ne}(i,j,k) \\ L^l_w(i,j,k) & L^l_c(i,j,k) & L^l_e(i,j,k) \\ L^l_{sw}(i,j,k) & L^l_s(i,j,k) & L^l_{se}(i,j,k) \end{bmatrix} \tag{2.45}$$

The construction of the coarse grid operator can be seen in Appendix A.

The coarse grid operator defined here involves 9 points, while as equation 2.27 shows an operator referring to 5 points on the finest grid, reads:

$$L^h(iF,jF,k) = \begin{bmatrix} 0 & A^h_{iF,jF,k} & 0 \\ B^h_{iF-1,jF,k} & -A^h_{iF,jF,k} - A^h_{iF,jF-1,k} - B^h_{iF-1,jF,k} - B^h_{iF,jF,k} & B^h_{iF,jF,k} \\ 0 & A^h_{iF,jF-1,k} & 0 \end{bmatrix} \tag{2.46}$$

2.6 Relaxation

Employing the grid operator L^l defined before, the discrete Reynolds equation for point (i, j, k) of the grid l at the k^{th} time step is shown as follows:

$$\begin{aligned}&L_c^l P_{i,j,k}^l + L_n^l P_{i,j+1,k}^l + L_w^l P_{i-1,j,k}^l + L_s^l P_{i,j-1,k}^l + L_e^l P_{i+1,j,k}^l +\\ &L_{nw}^l P_{i-1,j+1,k}^l + L_{sw}^l P_{i-1,j-1,k}^l + L_{se}^l P_{i+1,j-1,k}^l + L_{ne}^l P_{i+1,j+1,k}^l =\\ &(h^l \cdot h^l)(\bar{\rho} H)_x^l + (h^l \cdot h^l)(\bar{\rho} H)_t^l\end{aligned} \tag{2.47}$$

with $P_{i,j,k}^l = 0$ for points on the boundary and $P_{i,j,k}^l > 0$ for the cavitation condition. In Equation 2.47, h^l stands for the mesh size on the l^{th} grid. In terms of the couette and the transient term, their discrete forms are:

$$(\bar{\rho} H)_x^l = \begin{cases} \frac{\bar{\rho}_{i,j,k}^l H_{i,j,k}^l - \bar{\rho}_{i-1,j,k}^l H_{i-1,j,k}^l}{h^l} & \text{if } i = 1 \\ \frac{1.5\bar{\rho}_{i,j,k}^l H_{i,j,k}^l - 2.0\bar{\rho}_{i-1,j,k}^l H_{i-1,j,k}^l + 0.5\bar{\rho}_{i-2,j,k}^l H_{i-2,j,k}^l}{h^l} & \text{if } i \geqslant 2 \end{cases} \tag{2.48}$$

and

$$(\bar{\rho} H)_t^l = \begin{cases} 0 & \text{if } nt = 0 \\ \frac{\bar{\rho}_{i,j,k}^l H_{i,j,k}^l - \bar{\rho}_{i-1,j,k}^l H_{i-1,j,k}^l}{ht} & \text{if } nt = 1 \\ \frac{1.5\bar{\rho}_{i,j,k}^l H_{i,j,k}^l - 2.0\bar{\rho}_{i-1,j,k}^l H_{i-1,j,k}^l + 0.5\bar{\rho}_{i-2,j,k}^l H_{i-2,j,k}^l}{ht} & \text{if } nt \geqslant 2 \end{cases} \tag{2.49}$$

with

$$H_{i,j,k}^l = H_0(k) + \frac{X_{i,k}^2}{2} + \frac{Y_{j,k}^2}{2} + \sum_{i'} \sum_{j'} K_{i,i',j,j',k}^{ll} P_{i',j',k}^l \tag{2.50}$$

For the discrete Equation 2.47, Reference [10] shows that an iterative approach of combining the Gauss-Seidel line relaxation and the Jacobi distribution line relaxation is pretty stable and efficient. Hence, in this work the same method is applied. Figure 2.5 shows the relaxation process represented in Reference [10], where ξ^l is the *local* coefficient and its definition can been seen as Equation 2.51.

$$\xi_{i,j,k}^l = \frac{\bar{\rho}(P_{i,j,k}^l)(H_{i,j,k}^l)^3}{\bar{\eta}(P_{i,j,k}^l)\bar{\lambda}} \tag{2.51}$$

with $\xi_{i\pm1/2,j,k}^l = (\xi_{i,j,k} + \xi_{i\pm1,j,k})/2$ and $\xi_{i,j\pm1/2,k}^l = (\xi_{i,j,k} + \xi_{i,j\pm1,k})/2$.

Whether the Gauss-Seidel or the Jacobi distribution line relaxation is used, for each grid point (i, j, k) a new approximation $\bar{P}_{i,j,k}^l$ to $P_{i,j,k}^l$ is computed by:

$$\bar{P}_{i,j,k}^l = \tilde{P}_{i,j,k}^l + \omega\delta_{i,j,k}^l \tag{2.52}$$

with

$$\omega\delta_{i,j,k}^l = \begin{cases} \omega_{gs}\delta_{i,j,k}^l & \text{Guass-Seidel} \\ \omega_{ja}[\delta_{i,j,k}^l - \frac{(\delta_{i+1,j,k}^l + \delta_{i-1,j,k}^l + \delta_{i,j+1,k}^l + \delta_{i,j-1,k}^l)}{4}] & \text{Jacobi distribution} \end{cases}$$

where ω_{gs} and ω_{ja} are the relaxation factors for the Guass-Seidel line relaxation and the Jacobi distribution line relaxation respectively. The changes $\delta_{i,j,k}^l$ for the line relaxation in the X direction can be obtained from:

$$A^j \underline{\delta}_j^l = \underline{r}_j^l \tag{2.53}$$

in which $\underline{\delta}_j^l$ is a vector of changes $\delta_{i,j,k}^l$ and $\underline{r}_j^l$ is the residual vector $r_{i,j,k}^l$, both are n_x element vectors. A^j is a matrix of coefficients $A_{i,m}^j$, whose derivation can be found in Appendix B.

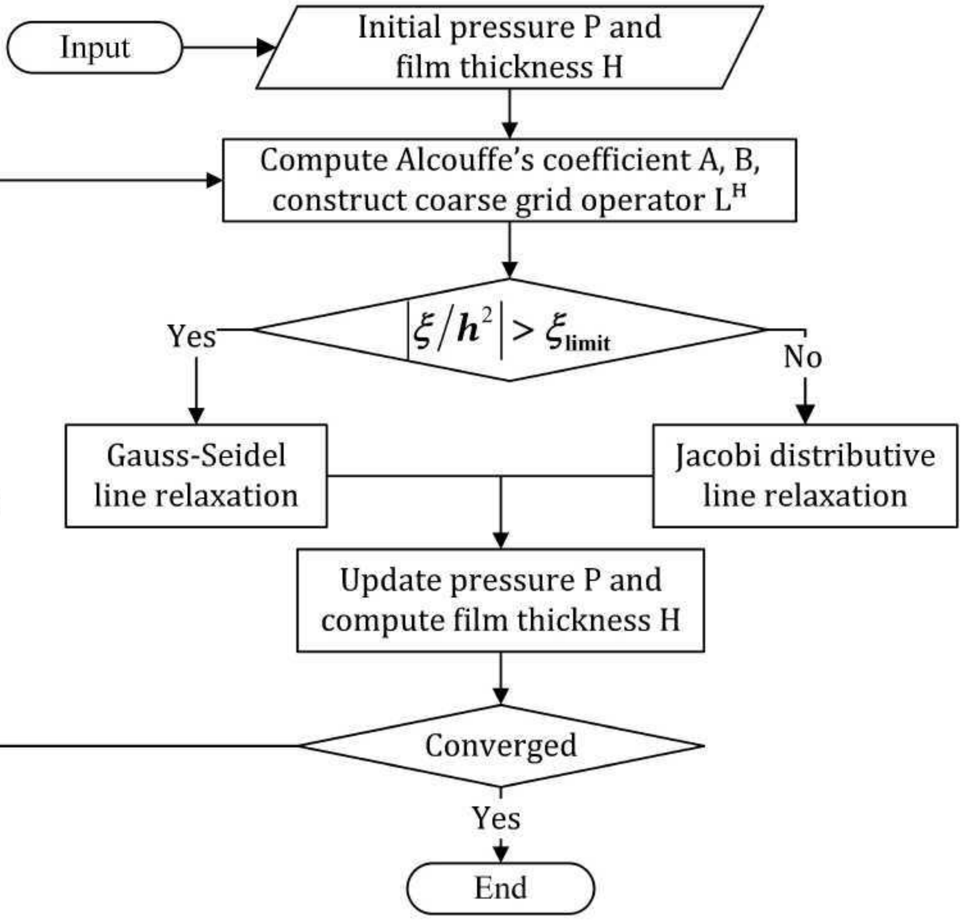

Figure 2.5: Flow chart of the hybrid relaxation process

2.7 Implementation of the Multi-Grid method

So far, pre-preparations for implementing the Multi-Grid method to solve the transient EHL equation system have already been prepared. Final step is to organize all steps together. Figure 2.6 shows a simple two-level "V" cycle which is used to illustrate the implementation of the Multi-Grid method. The corresponding steps are as follows:

- Several relaxations on grid h to obtain an approximate solution $\underline{\tilde{P}}^h$ by:

$$L^h\langle\underline{\tilde{P}}^h\rangle = \underline{F}^h, \tag{2.54}$$

  compute residual on grid h below:

$$\underline{r}^h = \underline{F}^h - L^h\langle\underline{\tilde{P}}^h\rangle. \tag{2.55}$$

- Compute Alcouffe's coefficients A, B and D, prepare the transfer operators I_h^H and I_H^h, construct the coarse grid operator L^H.

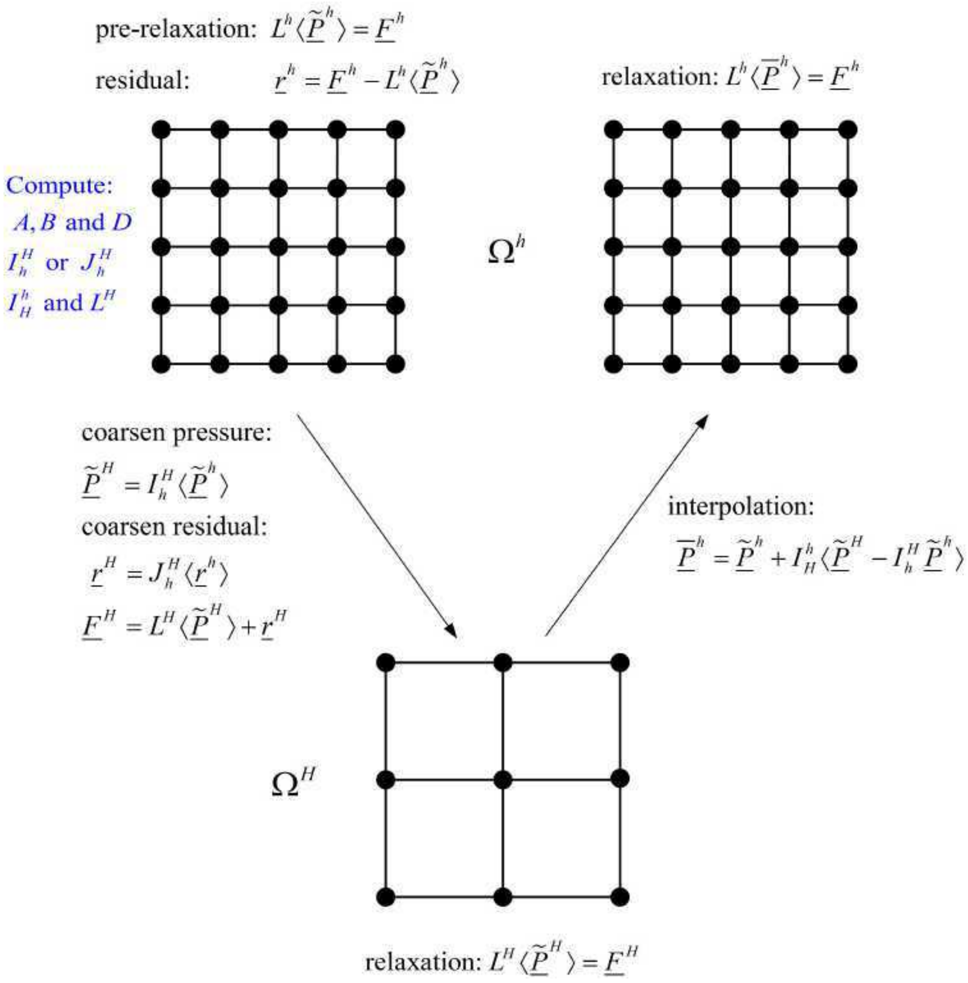

Figure 2.6: Implementation of the Multi-Grid method with a two level "V" cycle.

- Coarsen pressure $\underline{\tilde{P}}^h$ and residual $\underline{r}^h$ to grid H:

$$\begin{aligned} \underline{\tilde{P}}^H &= I_h^H\langle \underline{\tilde{P}}^h\rangle \\ \underline{r}^H &= J_h^H\langle \underline{r}^h\rangle \end{aligned} \tag{2.56}$$

  with the right hand side term $\underline{F}^H$ expressed as:

$$\underline{F}^H = L^H\langle \underline{\tilde{P}}^h\rangle + \underline{r}^H. \tag{2.57}$$

- Relax coarse grid solution $\underline{\tilde{P}}^H$ on grid H through:

$$L^H\langle \underline{\tilde{P}}^H\rangle = \underline{F}^H. \tag{2.58}$$

  if grid H is the coarsest grid, the mutual approach H_0 should be updated.

- Interpolate and correct $\underline{\tilde{P}}^h$ from grid H to h using:

$$\underline{\bar{P}}^h = \underline{\tilde{P}}^h + I_H^h\langle \underline{\tilde{P}}^H - I_h^H \underline{\tilde{P}}^h\rangle. \tag{2.59}$$

- Relaxations on grid h.

For simplicity, the current code uses "V" cycles to solve the EHL equation system. In terms of the transient EHL model, the transient term $\partial\bar{\rho}H/\partial X$ should be arranged in calculation cycles. Here use the equation below to denote the transient Reynolds equation with the first order backward discretization of transient term:

$$L^l\langle P^l\rangle - (h^l \cdot h^l)(\bar{\rho}H)^l_x = (h^l \cdot h^l)(\frac{\bar{\rho}^l_{i,j,k}H^l_{i,j,k} - \bar{\rho}^l_{i-1,j,k}H^l_{i-1,j,k}}{ht}). \tag{2.60}$$

In order to construct the transient "V" cycle, Equation 2.60 will be rewritten as:

$$L^l\langle P^l\rangle - (h^l \cdot h^l)(\bar{\rho}H)^l_x - (h^l \cdot h^l)(\frac{\bar{\rho}^l_{i,j,k}H^l_{i,j,k}}{ht}) = (h^l \cdot h^l)\frac{(-\bar{\rho}^l_{i-1,j,k}H^l_{i-1,j,k})}{ht}. \tag{2.61}$$

Observing Equation 2.61, one finds that the right hand side term of the Reynolds equation is $(h^l \cdot h^l)\frac{(-\bar{\rho}^l_{i-1,j,k}H^l_{i-1,j,k})}{ht}$. As shown in Figure 2.7, the right hand side term of the Reynolds equation for the $(nt)^{th}$ time step is the value of $(h^l \cdot h^l)\frac{(-\bar{\rho}^l_{i-1,j,k}H^l_{i-1,j,k})}{ht}$ for the $(nt-1)^{th}$ time step.

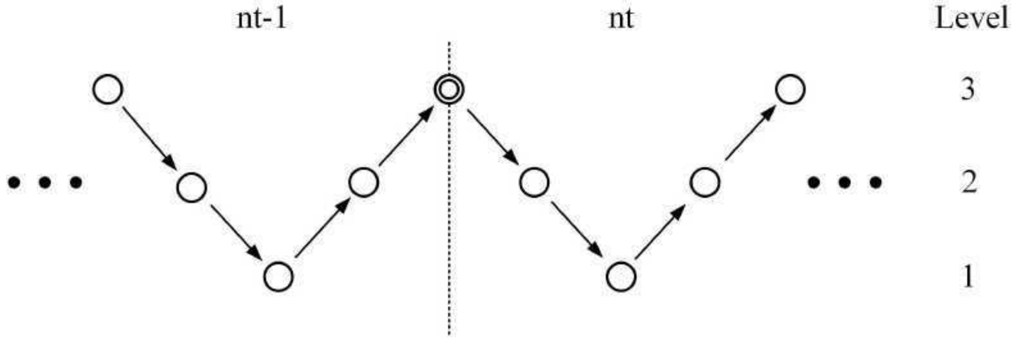

Figure 2.7: The time-dependent "V" cycles

2.8 Conclusion

In this chapter, the coarse grid construction method proposed by Alcouffe et al. [66] is implemented in the current EHL Multi-Grid code. Instead of the bi-linear interpolation stencil used in the class code [10], the new interpolation stencil applying Alcouffe's method is derived. Then the new restriction stencil is obtained through the Equation 2.35. A nine point coarse grid operator is also constructed by the Galerkin method in Appendix A. Finally, the implementation of the Multi-Grid method is introduced briefly.

Chapter 3

Friction influence of harmonic surface waviness

Contents

3.1 Introduction

As mentioned in Chapter 1, the friction of interfacial surfaces greatly influences the performance of mechanical elements. Studies show that the surface roughness amplitude, wavelength and anisotropy affect friction. Thus this chapter investigates the effect of surface waviness on the friction evolution, in which the surface waviness is defined by Equation (3.1). In this chapter, a relative friction coefficient is proposed to indicate the transition from the full-film to the mixed lubrication regime. The definition of the relative friction coefficient is illustrated in Section 3.3. Subsequently, the influence of operating conditions and surface waviness topography on friction are studied. Finally, a single friction curve is obtained depending on a new "Lambda ratio" parameter including operating conditions as well as surface waviness parameters. The waviness is defined as:

$$RR(X,Y,T) = Ai \times 10^{-10[max(0,\frac{X-\bar{X}}{\lambda_x/a_h})^2]} \cos(2\pi\frac{(X-\bar{X})}{\lambda_x/a_h})\cos(2\pi\frac{Y}{\lambda_y/a_h}) \tag{3.1}$$

where $\bar{X} = X_{st} + U_{\text{rat}} \times T$ with $U_{\text{rat}} = u_1/u_r$, Ai is the initial amplitude of the surface waviness, λ_x and λ_y are the wavelengths in x and y direction respectively. At the same time, the parameter r ($r = \lambda_x/\lambda_y$) is used to determine the surface waviness anisotropy. For convenience, the parameter λ is defined as $\lambda = \min(\lambda_x, \lambda_y)$. The exponential term is used to avoid discontinuous derivatives when the waviness moves into the calculation domain.

3.2 Lubricant rheological models

The lubricant rheology greatly determines the friction in a tribological contact [125]. Once the rheology of the lubricant is given, the friction force can be obtained by integration of the shear stress over the contact area [126]. Figure 3.1 shows a typical shear stress-shear rate relationship for an EHL contact. In the low shear strain rate range, the lubricant is Newtonian and the shear stress increases linearly with the shear strain rate. This linear model is valid for predicting hydrodynamic friction [127]. However, in the EHL regime of lubrication, the Newtonian assumption is insufficient, especially when large slide-to-roll ratios are employed. Studies [128–130] show that the lubricant in the inlet zone shows shear-thinning behavior (i.e. the fluid viscosity decreases with increasing shear stress rate) which influences the film thickness. Some frequently-used non-Newtonian fluid models are listed as follows:

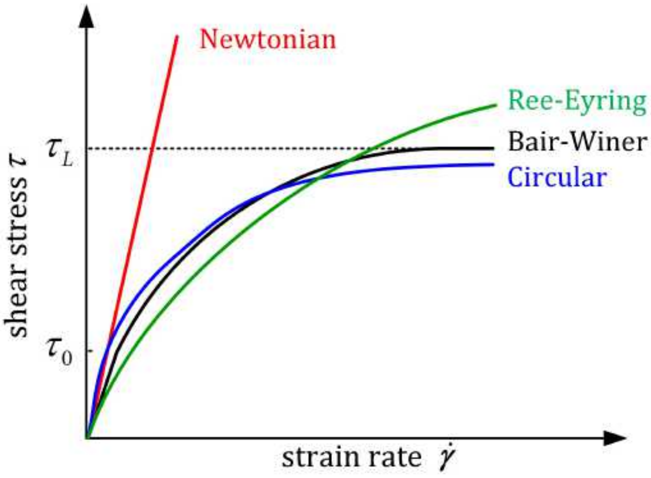

Figure 3.1: Shear stress-shear rate relationship for the EHL contact.

- **Ree-Eyring model (sinh-law model)**

  In 1977, Johnson and Tevaarwerk [131] proposed a simple constitutive equation for an isothermal lubricant based on a "nonlinear Maxwell" model, which reads:

  $$\dot{\gamma} = \frac{1}{G_e}\frac{d\tau}{dt} + \frac{\tau_0}{\eta}\sinh(\frac{\tau}{\tau_0}) \tag{3.2}$$

  in which G_e is the elastic shear modulus, τ is the stress, τ_0 is referred to as the Eyring stress and $\dot{\gamma}$ is the shear strain rate. The strain rate shown as Equation 3.2 consists of two components where the first elastic term is always neglected [132]. Thus Equation 3.2 reduces to:

  $$\dot{\gamma} = \frac{\tau_0}{\eta}\sinh(\frac{\tau}{\tau_0}). \tag{3.3}$$

  Observing Equation 3.3, when the Eyring stress τ_0 approaches infinity, the limit of Equation 3.3 becomes the Newtonian constitutive equation, i.e.:

  $$\lim_{\tau_0\to\infty}\frac{\tau_0}{\eta}\sinh(\frac{\tau}{\tau_0}) = \frac{\tau}{\eta}. \tag{3.4}$$

- **Bair-Winer model**

  For larger strain rates the lubricant exhibits a limiting shear stress τ_L which is the threshold of the shear stress. Bair and Winer [133] modified the "Maxwell" model applying this limiting shear stress, yields:

  $$\dot{\gamma} = \frac{1}{G_\infty}\frac{d\tau}{dt} + \frac{\tau_L}{\eta}\ln(1-\frac{\tau}{\tau_L}) \tag{3.5}$$

where G_∞ is the limiting elastic shear modulus.

- **Carreau-Yasuda model (power-law model)**

  Carreau and Yasuda [134] offered a more general model whose equation is:

  $$\eta = \eta_0[1+(\lambda_t\dot{\gamma})^2]^{(n-1)/2} \tag{3.6}$$

  where λ_t is the time constant for the fluid and $n-1$ is the power-law slope.

- **Circular fluid model**

  In order to overcome the difficulty lies in incorporating the Bair-Winer model into the Reynolds equation, Lee and Hamrock [135] suggested an appropriate lubricant rheological circular model, it reads:

  $$\dot{\gamma} = \frac{\tau}{\eta}[1-(\frac{\tau}{\tau_L})^2]^{-1/2} \tag{3.7}$$

- **Actual Ree-Eyring model**

  Bair [136] proposed an actual Ree-Eyring model for shear-shinning lubricants [137]:

  $$\tau = \sum_{i=1}^{N} x_i\tau_i \sinh^{-1}(\lambda_i\dot{\gamma}) \tag{3.8}$$

  in which $\lambda_i = \eta/\tau_i$ is a characteristic time of the fluid and x_i is a weighting factor ($\sum_{i=1}^{N} = 1$).

3.3 Methodology

3.3.1 Relative friction coefficient

Even though the previous section described several non-Newtonian rheological model, in this section, we will use a Newtonian model to describe friction variations resulting from pressure variations. Two arguments can be used.

- When the shear stress variations are small, a linearised model can be used. See the following example sinh.
- A linear model allows an FFT based sum over all wavelengths which a non-linear model does not.

Example:

$$\begin{aligned}\dot{\gamma} &= \frac{\tau_0}{\eta}\sinh\frac{\tau}{\tau_0}\\ &= \frac{\tau_0}{2\eta}(e^{\tau/\tau_0} - e^{-\tau/\tau_0})\\ &= \frac{\tau_0}{2\eta}(1+\frac{\tau}{\tau_0}+\frac{\tau^2}{2\tau_0^2}+\ldots-1+\frac{\tau}{\tau_0}-\frac{\tau^2}{2\tau_0^2}+\ldots)\\ &\approx \frac{\tau}{\eta}\end{aligned}$$

For Newtonian lubricant, the above equation can be rewritten as:

$$\tau = \eta \frac{du}{dz} \tag{3.9}$$

where u is the velocity in rolling direction, which is defined as [138, 139]:

$$u = \frac{1}{2\eta}\frac{\partial p}{\partial x}(z^2 - zh) + \frac{z}{h}(u_2 - u_1) + u_1. \tag{3.10}$$

Substituting Equation 3.10 into Equation 3.9, yields:

$$\tau = \frac{1}{2}\frac{\partial p}{\partial x}(2z - h) + \eta\frac{u_2 - u_1}{h} \tag{3.11}$$

where two parts contribute to the shear stress, the first term is a parabolic part due to the *Poiseuille flow* and the second term is a linear part due to the *Couette flow*. Thus the viscous shear force on the lower surface ($z = 0$) is obtained by integrating Equation 3.11 [140]:

$$f = -\iint (\frac{\partial p}{\partial x} \cdot \frac{h}{2}) dxdy + \iint (\eta \cdot \frac{u_2 - u_1}{h}) dxdy. \tag{3.12}$$

In the full-film EHL regime, the friction force is dominated by the viscous shear force, the dimensionless friction force is:

$$F_{\text{friction}} = -\iint (\frac{\partial P(X,Y,T)}{\partial X} \cdot \frac{H(X,Y,T)}{2}) dXdY + \iint (\bar{\eta} \cdot \frac{SRR}{H(X,Y,T)}) dXdY \tag{3.13}$$

in which $SRR = (u_2 - u_1)/\bar{u}$ is the slide-to-roll ratio.

Experimental results [141] also found that the Poiseuille force is lower than the Couette force. Hence the dimensionless friction force is simplified as:

$$F(X,Y,T) = \iint \bar{\eta}[P(X,Y,T)] \cdot \frac{SRR}{H(X,Y,T)} dXdY. \tag{3.14}$$

Different lubricant oils give different curves of friction coefficient. For the sake of simplicity, a relative friction coefficient is proposed to detect friction variations, which is defined as:

$$\frac{\mu_r}{\mu_s}(T) = \frac{F_r}{w}(T) / \frac{F_s}{w} = \frac{F_r}{F_s}(T) \tag{3.15}$$

where subscripts r and s are used to distinguish the rough and smooth case.

3.3.2 Numerical solution

The numerical simulation uses the domain $-2.5 \leqslant X \leqslant 1.5$ and $-2.0 \leqslant Y \leqslant 2.0$ with 513×513 equal-spaced points. The time step is selected equal to the spatial mesh size on the finest grid, i.e. with $\Delta T = hx = hy = 0.0078125$. Meanwhile, the calculation starts with $X_{st} = -2.5$ and the surface topography moves into the high pressure zone with the velocity of the rough surface u_1. The monitoring time should be long enough so that 'steady oscillations' of the results occur. The present work considers small-amplitude roughness and a small slip parameter is selected i.e. $U_{rat} = 1.01 (SRR = 0.02)$. This small slip assumption and and small amplitude allow us to use the Amplitude Reduction Theory [53] for pure rolling, as shown in [61].

The numerical code used in the present work is validated by comparing the current results with results from Reference [53]. Figure 3.2 shows the relative deformed amplitude (Ad/Ai) as a function of $f(r)\nabla_2$. This figure shows that results from the current model with $SRR = 0$ (blue squares) fall onto the master curve on Reference [53].

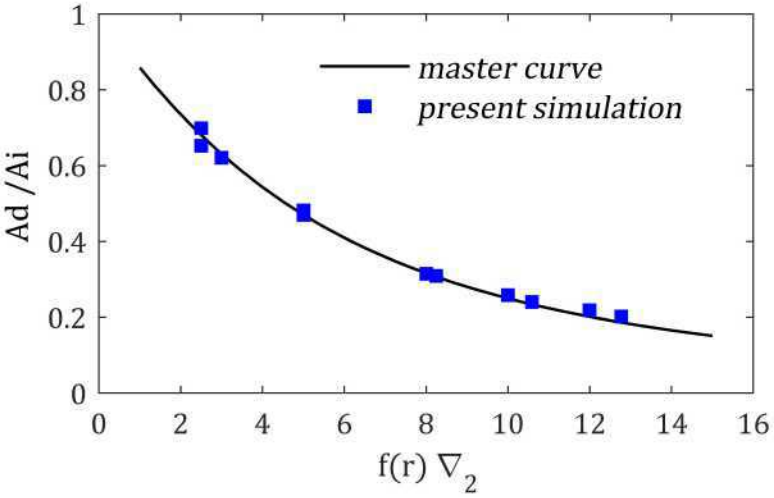

Figure 3.2: Comparison of the relative deformed amplitude (Ad/Ai) as a function of $f(r)\nabla_2$ for the current model (blue squares) with those on Reference [53] (solid line)

The choice of the mesh size influences computing time as well as precision. A large mesh size leads to large discretization errors and a small mesh size causes long computation times. This work applies an intermediate mesh size (513 × 513 points). Table 3.1 suggests that it yields a friction precision better than 1%.

Table 3.1: Relative friction coefficient versus the number of mesh points for: M=1000, L=10, $\lambda_x/a_h = 0.5$, r=0.4 and $Hc/Ai = 2$.

Mesh points	Relative friction coefficient
129 × 129	1.489
257 × 257	1.457
513 × 513	1.462
1025 × 1025	1.465

3.4 Time-dependent solution

Defined by Equation 3.1, Figure 3.3 shows the top view of the surface waviness for three cases: the isotropic surface waviness of $r = 1$ and $\lambda/a_h = 0.5$ (a), the longitudinal surface waviness of $r = 2$ and $\lambda/a_h = 0.5$ (b) and the transverse surface waviness of $r = 0.5$ and $\lambda/a_h = 0.5$ (c).

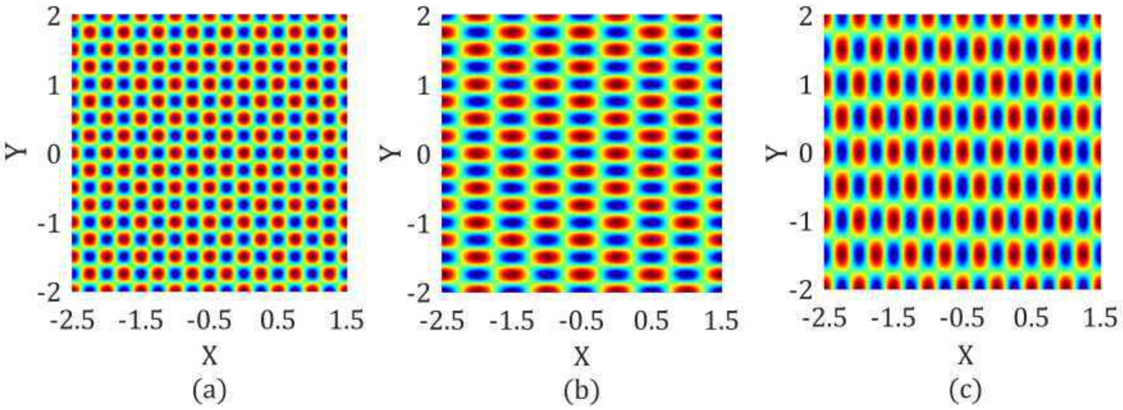

Figure 3.3: Top view of the surface waviness with $\lambda/a_h = 0.5$ and $Ai = 0.5Hc$: (a) the isotropic surface waviness $r = 1$, (b) the longitudinal surface waviness $r = 2$, (c) the transverse surface waviness $r = 0.5$.

For the transient case, in the high pressure zone the *Poiseuille* term vanishes, the Reynolds equation reduces to a transport equation:

$$-\frac{\partial(\bar{\rho}H)}{\partial X}-\frac{\partial(\bar{\rho}H)}{\partial T}\approx 0. \tag{3.16}$$

In this case, the final film thickness and pressure profiles depend on the profiles of steady state case as well as on the inlet disturbances [46]. Figures 3.4-3.6 show dimensionless pressure distribution $P(X,0)$ and dimensionless film thickness distribution $H(X,0)$ for three surface waviness cases, in which Hc is the central film thickness for the smooth case. For the operating condition of $M = 1000$ and $L = 10$, the dimensionless central film thickness for the smooth case is: $Hc = 0.0243$. In this work, we only focus on small surface waviness amplitude values i.e. $Ai/Hc \in [1,10]$. Figures 3.4-3.6 show that the propagation speed of the pressure increase is the same as that of the film thickness variation. This is due to the small slide-to-roll ratio, the velocity of the rough surface is nearly the same as the entrainment velocity $\bar{u}$. In addition, the wavelength of the pressure increase and the film thickness variation are the same as the wavelength of corresponding initial surface waviness.

Figure 3.7 shows the dimensionless central film thickness $Hc_{\text{rough}}(0,0,T)$ as a function of time T for the above three rough cases. The initial amplitude of the surface waviness is $Ai = 0.01215$, while from those figures, one can observe that the amplitude of the central film thickness is smaller. This means that the surface roughness is deformed under current operating conditions. For those cases in Figure 3.7, the deformed amplitudes are: $Ad = 0.0057$ for $r = 1$, $Ad = 0.00375$ for $r = 2$ and $Ad = 0.0057$ for $r = 0.5$. Reference [53] studied this deformation over a large range of operating conditions, and a single equation is obtained as Equation 3.17.

$$\frac{Ad}{Ai}=\frac{1}{1+0.15f(r)\nabla_2+0.015(f(r)\nabla_2)^2} \tag{3.17}$$

where

$$f(r)=\begin{cases} e^{1-1/r}, & \text{if } r>1\\ 1, & \text{otherwise}\end{cases}$$

$r = \lambda_x/\lambda_y$ and $\nabla_2 = (\lambda/a_h)\sqrt{M/L}$ with $\lambda = \min(\lambda_x, \lambda_y)$.

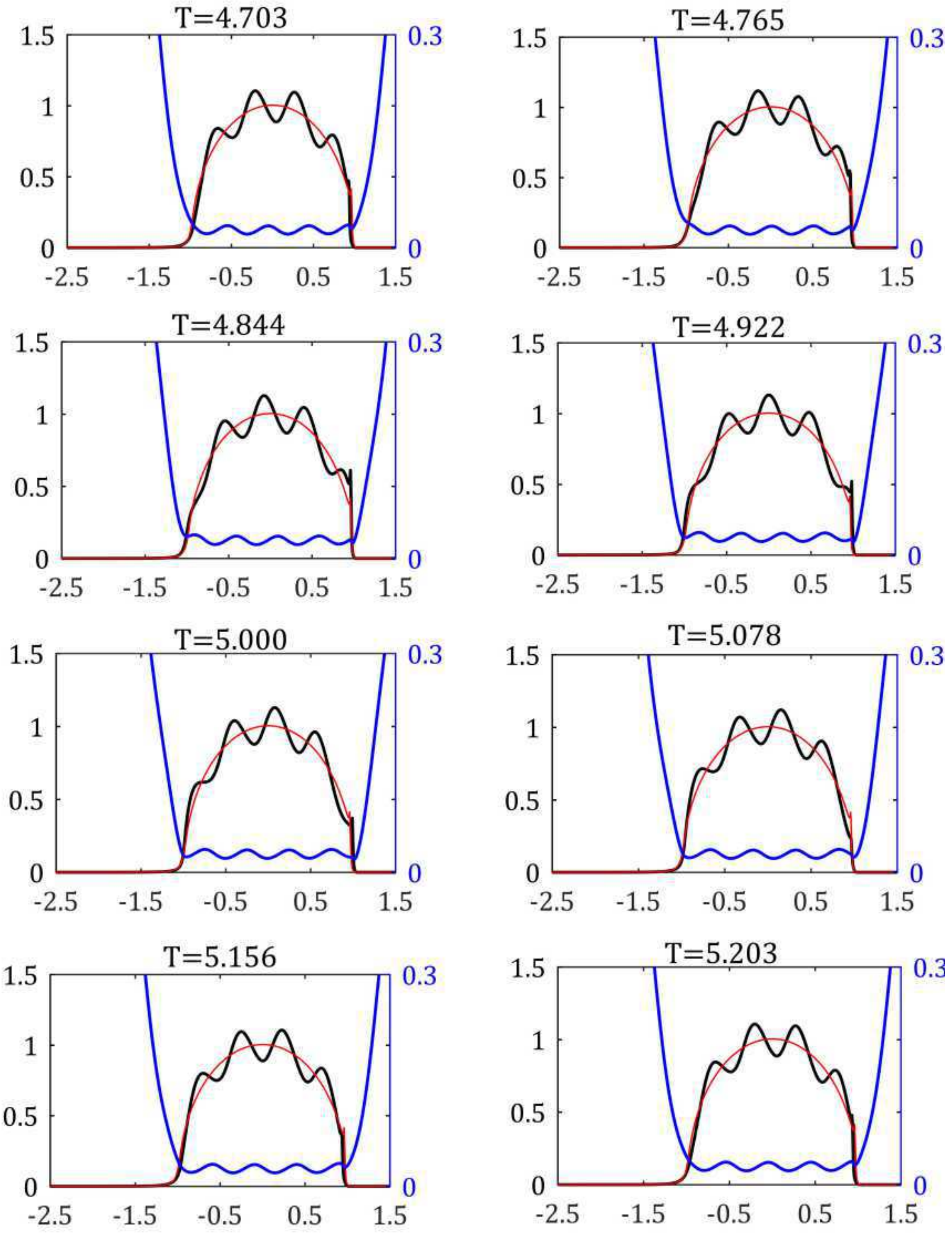

Figure 3.4: Central line pressure $P(X,0)$ (black lines) and central line film thickness $H(X,0)$ (blue lines) of isotropic surface waviness ($r = 1$) for $M = 1000$, $L = 10$, $\lambda / a_h = 0.5$ and $Ai = 0.5Hc$ during a time period. The central pressure line (red line) for the smooth case is plotted as a reference.

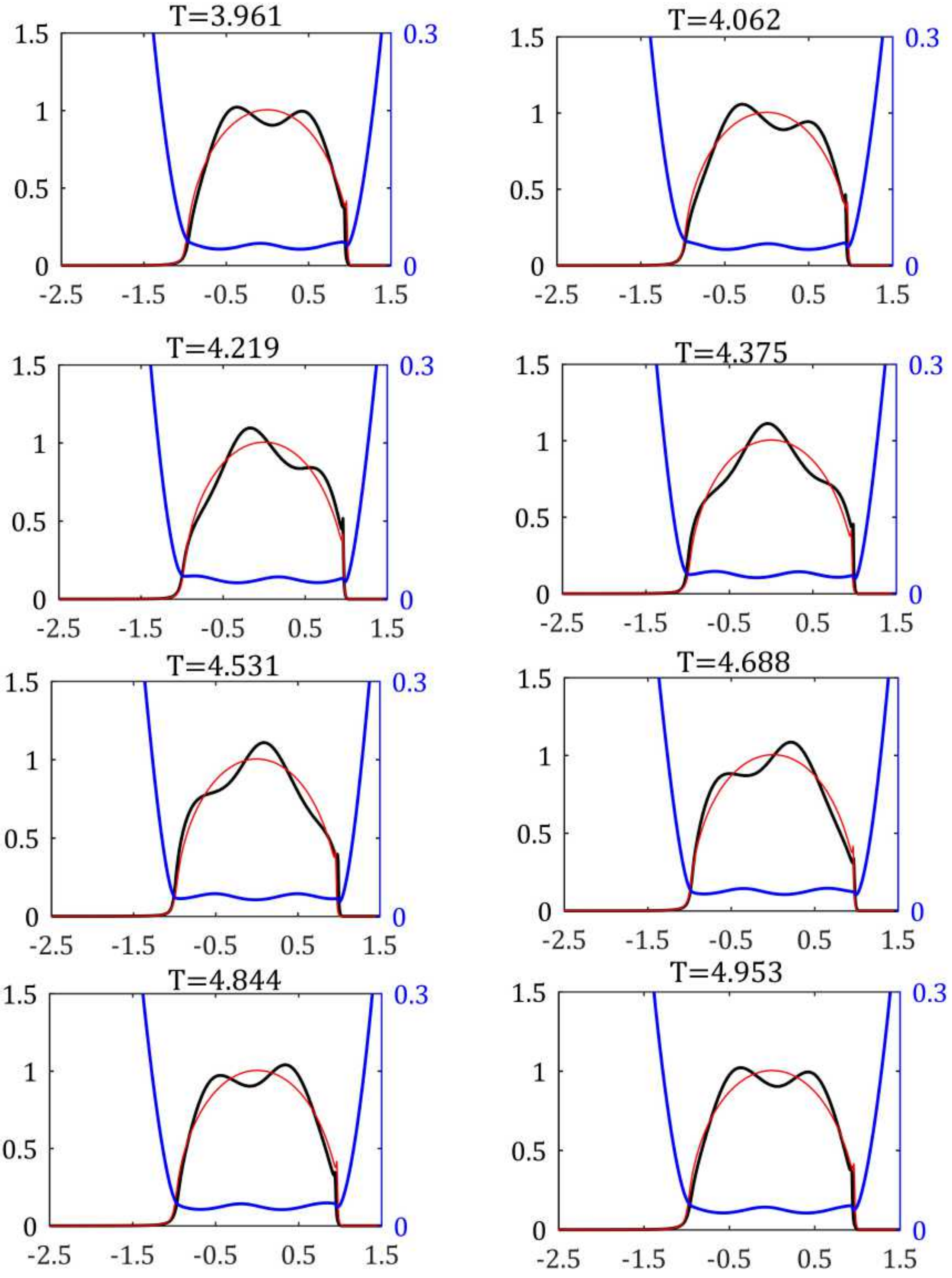

Figure 3.5: Central line pressure $P(X,0)$ (black lines) and central line film thickness $H(X,0)$ (blue lines) of longitudinal surface waviness ($r = 2$) for $M = 1000$, $L = 10$, $\lambda/a_h = 0.5$ and $Ai = 0.5Hc$ during a time period. The central pressure line (red line) for the smooth case is plotted as a reference.

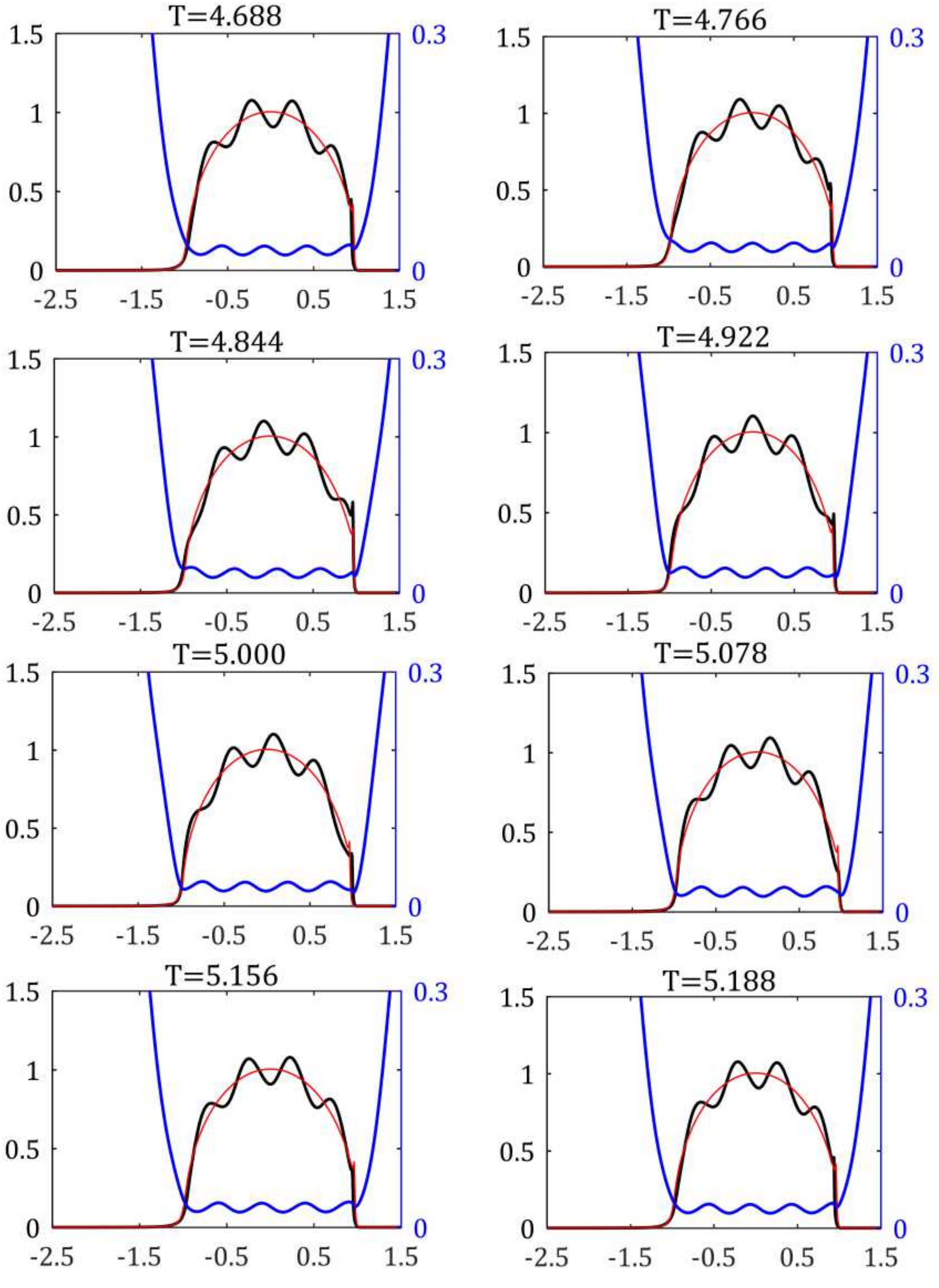

Figure 3.6: Central line pressure $P(X,0)$ (black lines) and central line film thickness $H(X,0)$ (blue lines) of transverse surface waviness ($r = 0.5$) for $M = 1000$, $L = 10$, $\lambda/a_h = 0.5$ and $Ai = 0.5Hc$ during a time period. The central pressure line (red line) for the smooth case is plotted as a reference.

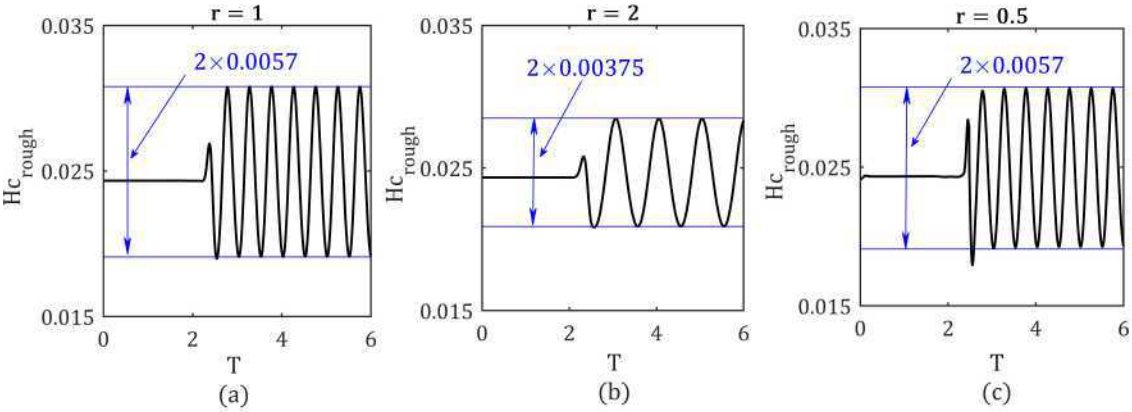

Figure 3.7: The dimensionless central film thickness Hc_{rough} as a function of the dimensionless time T for: $M = 1000$, $L = 10$, $\lambda/a_h = 0.5$ and $Ai = 0.5Hc$: (a) the isotropic surface wavy case, (b) the longitudinal surface wavy case $r = 2$, (c) the transverse surface wavy case $r = 0.5$.

Equation 3.15 shows that the relative friction coefficient is time-dependent. Figure 3.8 depicts the relative friction coefficient as a function of dimensionless time (T) for the isotropic, longitudinal and transverse cases with the same operating condition: M=1000, L=10, $Ai = 0.5Hc$ and dimensionless waviness: $\lambda = 0.5$. Because the surface topography $RR(T)$ is periodical, the relative friction coefficient $(\mu_r/\mu_s)(T)$ is also periodical. For each operating condition, the relative friction coefficient is defined as its average value (shown as blue dotted lines in Figure 3.8) i.e. $\sum_{i=0}^{i=N_T}(\frac{\mu_r}{\mu_s})_i/N_T$ in which N_T is the number of the relative friction coefficient values during one time period. Although the operating conditions for the three surfaces are the same, their averaged friction values are very different i.e. $\mu_r/\mu_s = 1.79$ for $r = 1$, $\mu_r/\mu_s = 1.57$ for $r = 2$ and $\mu_r/\mu_s = 1.48$ for $r = 0.5$.

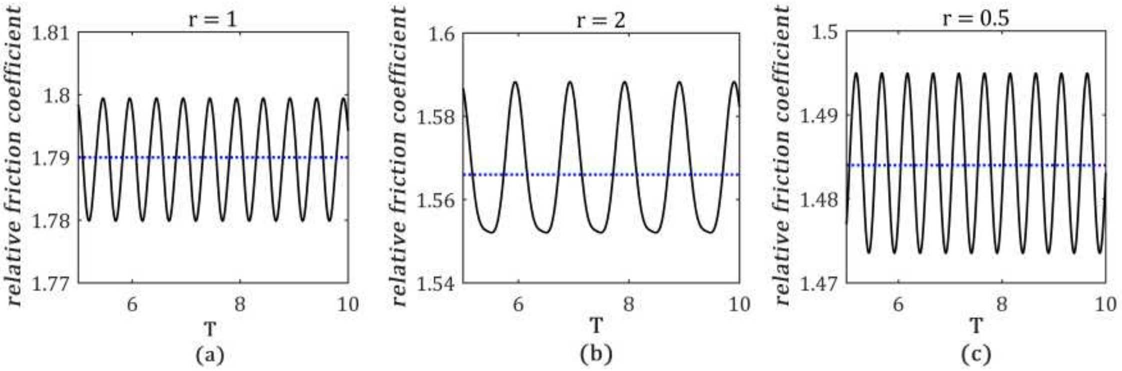

Figure 3.8: The relative friction coefficient μ_r/μ_s as a function of the dimensionless time T for: $M = 1000$, $L = 10$, $\lambda/a_h = 0.5$ and $Ai = 0.5Hc$: (a) isotropic surface wavy case, (b) longitudinal surface wavy case $r = 2$, (c) transverse surface wavy case $r = 0.5$. (Blue dotted line: average value of the relative friction coefficient.)

3.5 Effect of operating conditions

The relative friction coefficient can be plotted as a function of the classical parameter "lambda ratio" i.e. Hc/Ai (Ai is varying and Hc is fixed) for a specific operating condition: Figure 3.9. This figure shows that as Hc/Ai increases, the relative coefficient decreases monotonically.

Early work on conformal condition shows that with the "Λ ratio" increasing, the friction coefficient decreases to a minimum value (the transition position from the full-film to the mixed lubrication regime) first then increases.

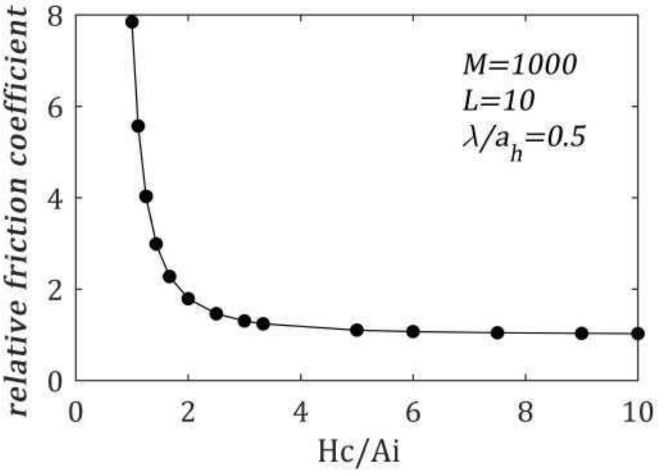

Figure 3.9: Relative friction coefficient as a function of Hc/Ai for a specific operating condition

The following work will detect the influence of the operating conditions M, L and surface wavelength on the relative friction coefficient for the isotropic case.

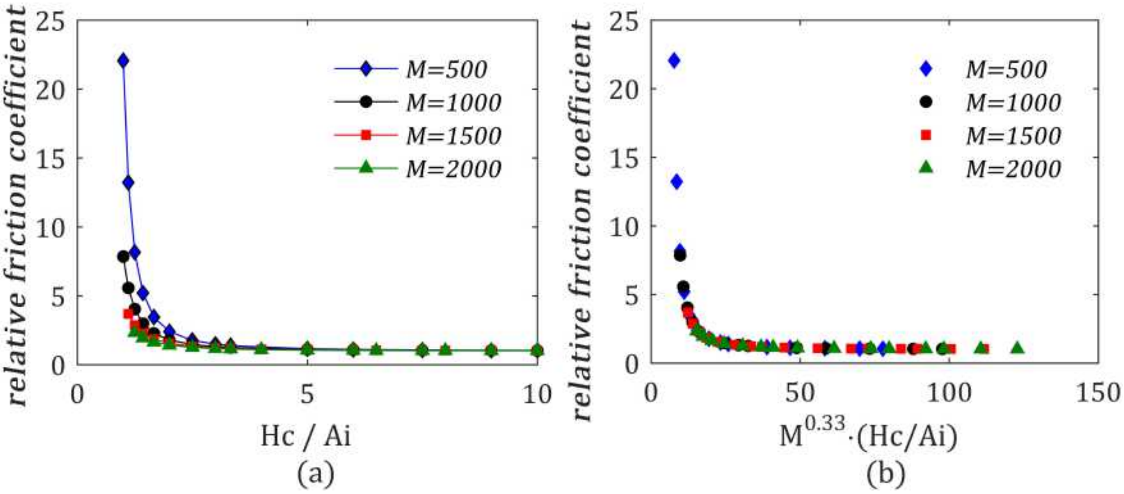

Figure 3.10: Effect of the load parameter M on the relative friction coefficient for $L = 10$ and $\lambda/a_h = 0.5$: (a) relative friction coefficient as a function of Hc/Ai, (b) relative friction coefficient as a function of $M^{0.33} \cdot (Hc/Ai)$

Figure 3.10 displays the influence of the load parameter M on the relative friction coefficient for $L = 10$ and $\lambda/a_h = 0.5$. From Figure 3.10 (a), one can observe that for each M value, there is a single curve. As M increases, the relative friction coefficient decreases, meanwhile each single curve has a small left-shift. It seems that there is a scaling factor can be used to combine all curves together. Figure 3.10 (b) shows that $M^{0.33}$ is an appropriate factor to scale all curves.

Figure 3.11 shows the influence of the material parameter L on the relative friction coefficient for $M = 1000$ and $\lambda/a_h = 0.5$. From Figure 3.11 (a), one can observe that the parameter L affects the relative friction coefficient. As L increases, the relative friction coefficient increases, each single curve has a small right-shift. Once again, there exists a scaling parameter $L^{-1.1}$ which can be applied to shift all curves together (shown in Figure 3.11 (b)).

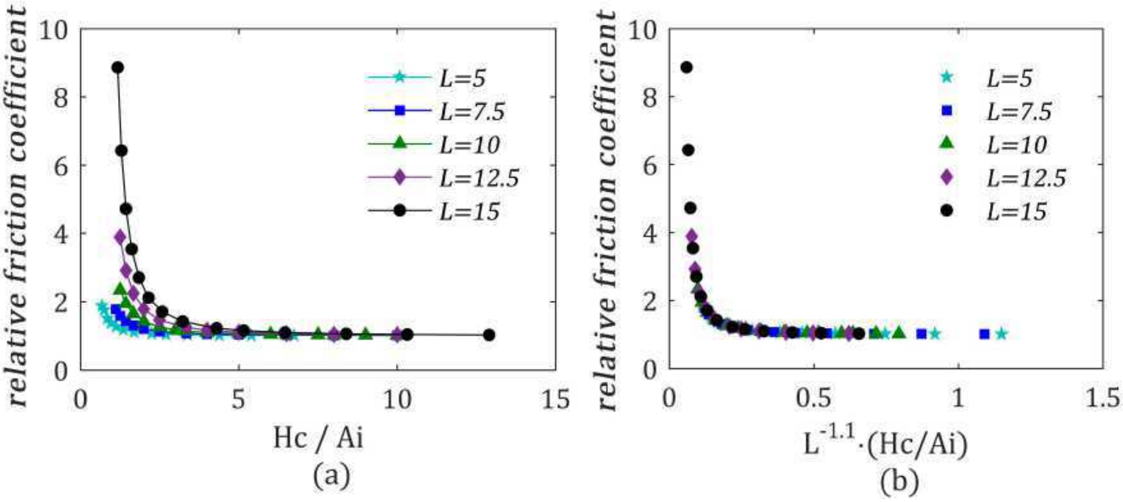

(a)

(b)

Figure 3.11: Effect of material parameter L on the relative friction coefficient for $M = 2000$ and $\lambda/a_h = 0.5$: (a) relative friction coefficient as a function of Hc/Ai, (b) relative friction coefficient as a function of $L^{-1.1} \cdot (Hc/Ai)$

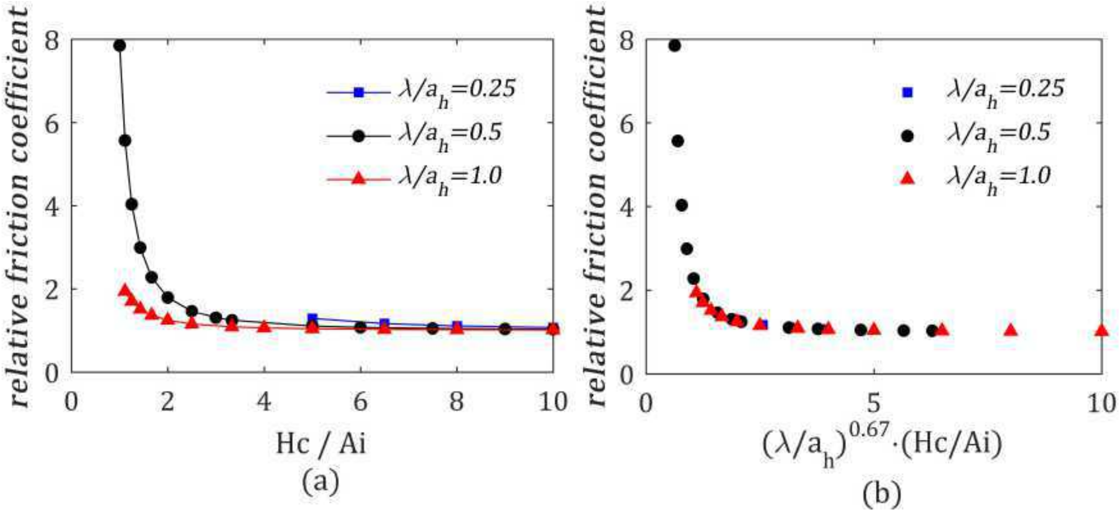

(a)

(b)

Figure 3.12: Effect of wavelength λ/a_h on the relative friction coefficient for $M = 1000$ and $L = 10$: (a) relative friction coefficient as a function of Hc/Ai, (b) relative friction coefficient as a function of $(\lambda/a_h)^{0.67} \cdot (Hc/Ai)$

The relative friction coefficient is affected not only by the operating conditions M and L, but also by the wavelength of the surface waviness. Figure 3.12 describes the effect of the wavelength λ/a_h on the relative friction coefficient for $M = 1000$ and $L = 10$. As λ/a_h increases, the relative friction coefficient decreases, each single curve has a small left-shift (shown in Figure

3.12 (a)). The parameter $\lambda/a_h^{0.67}$ is a suitable factor to unify those curves (shown in Figure 3.12 (b)).

Figure 3.13 presents the relative friction coefficient as a function of the classical "lambda ratio" Hc/Ai for many different operating conditions. This figure shows that for each operating condition, a very smooth curve is obtained, however, one does not obtain a single curve as for the low pressure case using the parameter Hc/Ai. According to the Amplitude Reduction Theory [53, 58], for very high pressures, the surface roughness will deform. Instead of using this simple parameter Ai or a measured surface roughness parameter σ, it is better to use the deformed parameter Ad.

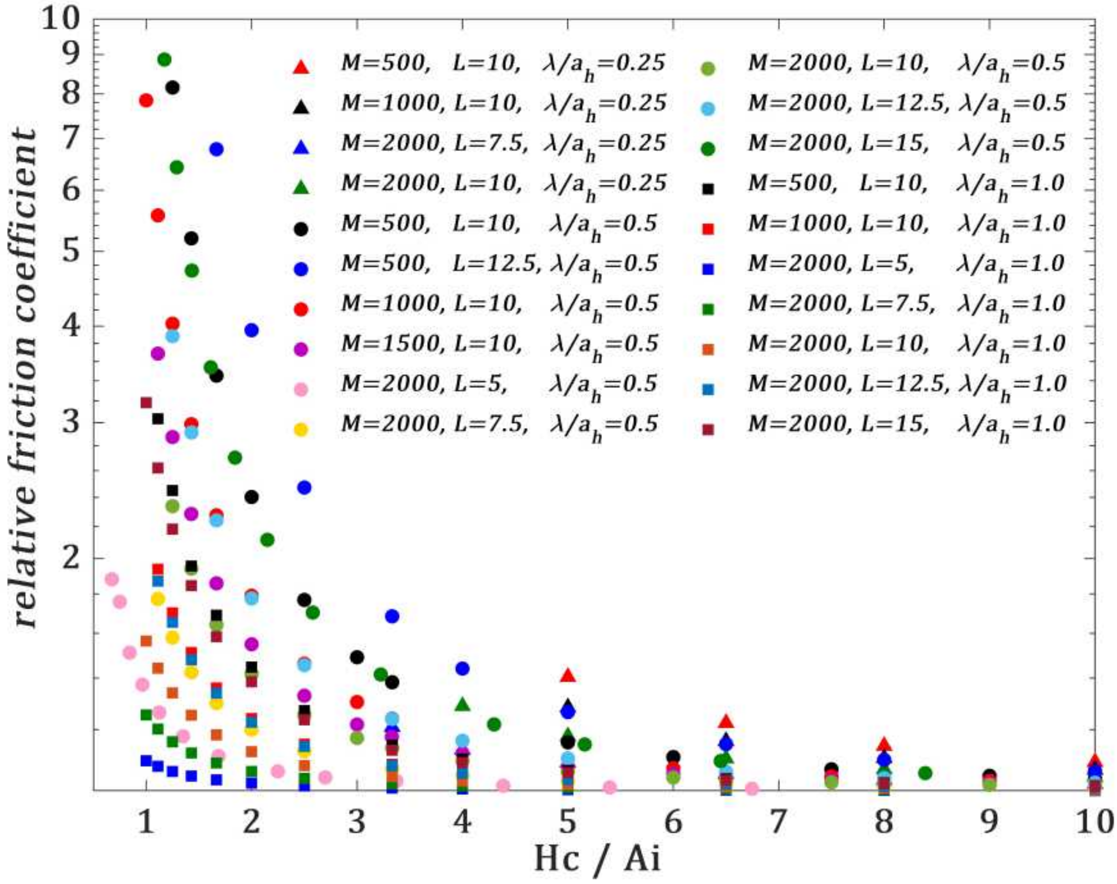

Figure 3.13: Relative friction coefficient as a function of the classical parameter "lambda ratio" i.e. Hc/Ai for a large range of operating conditions.

Employing the scaling factors of Figures 3.10-3.12, it is possible to combine all results obtained for different values of λ/a_h, M, L as well as Hc/Ai into a single curve using a dimensionless parameter θ_2. Figure (3.14) shows the relative friction coefficient as a function of the new parameter θ_2 for $500 \le M \le 2000$, $5 \le L \le 15$, $0.25 \le \lambda/a_h \le 1.0$ and $1.0 \le Hc/Ai \le 10$. After curve-fitting, the single curve can be described by the following equation:

$$\frac{\mu_r}{\mu_s} = 1 + 0.56\,\theta_2^{-2} + 0.23\,\theta_2^{-4} \tag{3.18}$$

where $\theta_2 = L^{-1.1} M^{0.33} (\lambda/a_h)^{0.67} (Hc/Ai)$. The physical justification of this scaling parameter can be understood from a simplified analysis given in Appendix C.

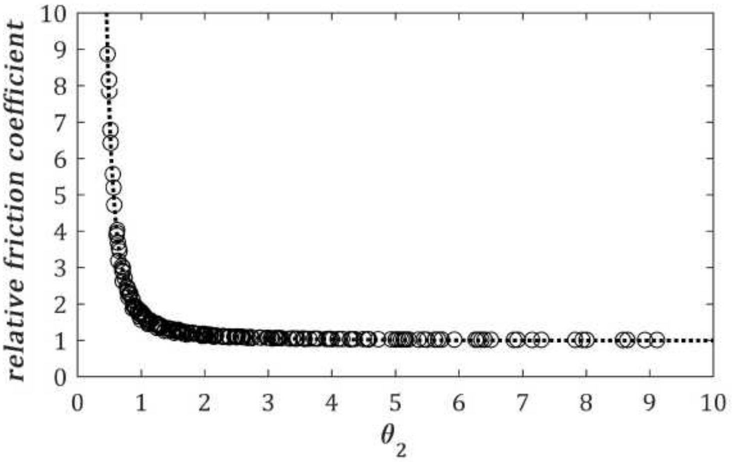

Figure 3.14: Relative friction coefficient as a function of the new parameter θ_2, simulation results: black circles; fitted curve: the black dashed line.

3.6 Effect of surface anisotropy

The previous section demonstrated the influence of the operating conditions and the wavelength on the relative friction coefficient for the isotropic case. Figure 3.8 shows that the surface anisotropy affects the relative friction coefficient under the same operating conditions. This section describes the influence of the surface anisotropy on the relative friction coefficient in more detail.

3.6.1 Longitudinal and transverse wavy cases

Figure 3.15 shows the relative friction coefficient (μ_r/μ_s) as a function of Hc/Ai for different r ($1 \leq r \leq 32$) values. It can be observed that the results of the longitudinal case show the same trend as those of the isotropic wavy case ($r = 1$). That is, a decreasing trend of the relative friction coefficient when Hc/Ai increases. For each r value a single curve exists but it shifts to the left compared to the curve with $r = 1$. For the case considered, the relative friction coefficient monotonically decreases as r increases (shown in the right small figure in Figure 3.15).

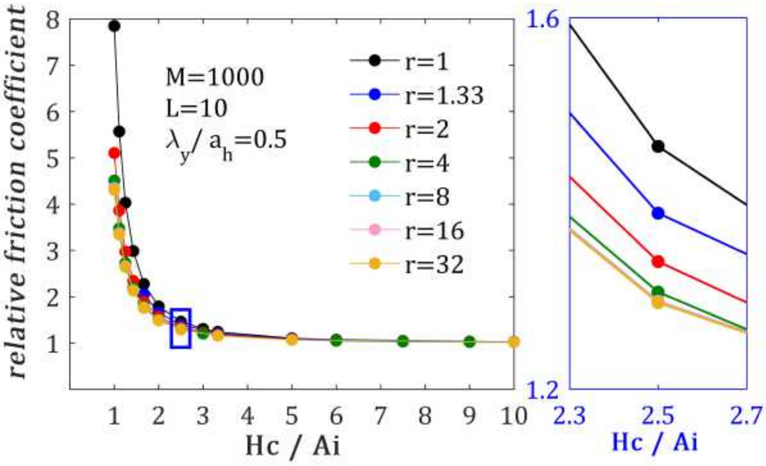

Figure 3.15: Relative friction coefficient (μ_r/μ_s) as a function of Hc/Ai for different r ($1 \leq r \leq 32$) values for: $M = 1000$, $L = 10$ and $\lambda_y/a_h = 0.5$ (left), zoom from 2.3 – 2.7 (right).

From Figure 3.15, one can conclude that the results for $r = 16$ and for $r = 32$ are almost identical and the left shift is limited. It is assumed that a function can be used to shift all results onto a single curve. The single curve is obtained as shown in Figure 3.16 when the horizontal coordinate Hc/Ai in Figure 3.15 is multiplied by the following function:

$$\mathrm{ff}(r) = 1.23 - 0.23(\frac{1}{r})^{1.4} \tag{3.19}$$

in order to distinguish the surface roughness anisotropy function in Equation 3.17, in this work, the anisotropy function is marked as ff(r).

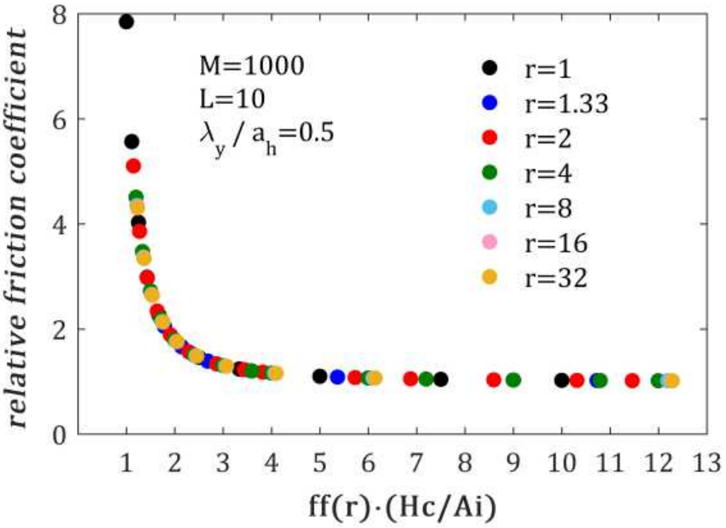

Figure 3.16: Relative friction coefficient (μ_r/μ_s) as a function of ff$(r) \cdot (Hc/Ai)$ for different r ($1 \leq r \leq 32$) values for: $M = 1000$, $L = 10$ and $\lambda_y/a_h = 0.5$.

The transverse case is studied for $M = 1000$, $L = 10$ and $\lambda_x/a_h = 0.5$. Figure 3.17 shows the relative friction coefficient (μ_r/μ_s) as a function of Hc/Ai for different r ($0 \leq r \leq 1$) values. Results for the transverse case are more complicated. It can be observed from Figure 3.17 that as r increases (r varies from 0 to 0.33), the relative friction coefficient decreases gradually (shown as blue lines) while for r varying from 0.4 to 1, the relative friction coefficient increases (shown as black lines).

Once again, a function can be found to scale all results and form a single curve as shown in Figure 3.18.

$$\mathrm{ff}\ (r) = \frac{2.7r^2 + 0.1}{r^3 + 1.7r^2 + 0.1} \tag{3.20}$$

Combining all anisotropy factors, the anisotropy function is expressed as:

$$\mathrm{ff}\ (r) = \begin{cases} (2.7r^2 + 0.1)/(r^3 + 1.7r^2 + 0.1), & \text{if } r < 1 \\ 1.23 - 0.23(1/r)^{1.4}, & \text{otherwise} \end{cases} \tag{3.21}$$

where $r = \lambda_x/\lambda_y$. Figure 3.19 shows the comparison of the simulation results of the anisotropy factors and the final fitted function (shown as Equation 3.21).

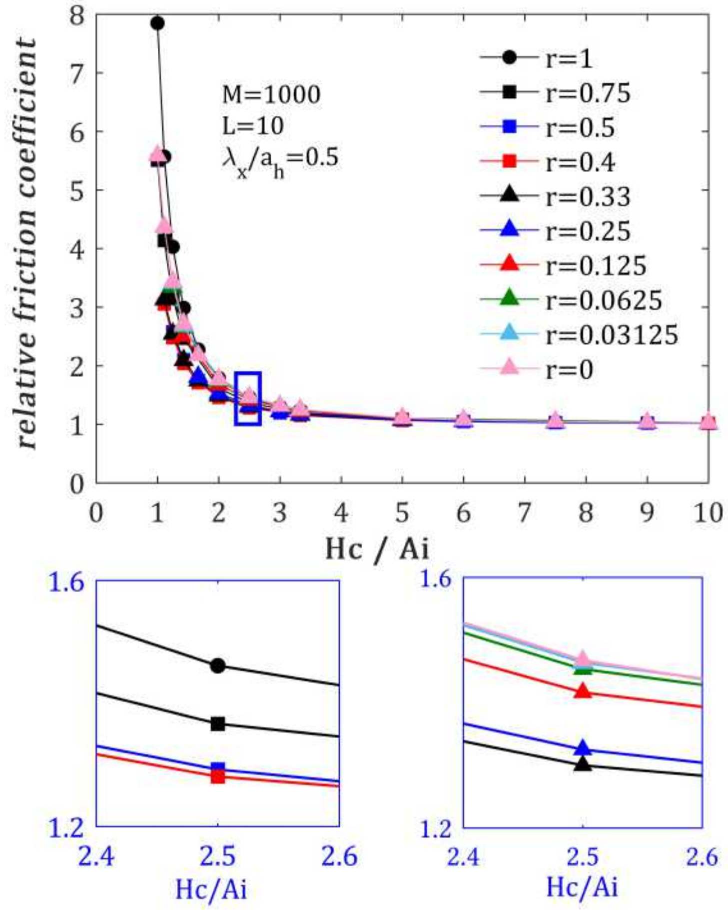

Figure 3.17: Relative friction coefficient (μ_r/μ_s) as a function of (Hc/Ai) for different r $(0 \le r \le 1)$ values for: $M = 1000$, $L = 10$ and $\lambda_x/a_h = 0.5$(upper), zoom from $2.4-2.6$ (lower).

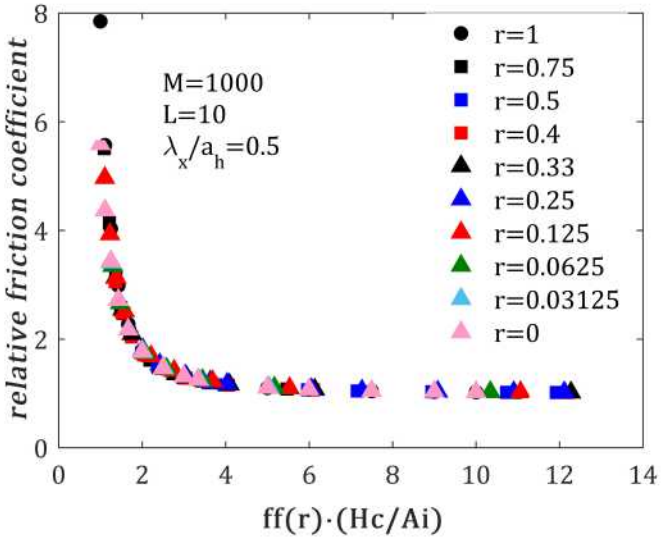

Figure 3.18: Relative friction coefficient (μ_r/μ_s) as a function of $\text{ff}(r) \times (Hc/Ai)$ for different r $(0 \le r \le 1)$ values for: $M = 1000$, $L = 10$ and $\lambda_x/a_h = 0.5$.

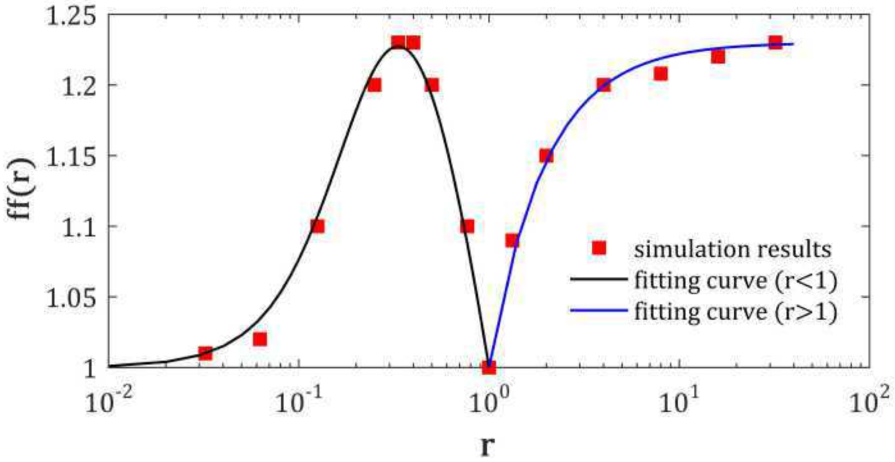

Figure 3.19: ff (r) as a function of r. Numerical results: red squares. Fitted curve: solid lines.

3.6.2 Purely longitudinal wavy case

Study [51] showed that the transient purely longitudinal case remains a stationary problem. This phenomenon can also be seen in the current study. Figure 3.20 presents the comparison between the transient results and the stationary results for $M = 1000$, $L = 10$, $Hc/Ai = 2$, $\lambda_y/a_h = 1.0$ and $\lambda_x = \infty$. In order to compare these results, the stationary result is also plotted as a function of the dimensionless time T in Figure 3.20. Figure 3.20 shows that the value of the relative friction coefficient is the same as the value of the stationary case, i.e. $\mu_r/\mu_s = 1.673$. This is due to the waviness term (Equation 3.1) reduces to $RR(X,Y) = Ai \times \cos(2\pi \frac{Y}{\lambda_y/a_h})$, which is a time-independent term.

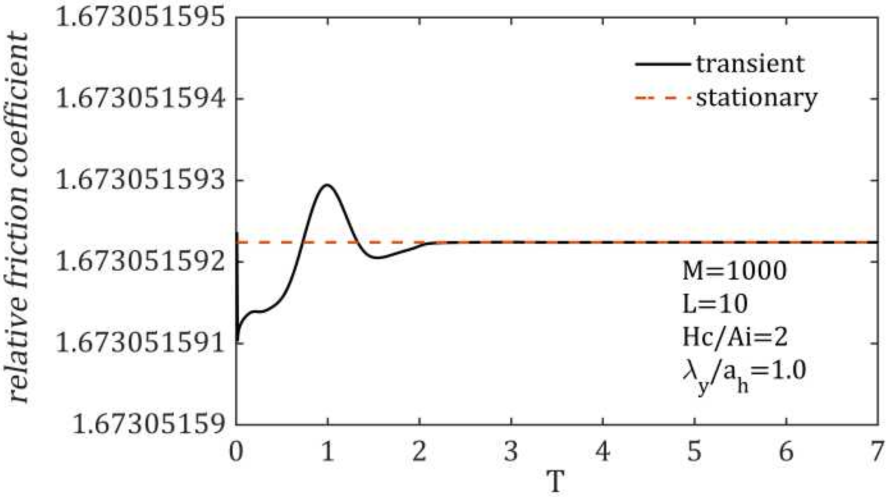

Figure 3.20: Comparison between the transient relative friction coefficient and that of the stationary case. Transient results: black line. Stationary results: magenta dash-dotted line.

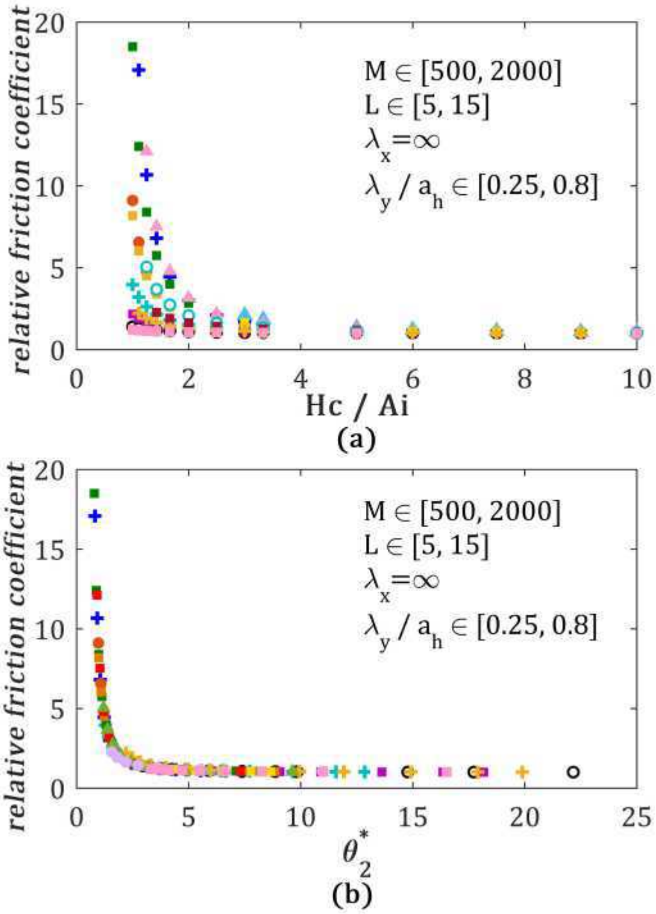

Figure 3.21: Relative friction coefficients for the purely longitudinal wavy case: (a) relative friction coefficient as a function of original "lambda ratio" Hc/Ai parameter, (b) relative friction coefficient as a function of the new parameter θ_2^*

The influence of the waviness anisotropy on friction can be found in Table 3.2. It is reported that with r increasing from 1 to 32 the relative friction coefficient (μ_r/μ_s) decreases, while the case $r = \infty$ predicts the highest relative friction coefficient value.

Table 3.2: Relative friction coefficient versus different surface anisotropy parameters for: $M = 1000$, $L = 10$, $\lambda_y/a_h = 0.5$ and $Hc/Ai = 2$.

r	1	2	4	8	16	32	∞
μ_r/μ_s	1.789	1.566	1.508	1.491	1.489	1.487	2.041

Figure 3.21 gives the results of the relative friction coefficient for the purely longitudinal wavy case for a relative large range of operating conditions: $M \in [500, 2000]$, $L \in [5, 15]$ and $\lambda_y/a_h \in [0.25, 0.8]$. As usual, in Figure 3.21 (a), a very smooth curve as a function of Hc/Ai for each operating condition. While, the old scaling parameter θ_2 can not scale all cases together. For the purely longitudinal cases considered, there is indeed a new parameter θ_2^* expressed as Equation (3.22), and shown in Figure 3.21 (b) to unify all cases onto a single curve. The operating conditions are: $500 \le M \le 2000$, $5 \le L \le 15$ and $0.25 \le \lambda/a_h \le 0.8$.

$$\theta_2^* = M^{0.4} L^{-1.2} [-1.1(\lambda_y/a_h)^2 + 2.1(\lambda_y/a_h) + 0.2](Hc/Ai). \tag{3.22}$$

3.7 Conclusion

In this chapter, the relative friction coefficient is predicted by means of numerical simulation for a large range of transient EHL operating condition and surface waviness anisotropy ($r = \lambda_x/\lambda_y$). A relation is derived for the relative friction coefficient for isotropic and anisotropic harmonic surfaces. For the isotropic wavy case, all relative friction coefficient values can be unified onto a single curve applying a dimensionless parameter θ_2. For anisotropic wavy cases, a roughness anisotropy function ff (r) is used to scale all results together, when the same operating conditions are considered. Finally, results of all cases can be combined into a single equation:

$$\frac{\mu_r}{\mu_s} = 1 + 0.56[\mathrm{ff}\,(r)\theta_2]^{-2} + 0.23[\mathrm{ff}\,(r)\theta_2]^{-4} \tag{3.23}$$

where

$$\mathrm{ff}\,(r) = \begin{cases} (2.7r^2 + 0.1)/(r^3 + 1.7r^2 + 0.1), & \text{if } r < 1 \\ 1.23 - 0.23(1/r)^{1.4}, & \text{otherwise} \end{cases}$$

and $\theta_2 = M^{0.33}L^{-1.1}(\lambda/a_h)^{0.67}(Hc/Ai)$ with $\lambda = \min(\lambda_x, \lambda_y)$.

However, from a lubrication point of view, the purely longitudinal wavy case ($r = \infty$) has a very different frictional behavior. A separate scaling parameter θ_2^* is obtained for the purely longitudinal wavy case.

Early work on conformal contacts showed that the onset of mixed lubrication regime was roughly around a "lambda ratio" equal to 3, in which the "lambda ratio" is defined as the ratio of oil film thickness to the combined surface roughness. The current work reveals that besides the classical "lambda ratio" parameter, the operating conditions as well as the surface topography play an important role on the onset of the mixed lubrication regime.

Chapter 4

Friction of complex rough surfaces

Contents

4.1 Introduction

The previous chapter has already predicted the friction increase for simple harmonic surface waviness, while the range of wavelengths is limited. In reality, the real surface roughness is more complicated. It contains very different wavelengths and amplitudes. On the other hand, the full numerical simulation is time-consuming for real rough surfaces. In this chapter a rapid prediction method based on the roughness power spectral density (PSD) is provided to predict the friction increase due to the roughness. Section 4.2 will describe this method in the first place. Section 4.3 tests this method for an artificial fractal surface roughness. Finally, section 4.4 predicts the transition of the full-film to the mixed lubrication regime by applying this method for real measured surface roughness.

4.2 Power spectral density friction method

4.2.1 PSD friction model

The power spectral density (PSD) is a mathematical tool that decomposes a rough surface into harmonic components of different frequencies [109], which enables the pressure increase to be calculated analytically for each frequency component. Subsequently, the friction variations for the whole rough surface can be obtained. At last, the relative friction coefficient is obtained. The calculation process is as follows:

A rough surface topography $rr_{x,y}$ can be expressed in the frequency domain by means of the Fourier transform:

$$rr_{q_x,q_y} = (\frac{4}{N_x N_y})\sum_{x,y}(rr_{x,y})e^{-i(q_x x+q_y y)} \tag{4.1}$$

where $rr_{x,y}$ is the discrete form of the surface roughness $rr(x,y)$, q_x and q_y are the wavenumbers in the x and y direction respectively. In general, Equation 4.1 is computed by the fast Fourier transform (FFT) algorithm.

Combine Equation 4.1 and Equation 3.17, the deformed surface roughness $rr^d_{q_x,q_y}$ in the frequency domain is:

$$rr^d_{q_x,q_y} = (\frac{A_d}{A_i})_{q_x,q_y}\cdot|rr_{q_x,q_y}|. \tag{4.2}$$

According to the relation between the pressure and the elastic deformation of the waviness given in Appendix D, the pressure increase in the frequency domain follows the expression below

$$\delta p_{q_x,q_y} = \frac{\pi E'}{2k(r)\lambda}(rr_{q_x,q_y} - rr^d_{q_x,q_y}) \tag{4.3}$$

where λ is defined as $\lambda = \min(2\pi/q_x, 2\pi/q_y)$. With the inverse discrete Fourier transform, the pressure increase in the space domain is obtained:

$$\delta p_{x,y} = (\frac{4}{N_x N_y})\sum_{q_x,q_y}\delta p_{q_x,q_y}\cdot e^{i(q_x x+q_y y)}. \tag{4.4}$$

According to the friction force Equation 3.14, the ratio of the shear stress τ_r/τ_s can be derived as:

$$\frac{\tau_r(x,y)}{\tau_s(x,y)} = \frac{\eta_r(x,y)}{\eta_s(x,y)}\cdot\frac{h_s(x,y)}{h_r(x,y)} = \frac{\eta_r(x,y)}{\eta_s(x,y)}\cdot\frac{h_s(x,y)}{h_s(x,y)-a_d(x,y)} \tag{4.5}$$

It is easy to obtain the shear stress distribution $\tau_s(x,y)$ for the smooth surface case, where the pressure distribution for the smooth surface case can be replaced by a semi-elliptical pressure distribution:

$$p_s(x,y) = \begin{cases} p_h\sqrt{1-(x/a_h)^2-(y/a_h)^2}, & \text{if } x^2+y^2 \le a_h^2 \\ 0, & \text{otherwise.} \end{cases} \tag{4.6}$$

Afterwards, the pressure distribution for roughness cases is computed by $p_s + \delta p$. The shear stress distribution $\tau_r(x,y)$ for a rough surface case is obtained as:

$$\tau_r(x,y) = \frac{\eta_r(x,y)}{\eta_s(x,y)}\cdot\frac{h_s(x,y)}{h_s(x,y)-a_d(x,y)}\cdot\tau_s(x,y). \tag{4.7}$$

Finally, the shear forces for both the smooth case and the rough case are computed by integrating the shear stress $\tau_s(x,y)$ and $\tau_r(x,y)$, respectively. The relative friction coefficient is then calculated according to Equation 3.15. A detailed description of the prediction process of the relative friction coefficient is shown in Figure 4.1.

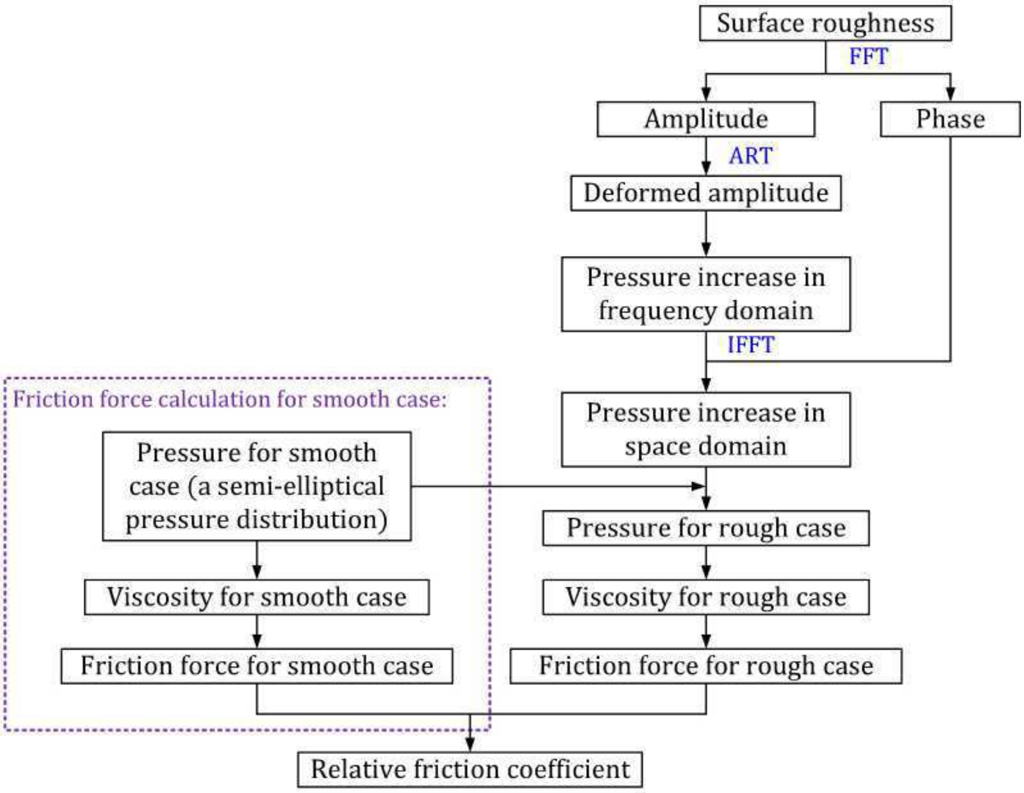

Figure 4.1: Flow chart for the relative friction coefficient prediction

4.2.2 Model validation

To validate the model described in subsection 4.2.1, the relative friction coefficient evaluated from a full numerical simulation is compared with that predicted by PSD under the same operating conditions. The same calculation domain, mesh size and slide-to-roll ratio as in subsection 3.3.2 are used here. An artificial fractal rough surface is chosen to validate the model mentioned in the previous subsection and the operating condition parameters are listed in Table 4.1.

Table 4.1: Operating condition parameters.

Parameter	Value	Units
w	600	N
u_r	0.84	m/s
R_x	0.018	m
E'	2.26×10^{11}	Pa
α	2.2×10^{-8}	Pa^{-1}
η_0	4×10^{-2}	Pa·s
h_c	0.233	μm
σ	5×10^{-8}	m
$L_x = L_y$	8.29×10^{-4}	m
q_r	0	m^{-1}
Hurst exponent	0.8	

Table 4.2 presents the friction ratio as a function of the number of mesh points for the two methods. The results predicted by the two schemes are basically identical. The ratio of the friction coefficients predicted by the PSD method changes slightly (< 0.08%) with decreasing mesh size. However, in the full numerical simulation, a large mesh size leads to a relative large error. This is because some high frequency components of the rough surface can not be correctly represented on such a large mesh size. In this chapter, the precision of the numerical results simulated by a 513 × 513 points is considered acceptable.

Table 4.2: Relative friction coefficients as a function of the mesh points for two prediction schemes.

Mesh points $N_x \times N_y$	$hx = hy$	μ_r/μ_s(PSD)	μ_r/μ_s(EHL)
257 × 257	1/64	1.534	1.487
513 × 513	1/128	1.534	1.518
1025 × 1025	1/256	1.534	1.510

4.3 The artificial surface roughness

In this section, an artificial fractal surface roughness is selected to test the rapid friction prediction method.

4.3.1 Surface roughness power spectrum

Many parameters like the root-mean square (R_q), standard deviation (σ), skewness (Sk), kurtosis (K) et al. are employed to describe a measured surface roughness [142]. The power spectral density (PSD) is perhaps the most used method for the surface description. Reference [143] gives the calculation of the PSD for a surface roughness:

$$C^{2D}_{q_x,q_y} = (L_x L_y)^{-1} |rr_{q_x,q_y}|^2 \tag{4.8}$$

where L_x and L_y are the length of the measured surface roughness profiles in the x and y directions. A 2D surface roughness is shown in Figure 4.2 (a) and it can be represented as a 2D PSD C^{2D} in frequency space. When the surface is isotropic, its power spectral density is radially symmetric (reported in Figure 4.2 (b)).

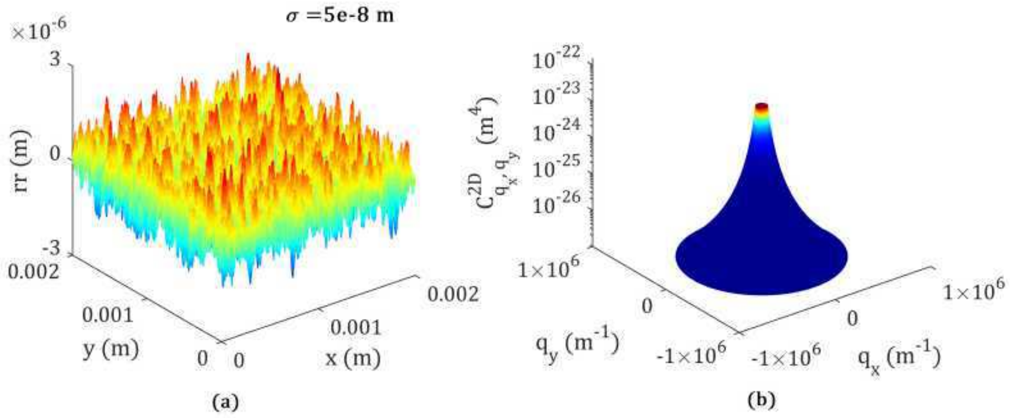

Figure 4.2: Surface roughness (a) and its 2D power spectral density (b)

Many real rough surfaces show self-affine characteristic. A surface is self-similar when it has the same statistical properties as a magnified version of itself [144].The power spectral density of a self-affine surface often follows the following equation [109, 145] and shown in Figure 4.3:

$$C^{iso}(q) = \begin{cases} C_0, & \text{if } q_L \le q < q_r \\ C_0 q^{-2-2H}, & \text{if } q_r \le q < q_s \\ 0, & \text{otherwise} \end{cases} \tag{4.9}$$

in which $q = \sqrt{q_x^2 + q_y^2}$, q_L is the long-wavelength cut-off wave vector, q_r is the long-wavelength roll-off wave vector and q_s is the short-wavelength cut-off wave vector. H is the Hurst exponent, which is related to the fractal dimension D_f of the surface [144] : $H = 3 - D_f$.

Once the power spectral density of a rough surface is obtained, other parameters like the RMS roughness h_{rms}, RMS slope h'_{rms} and RMS curvature h''_{rms} can be derived [146].

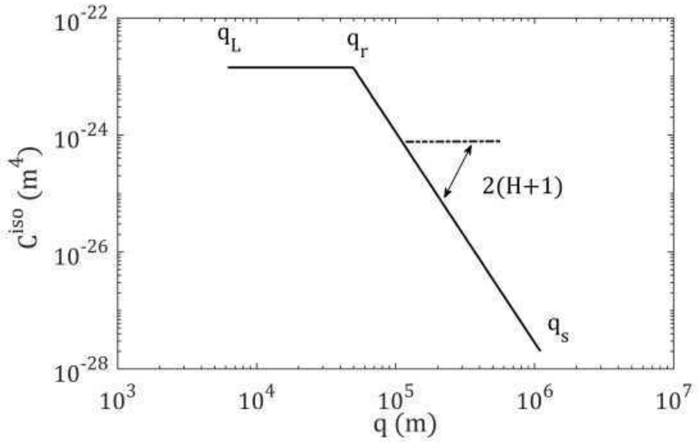

Figure 4.3: Power spectral density C^{iso} of the self-affine surface(Figure 4.2(a)) with $H = 0.8$.

4.3.2 Friction increase prediction of a rough surface

The friction increase is determined by the non-linear viscosity variations from pressure variations caused by roughness deformation. In this subsection, these variables are plotted by employing the artificial surface roughness with $q_r = 50000\ \text{m}^{-1}$ shown in Figure 4.4.

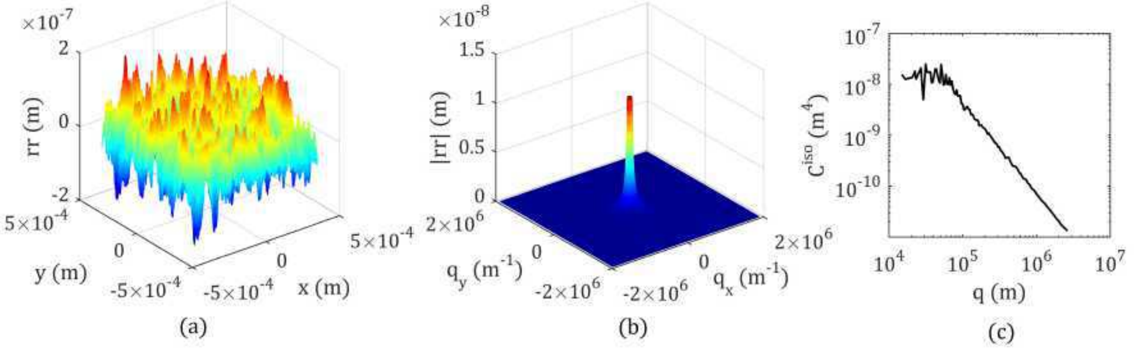

Figure 4.4: The selected artificial surface roughness (a), amplitude distribution of this surface roughness (b) and its power spectral density (c).

The first step is to compute the deformed surface roughness based on the Amplitude Reduction Theory [53] with the operating condition in Table 4.1. Figure 4.5 (a) shows the ratio of the deformed amplitude and the initial amplitude described by Equation 3.17. Combining the initial amplitude distribution in Figure 4.4, the deformed surface roughness distribution is depicted in Figure 4.5 (b).

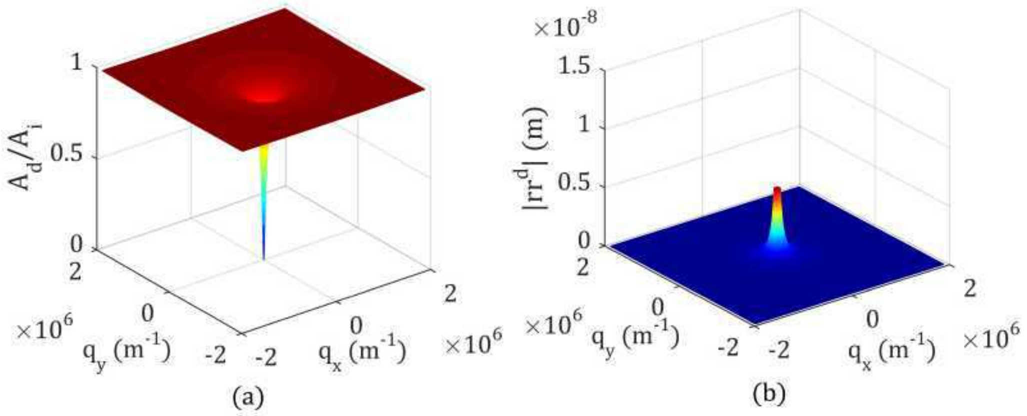

Figure 4.5: The ratio of the deformed amplitude and the initial amplitude fitted as Equation (3.17) (a) and the deformed surface roughness in frequency domain (b).

Figure 4.6 compares the initial surface roughness with the deformed surface roughness. It can be observed that the initial surface roughness is deformed.

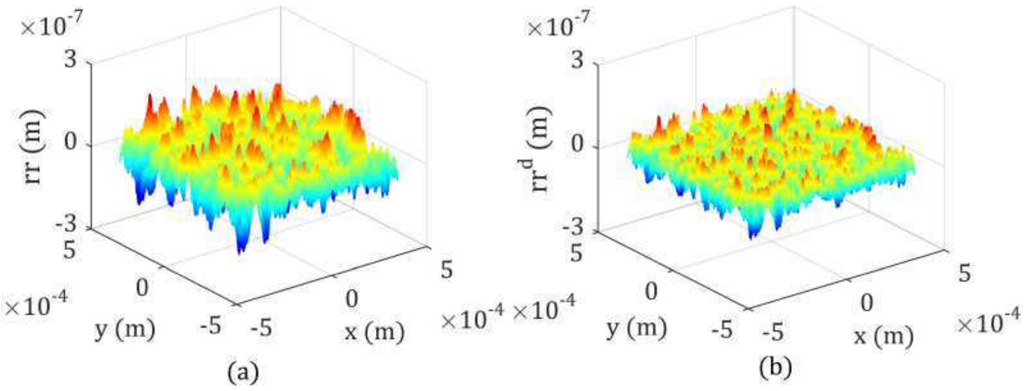

Figure 4.6: Comparison between the initial surface roughness (a) and the deformed surface roughness (b).

Subsequently, the pressure increase can be computed by Equation 4.3 and Equation 4.4. Figure 4.7 gives the pressure increase distribution in frequency and space domains, respectively. Then the pressure distribution as well as film thickness distribution for the rough case can be obtained as $p_s + \delta p$ and $h_s - rr^d$ respectively. Shear stress for both cases are predicted by $\eta(u_2 - u_1)/h$, which are shown in Figure 4.8. Those values are unrealistically high, and more complex rheological models are required for an absolute shear stress prediction, but here we are only interested in the relative shear. The shear stress for rough case is higher than that of smooth case, this is because pressure variations caused by roughness deformations make a big contribution to the viscosity. Finally, the friction force is calculated by Equation 3.14 and the relative friction coefficient is given by Equation 3.15. For this rough surface, friction forces for the smooth case and the rough case are $F_s = 1.0606 \times 10^6$ N and $F_r = 1.3624 \times 10^6$ N, respectively. The relative friction coefficient is $\mu_r/\mu_s = 1.2846$.

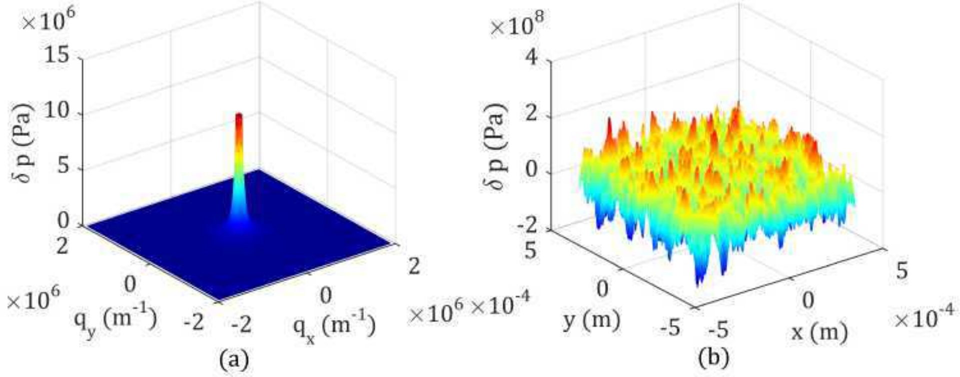

Figure 4.7: Pressure increase distribution in frequency (a) and space (b) domains, respectively.

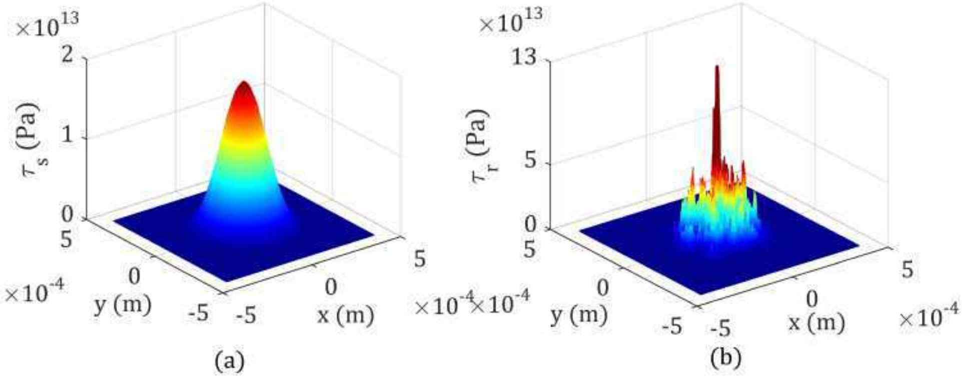

Figure 4.8: Shear stress distributions for the smooth case (a) and for the rough case (b).

4.3.3 Comparison between the EHL simulation and the PSD prediction

The chosen artificial surface topography is generated by means of fractals without a roll-off region. The friction prediction only occurs in the high pressure zone ($X^2 + Y^2 \leq 1.0$), hence in the full numerical EHL simulation this generated surface roughness is located in the high pressure zone (shown in Figure 4.9 (b)). In order to make results keep periodical, the "patch" also needs to be periodical shown in Figure 4.9 (c).

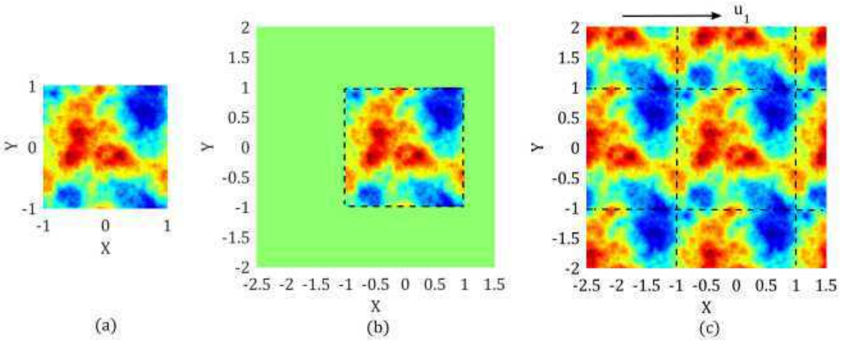

Figure 4.9: The generated surface roughness patch (a), the roughness patch in the high pressure zone (b) and the periodical roughness pattern for full the numerical simulation (c).

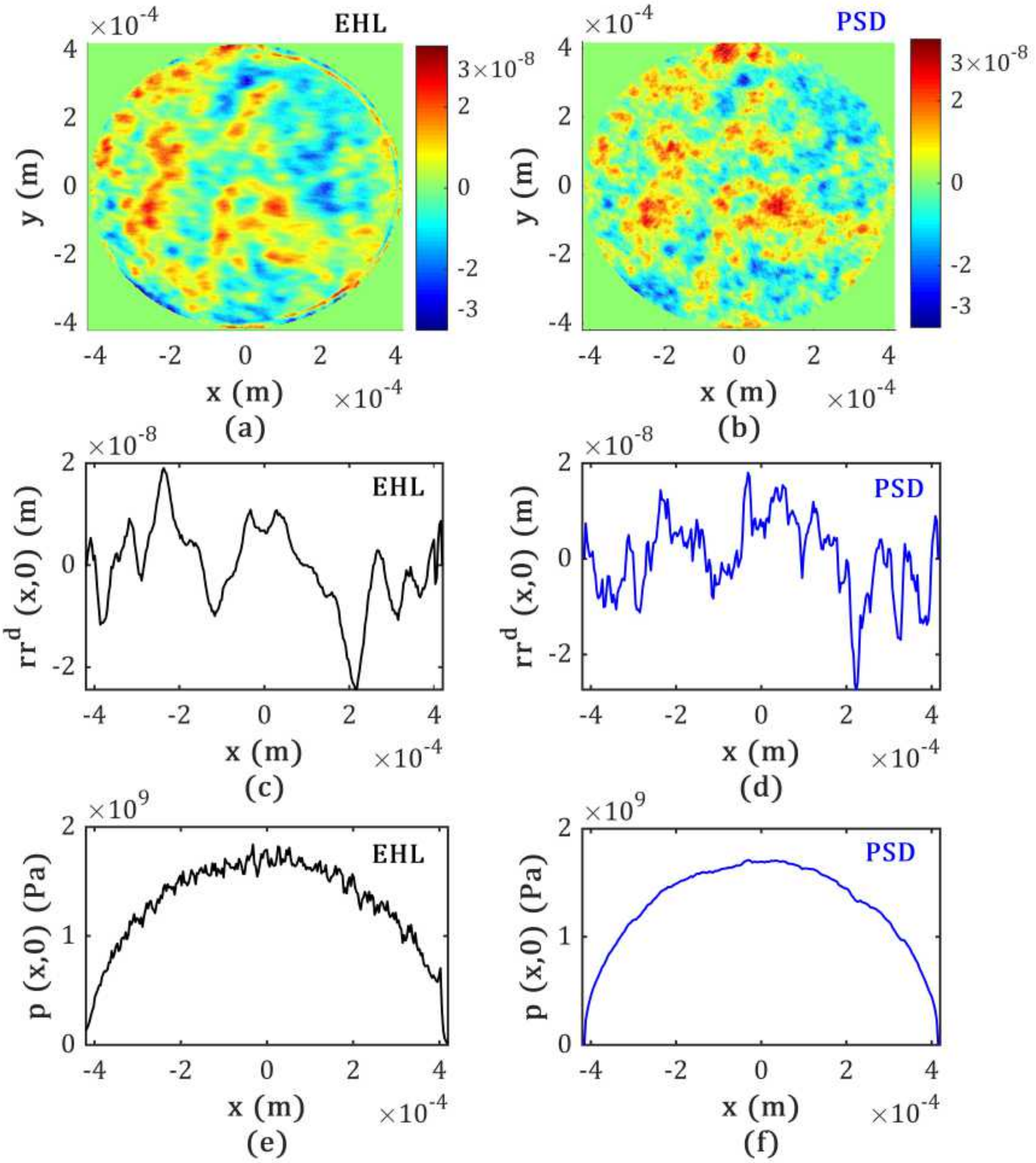

Figure 4.10: Top view of the deformed surface roughness for a specific time step for a full numerical simulation (a) and for a PSD prediction (b). Central line $rr^d(x,0)$ of the deformed surface roughness for the full numerical simulation (c) and for the PSD prediction (d). Central line $p(x,0)$ of the pressure distribution for the full numerical simulation (e) and for the PSD prediction (f).

As shown in the previous subsection, one can find that the deformed amplitude is a fundamental intermediate variable. It is necessary to compare this parameter in the first place. The resulting deformed micro-geometry, of which the original surface topography is shown in Figure 4.9 (a) for a full numerical EHL simulation and a PSD prediction, are presented in Figure 4.10. In terms of numerical simulation results, the deformed micro-geometry rr^d is obtained by $h_s - h_r$ and removing data outside the high-pressure zone ($X^2 + Y^2 \leq 1$). Once again, for this specific surface, the operating conditions are the ones given in Table 4.1 where $M = 1000$ and

$L = 10$. Both the deformed surface topographies rr^d are shown in the same high pressure region. The maximum Hertzian pressure reaches 1.66 GPa and the maximum surface roughness height deformed significantly from 1×10^{-7} m to 3.5×10^{-8} m. In addition, it is shown that the height distribution of the deformed surface roughness from the EHL simulation and the PSD prediction are very similar. Magnitudes of the central line $rr^d(x,0)$ and $p(x,0)$ for both methods are also similar. However, the full numerical simulation shows a more "smooth" results in terms of the deformed surface roughness, this is because small wavelength components can not be represented correctly in full numerical simuialtion. On the other hand, the Amplitude Reduction Theory is valid for small roughness amplitude values, this is the reason for some components shown in subfigure(d) whose maginitude is a little higher. In addition, the pressure distribution predicted by the PSD method is the combination of a semi-elliptical pressure distribution and the pressure deflection i.e. $p_s + \delta p_{x,y}$.

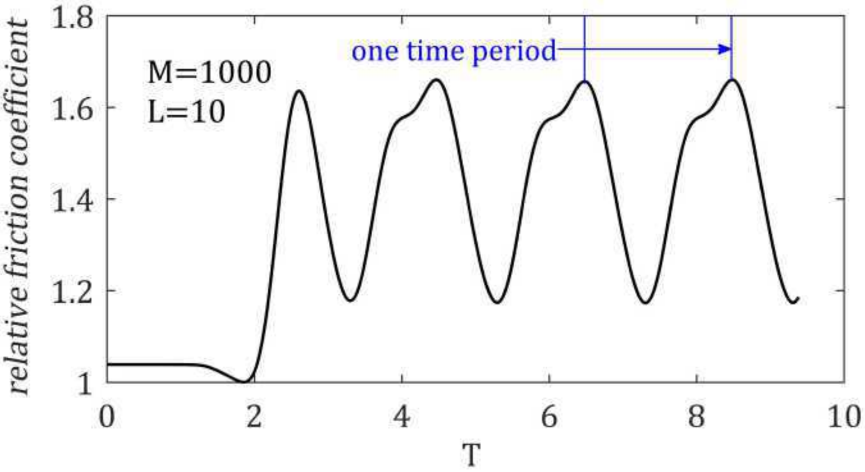

Figure 4.11: The relative friction as a function of dimensionless time employing the surface roughness pattern in Figure 4.9 (c) for the full numerical simulation method.

Figure 4.11 shows the periodical relative friction coefficient variation when the surface roughness pattern in Figure 4.9 (c) is used. As mentioned before, the relative friction coefficient value should be the averaged value of the relative friction coefficient in one time period. The PSD method only gives the value of the relative friction coefficient for one time step, hence one should predict this value for each time step within one time period.

Twenty artificial random rough surfaces are generated (shown in Figure 4.12) with the same input parameters i.e. the standard deviation $\sigma = 5 \times 10^{-8}$ m, lengths of final topography $L_x = L_y = 8.29 \times 10^{-4}$ m, roll–off wave number $q_r = 0$ m^{-1} and Hurst exponent=0.8. These generated roughness are used to compare results from the full numerical simulation as well as the PSD prediction.

The averaged relative friction coefficients for these artificial random rough surfaces are given in Table 4.3, showing that the two different prediction methods give close results. The average deviation is around 8%. It seems that the averaged relative friction values simulated by the full numerical simulation are higher than those predicted by PSD. This is beacuse in PSD prediction pressure spike effects are not taken into consideration. Here we need to notice that when the number of mesh points is selected as 513×513, the calculation time of the full numerical simulation is almost 3 days, this is because more than 2000 time steps are needed. Meanwhile the calculation time of the PSD prediction is only 15 minutes.

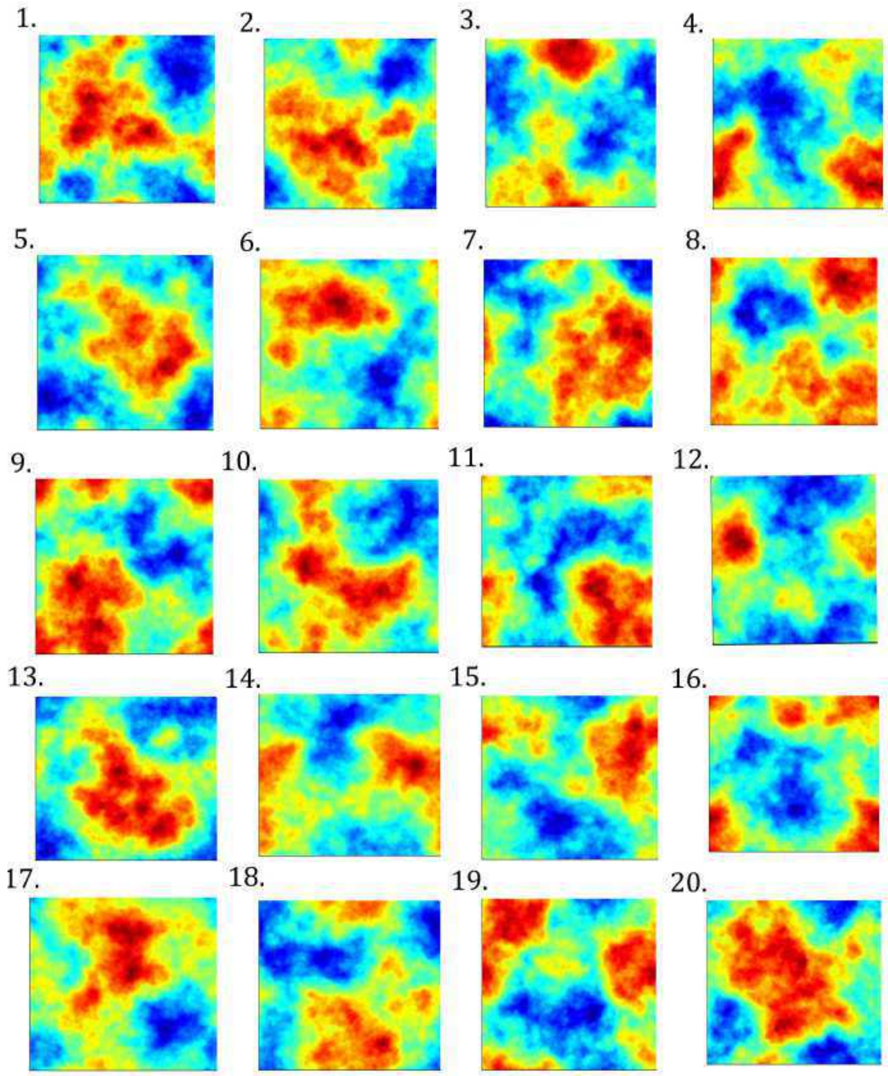

Figure 4.12: Top view of the twenty generated artificial random rough surfaces from N°1 to N°20 with a same standard divation value $\sigma = 0.05\mu$m and a same set of operating conditions listed in Table 4.1.

Table 4.3: The relative friction coefficient obtained by EHL simulation and PSD prediction for 20 artificial random rough isotropic surfaces.

Surface number	μ_r/μ_s(EHL)	μ_r/μ_s(PSD)	Deviation(%)
1	1.40	1.30	7
2	1.45	1.36	6
3	1.12	0.96	14
4	1.15	1.03	11
5	1.42	1.34	6
6	1.23	1.11	9
7	1.37	1.29	6
8	1.14	1.00	11

(to be continue)

Surface number	μ_r/μ_s(EHL)	μ_r/μ_s(PSD)	Deviation(%)
9	1.19	1.07	10
10	1.37	1.29	6
11	1.21	1.09	9
12	1.42	1.37	4
13	1.34	1.36	1
14	1.42	1.36	4
15	1.29	1.17	9
16	1.09	0.93	15
17	1.34	1.24	7
18	1.25	1.12	10
19	1.29	1.19	8
20	1.33	1.22	8

4.4 Measured surface roughness

The surface roughness used in this section is the surface roughness measured from discs employed in friction experiments in Reference [140].

4.4.1 Friction prediction under a specific operating condition

In this subsection, the measured surface roughness dART is collected within an area of 1 cm^2 and having a sampling interval of $hx = hy = 3.653$ μm [140]. This surface roughness is measured from a finished disc made of AISI 52100 steel with a 60 mm diameter and an 8 mm thickness. The surface roughness is then corrected by removing large scales (through a high pass-filtering operation), this corrected surface roughness and the original measured surface roughness are shown in Figure 4.13. The root-mean-square of this surface roughness is $R_q = 0.038\mu$m.

Since the area of high pressure happens in an area of Hertz contact zone, small square windows with the length of $2a_h$ are used to extract effective prediction areas (shown in Figure 4.14). For a measured surface roughness, more effective prediction areas are obtained.

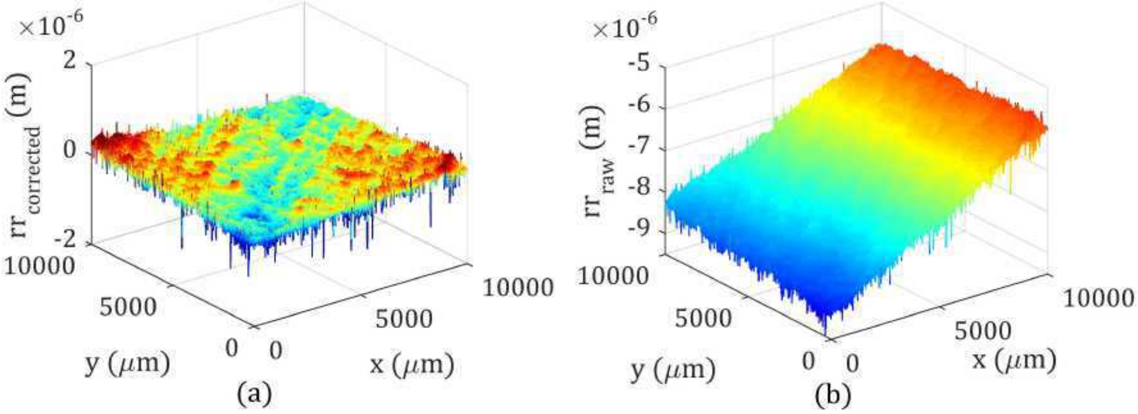

Figure 4.13: Measured surface roughness dART: (a) corrected surface roughness and (b) raw surface roughness.

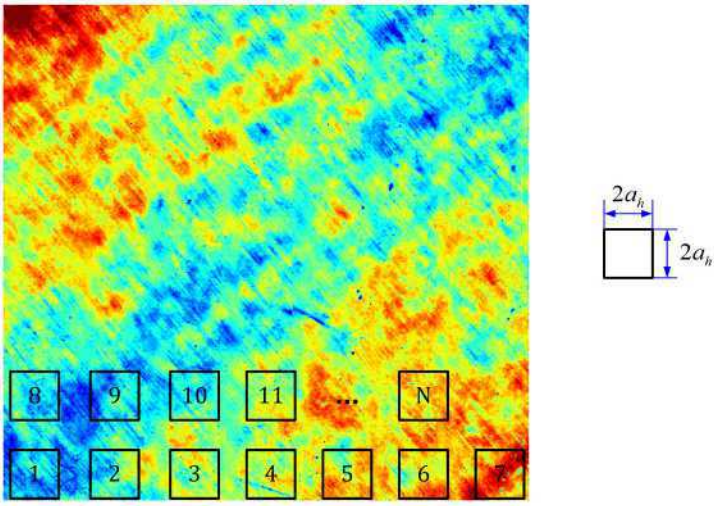

Figure 4.14: Effective prediction areas.

Table 4.4: Measured operating condition and lubricant parameters.

Parameter	Value	Units	Parameter	Value	Units
w	10	N	η_0	0.7590	Pa·s
u_r	0.29	m/s	T_{room}	22	°C
R_x	9.525	mm	SRR	25	%
E'	210	GPa	a_h	87.95	μm
α	2.0×10^{-8}	Pa^{-1}	p_h	617.23	MPa

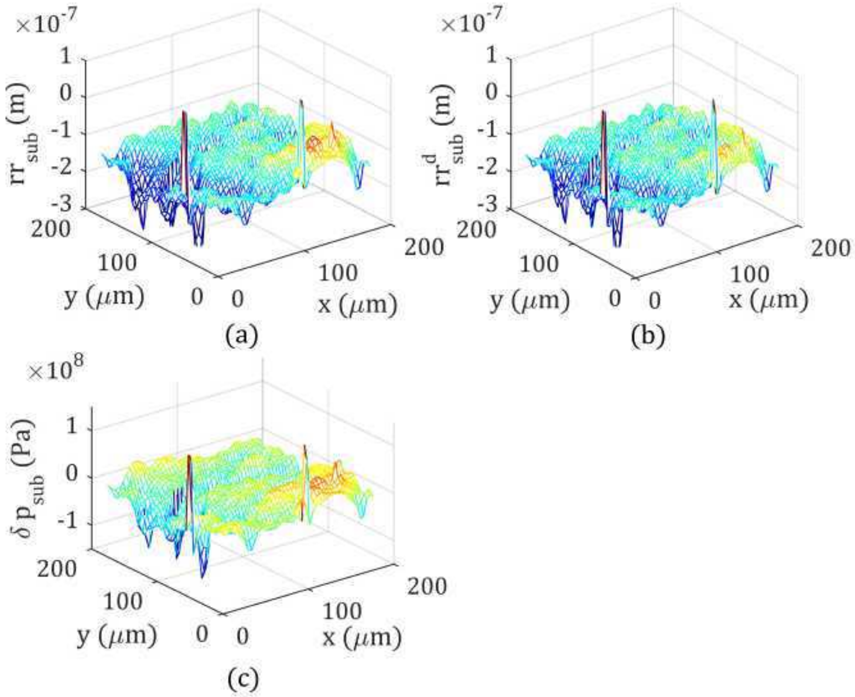

Figure 4.15: An extracted surface patch of dART: (a) surface roughness height of this surface patch; (b) deformed surface patch; (c) pressure fluctuation of the surface patch.

For each extracted sub-surface, the friction prediction process described in subsection 4.2.1 is applied to predict its relative friction coefficient under a specific operating condition. Measured operating conditions and lubricant parameters are listed in Table 4.4. Under this specific operating condition, Moes parameters $M = 9.09$ and $L = 16.23$, Figure 4.15 shows a deformed surface geometry and pressure increase distribution of a surface patch, meanwhile its relative friction coefficient is 1.03.

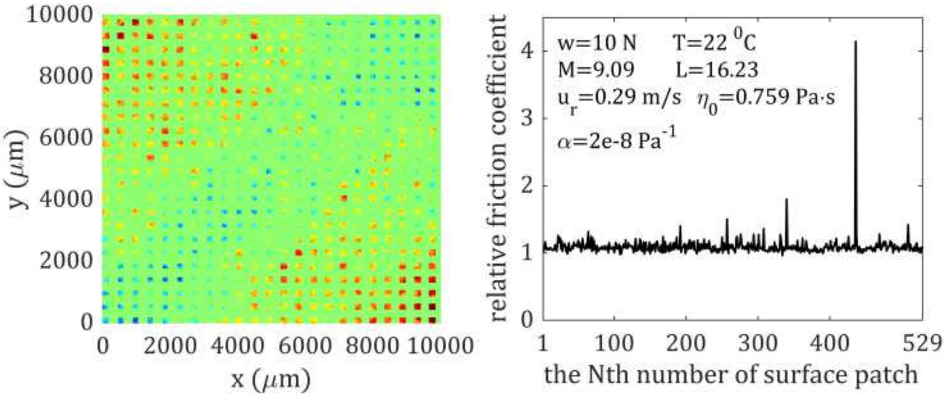

Figure 4.16: Extracted 529 surface patch (left) and their relative friction coefficient values (right).

Figure 4.16 shows the extracted 529 surface patches (left) and their values of the relative friction coefficient (right). For this measured surface roughness dART under this specific operating condition, the relative friction coefficient is defined as the averaged value of that of sub-surfaces. From this figure, one can observe that all relative friction values are smaller than 2 except for a point whose value reaches 4, hence this high value point will be removed. Figure 4.17 shows the corrected relative friction coefficients. At this time, the mean relative friction coefficient is 1.09 and the corresponding standard deviation is 0.071.

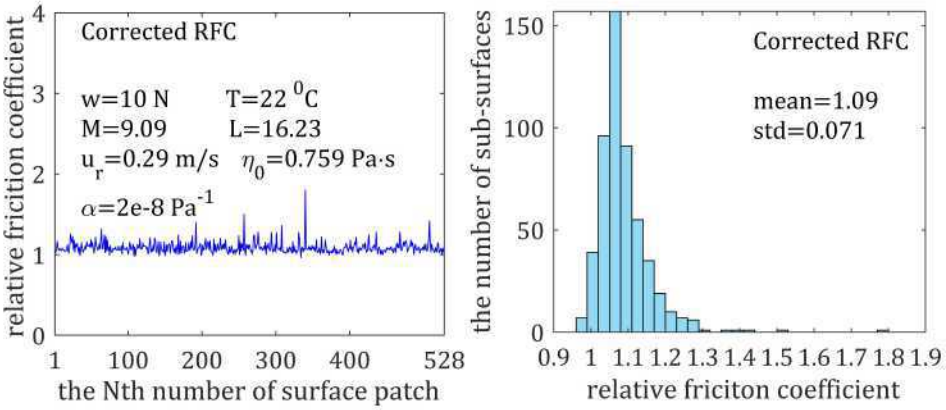

Figure 4.17: Corrected relative friction coefficient values for 528 surface patches (left) and its histogram (right).

Figure 4.18 shows the mean relative friction coefficient as a function of total number of extracted surface patches with operating condition in Table 4.4. It can be observed that the variation of mean relative friction for different the number of surface patch are small. For the sake of saving computation time, the number of surface patch for the rest study is selected as

529.

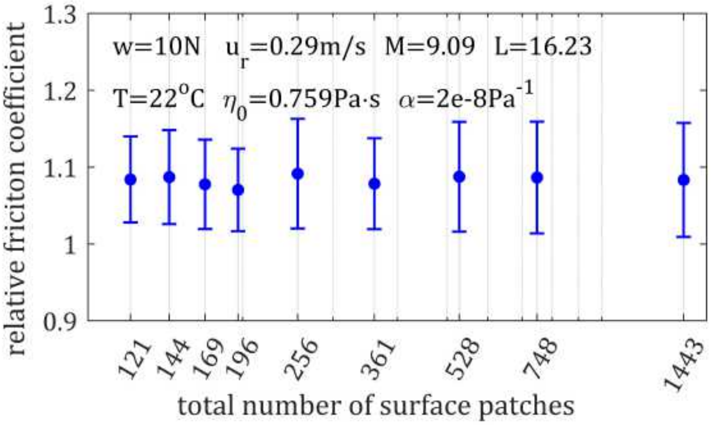

Figure 4.18: Relative friction coefficient as a function of total number of surface patches under the operating condition in Table 4.4.

4.4.2 Operating condition effects

The method to predict friction variations for measured rough surfaces has already described in the previous subsection. In this subsection, effects of operating conditions on friction will be investigated. Except for the rolling speed u_r which is varying, the values of all the other parameters are fixed as shown in Table 4.4. Equation C.1 shows that the pressure fluctuation δp makes a significant contribution to the relative friction coefficient. Equation D.1 shows that the amplitude deformation rr^d of surface roughness is also an important variable. Therefore, it is necessary to investigate δp and rr^d. A surface patch shown extracted from the surface roughness dART in figure 4.19 is extracted from the rough surface dART to study the variations of δp and rr^d when different operating conditions are employed (shown in table 4.5).

Table 4.5: Operating conditions of selected cases.

Cases	u_r (m/s)	M	L	μ_r/μ_s
1	0.010	114.79	6.97	5.21
2	0.046	36.40	10.22	2.02
3	0.100	20.35	12.41	1.54
4	0.154	14.73	13.82	1.38
5	0.195	12.38	16.65	1.31

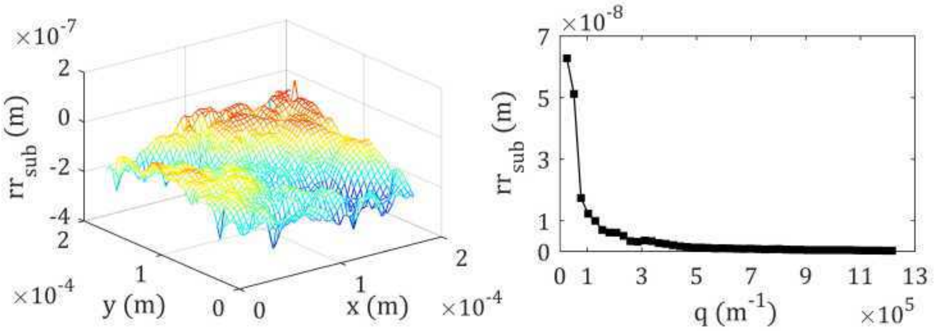

Figure 4.19: A extracted surface patch (left) and its average initial amplitude as a function as q.

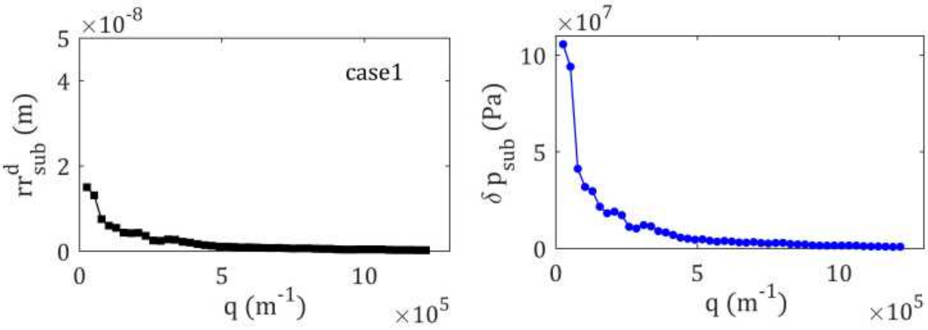

Figure 4.20: The deformed surface patch shown in Figure 4.19 (left) and its pressure variations for case 1.

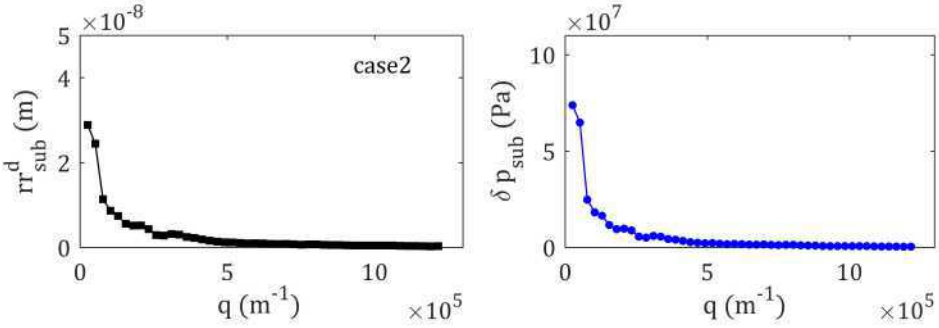

Figure 4.21: The deformed surface patch shown in Figure 4.19 (left) and its pressure variations for case 2.

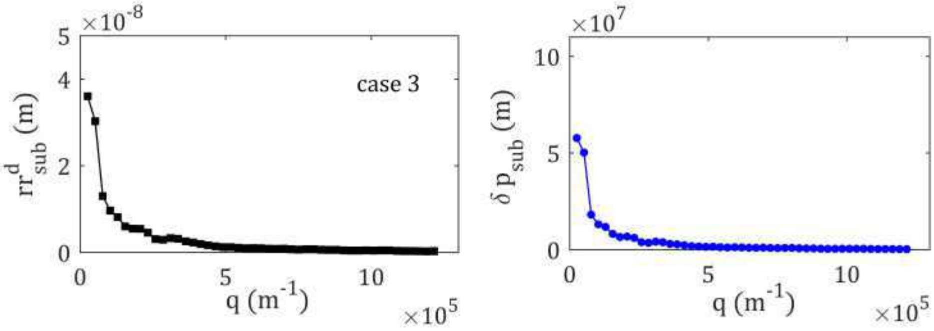

Figure 4.22: The deformed surface patch shown in Figure 4.19 (left) and its pressure variations for case 3.

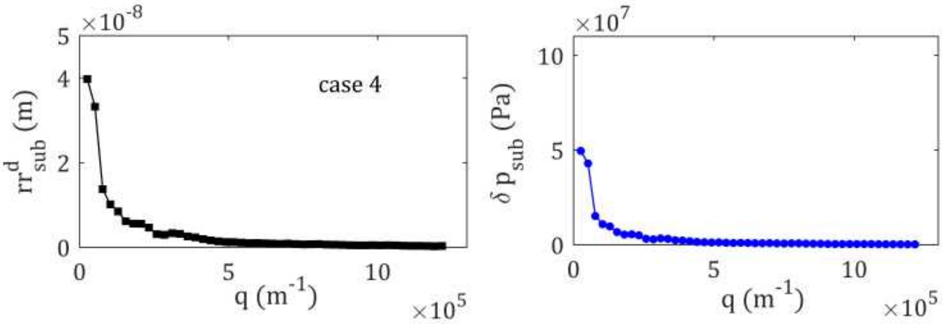

Figure 4.23: The deformed surface patch shown in Figure 4.19 (left) and its pressure variations for case 4.

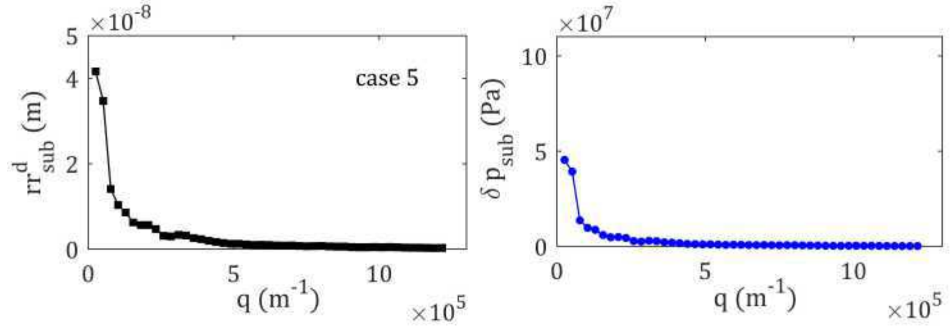

Figure 4.24: The deformed surface patch shown in Figure 4.19 (left) and its pressure variations for case 5.

Figures 4.20-4.24 show the deformed surface patches and their pressure variations as functions of the wave vector q for all the operating conditions in table 4.5. The values at $q = 0$ in these figures are removed, because there are no deformations of sub-surfaces when $q = 0$. According to observation, when the rolling speed u_r increases, the value of the deformed subsurface increases while the value of the pressure increase decreases.

4.4.3 Friction curves for measured surface roughness

Friction variations for two measured surface roughness are plotted in this subsection. For the roughness dART (shown in Figure 4.13), the variations of the Moes load parameter M and material parameter L using geometry and lubricant parameter in Table 4.4 are shown in Figure 4.25.

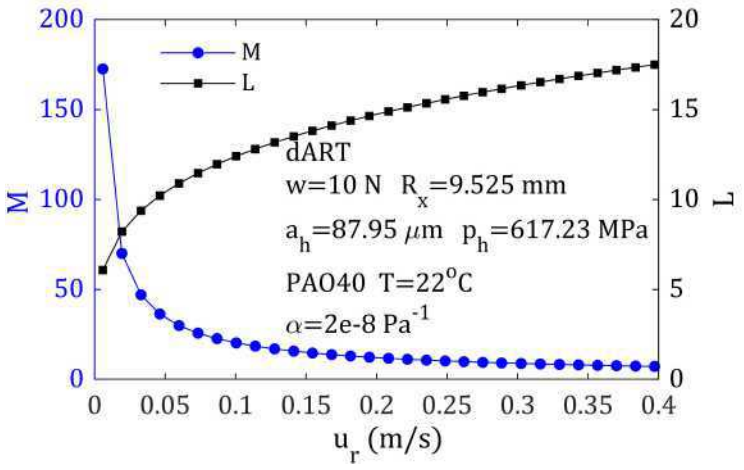

Figure 4.25: Moes parameters M and L as a function of u_r for the roughness dART.

Figure 4.26 shows variations of the relative friction coefficient employing the operating conditions shown in Figure 4.25. It can be observed from this figure that as rolling speed u_r increases, the relative friction coefficient decreases. This decrease trend can also be found in Reference [140] Figure 6.1 (b). According to Hamrock-Dowson central film thickness equation [120], h_c is a function of rolling speed u_r, hence Figure 4.26 can be re-plotted as a function of the "Λ ratio" (shown in Figure 4.27).

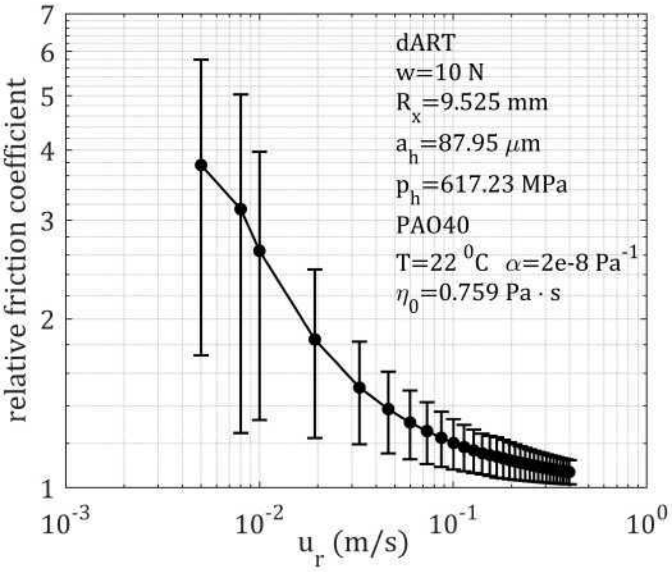

Figure 4.26: The relative friction coefficient as a function of u_r for the roughness dART.

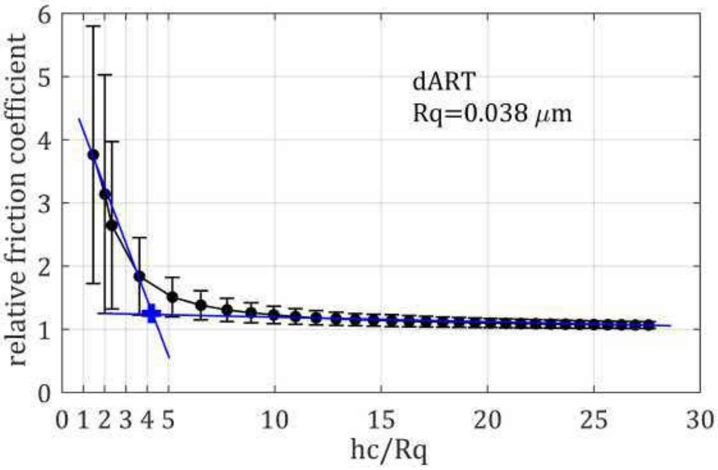

Figure 4.27: The relative friction coefficient as a function of "Λ ratio" for the roughness dART.

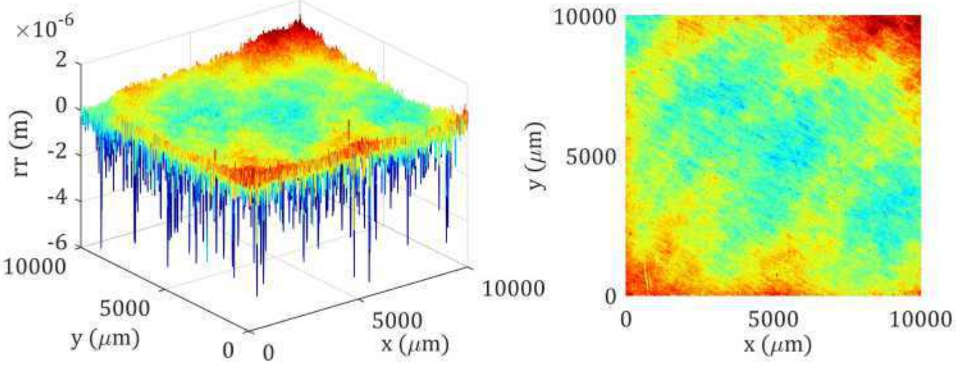

Figure 4.28: Surface roughness dARTEb (left) and the top view of this roughness (right).

Another surface roughness dARTEb (shown in Figure 4.28) is collected from a finished and roughening steel disc, with its root-mean-square $R_q = 0.132\mu$m. The size of this disc is the same as the one for surface roughness dART.

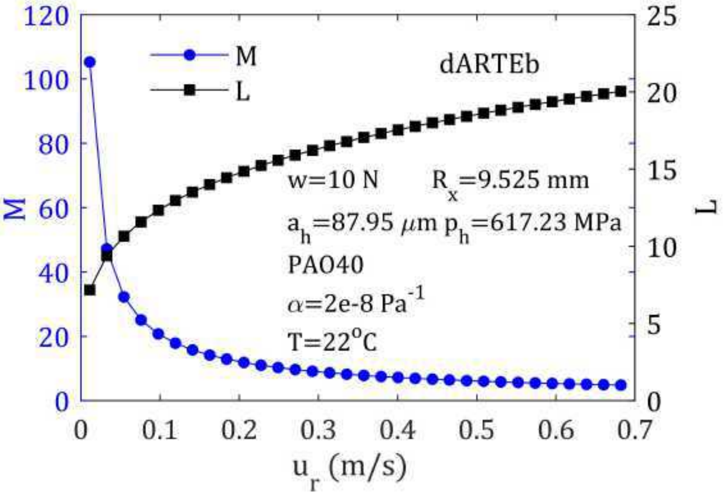

Figure 4.29: Moes parameters M and L as a function of the rolling speed for the surface roughness dARTEb.

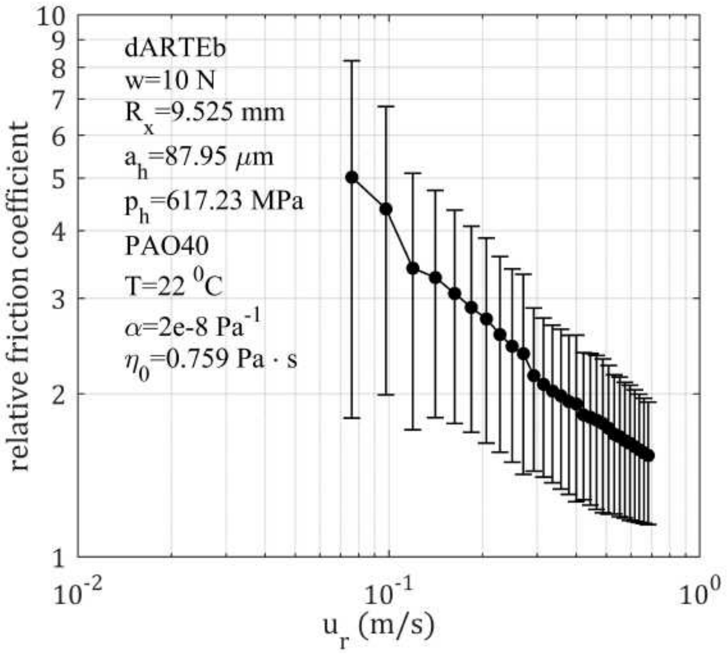

Figure 4.30: The relative friction coefficient as a function of u_r for the surface roughness dARTEb.

For the surface roughness dARTEb, operating conditions can be seen in Figure 4.29. And friction variation curves for this roughness is shown in Figure 4.30 and Figure 4.31. The classical Stribeck curve has a minimum friction point, which is often regarded as the transition point from the mixed lubrication to hydrodynamic lubrication regime. However, for friction curves shown in these two figures, minimum friction points do not occur. Reference [147] defined the transition position as the intersection between two tangent lines to the friction curve (shown as blue crosses in Figure 4.27 and 4.31). For conformal contact, the transition from the mixed lubrication to full-film lubrication regime occurs around $\Lambda = 3.0$. For non-conformal contact cases considered in this subsection, the onset of the "mixed regime" at hc/R_q varying from 4 to 5. At the same time, two different surface roughness show different friction behaviour(shown in Figure 4.32).

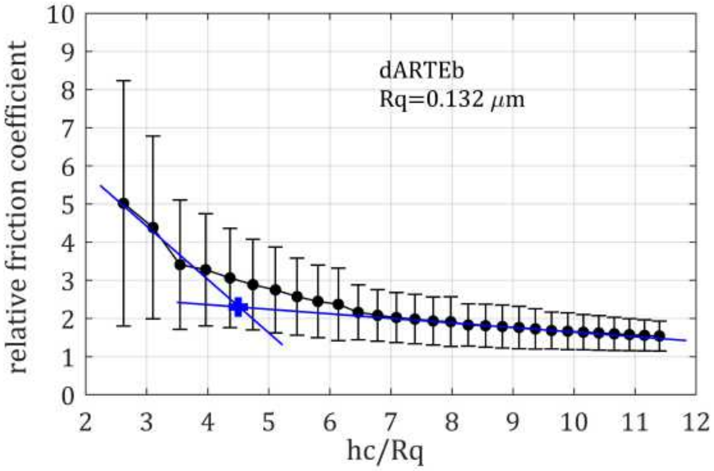

Figure 4.31: The relative friction coefficient as a function of the "Λ ratio" for the surface roughness dARTEb.

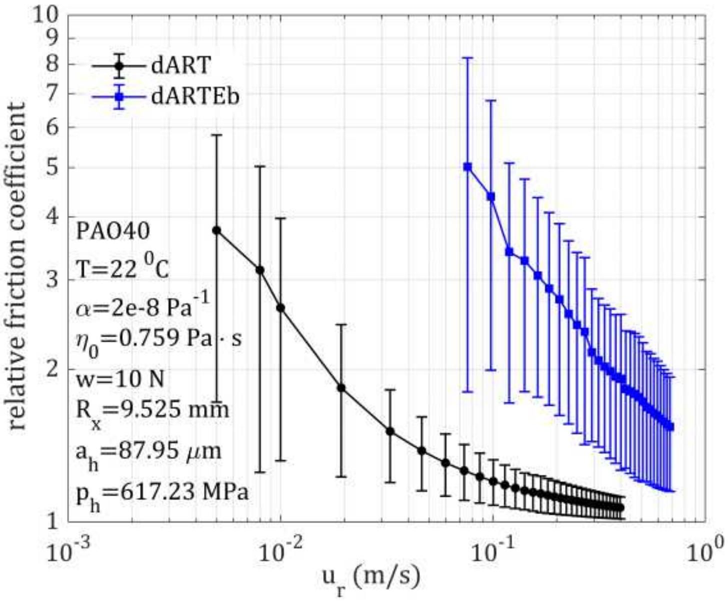

Figure 4.32: The relative friction coefficient as a function of the rolling speed u_r for the surface roughness dART and dARTEb, respectively.

4.5 Conclusion

This chapter proposes a rapid analytical method using the power spectral density to predict friction increase which is due to non-linear viscosity variations from pressure variations caused by surface roughness deformation. This method is validated for an artificial surface roughness by comparing the results with those of a full numerical simulation. A good agreement is found between the full numerical simulation and the PSD prediction. Then the PSD prediction method is also employed to analyse friction variations for a measured surface roughness. Prediction results show that as the "Λ ratio" increases, the friction decreases. The minimum friction point describing the transition from the mixed lubrication to the full-film lubrication regime does not occur for high pressure cases. The same result has also been found in experimental work [140, 147].

Chapter 5

Conclusion and perspectives

Contents

5.1 Conclusion

Proper lubrication and low friction play essential roles in energy conservation. The Stribeck curve is a good tool to describe the friction variation throughout the entire lubrication regime. However, most of the work to obtain this friction curve was related to low pressure condition (conformal contact), and the work was mainly experimental. The motivation for conducting this work is to determine the frictional behaviour under high pressure conditions (non-conformal contact) when the surface roughness is taken into consideration. The main conclusions are listed below:

(i) Current MultiGrid codes show good efficiency to solve lubricated contact problems, but are not sufficiently robust to treat the rough surface problem in a general way. This is because for very rough surfaces, large variations of the coefficient $\rho h^3/\eta$ in Reynolds equation occur on a small scale. Alcouffe et al [66] proposed an efficient way to restore the performance by constructing the coarse grid operator and the intergrid transfers. An new transient EHL code is modified by implementing the coarse grid construction method into the existing EHL MultiGrid code. The new code shows better performance in solving the rough contact problem.

(ii) The Stribeck curve shows that the "Λ ratio" is a suitable parameter to plot friction variation. According to the Amplitude Reduction Theory [53, 58], under very high pressure, the surface roughness will deform and this deformation depends on the operating conditions as well as on the surface roughness parameters. This means that the old "Λ ratio" is not a proper parameter. In this work, using harmonic surface waviness, an elaborate scaling parameter $\theta_2\mathrm{ff}(r)$ including the old "Λ ratio", operating conditions and surface anisotropy parameters is found. Using this new parameters, all simulation results can be unified into a single curve and a curve-fitting equation is obtained.

(iii) A rapid analytical prediction method using the power spectral density is proposed in this work to predict friction increase for a complex surface roughness. This friction increase is due to non-linear viscosity variations from pressure variations caused by surface roughness deformation. This method is validated by the comparison between predictions and full numerical simulations when an artificial surface roughness is employed. Then this rapid prediction method is applied to analyse measured surface roughness.

5.2 Perspectives

The work carried out in this thesis offers a useful tool to detect friction variations under high pressure conditions. However, what we presented in this work is related to Newtonian lubricant, sufficient lubrication and isothermal model. Future work can be suggested as follows:

- In current work, a small slide-to-roll ratio is used to predict friction force and a unique curve is obtained. Larger slide-to-roll ratios should be applied and the theory should be extended.
- The EHL model used in this work is isothermal and Newtonian. Thermal effects and non-Newtonian lubricant can be considered in future study.
- The work studied in this thesis is numerical, more relevant experiments should be conducted to give comparable results.

Appendix A

Construction of the coarse grid operator

The coarse grid operator is:

$$L^H = J_h^H L^h I_H^h \tag{A.1}$$

In order to get the coarse grid operator, orthogonal basis vectors are needed. The first step is to compute $I_H^h \langle e_{iC,jC,k}^H \rangle$:

$$\begin{aligned} I_H^h \langle e_{iC,jC,k}^H \rangle = {} & C_{iF,jF,k}^h e_{iF,jF,k}^h + NW_{iF,jF,k}^h e_{iF-1,jF+1,k}^h + SW_{iF,jF,k}^h e_{iF-1,jF-1,k}^h \\ & + SE_{iF,jF,k}^h e_{iF+1,jF-1,k}^h + NE_{iF,jF,k}^h e_{iF+1,jF+1,k}^h \\ & + N_{iF,jF,k}^h e_{iF,jF+1,k}^h + S_{iF,jF,k}^h e_{iF,jF-1,k}^h \\ & + W_{iF,jF,k}^h e_{iF-1,jF,k}^h + E_{iF,jF,k}^h e_{iF+1,jF,k}^h \end{aligned} \tag{A.2}$$

Then, substituting Equation A.2 in $L^h \langle I_H^h e_{iC,jC,k}^H \rangle$ reads:

$$\begin{aligned} L^h \langle I_H^h e_{iC,jC,k}^H \rangle = L^h [& C_{iF,jF,k}^h e_{iF,jF,k}^h + NW_{iF,jF,k}^h e_{iF-1,jF+1,k}^h + SW_{iF,jF,k}^h e_{iF-1,jF-1,k}^h \\ & + SE_{iF,jF,k}^h e_{iF+1,jF-1,k}^h + NE_{iF,jF,k}^h e_{iF+1,jF+1,k}^h \\ & + N_{iF,jF,k}^h e_{iF,jF+1,k}^h + S_{iF,jF,k}^h e_{iF,jF-1,k}^h \\ & + W_{iF,jF,k}^h e_{iF-1,jF,k}^h + E_{iF,jF,k}^h e_{iF+1,jF,k}^h] \end{aligned} \tag{A.3}$$

in which the influence of L^h need to act on every term, as illustrated in Figure A.1 for 3 terms:

- The influence of L^h on the central point (i, j) (shown as Figure A.1 (a)):

$$\begin{aligned} L^h \langle C_{iF,jF,k}^h e_{iF,jF,k}^h \rangle &= C_{iF,jF,k}^h L^h \langle e_{iF,jF,k}^h \rangle \\ &= C_{iF,jF,k}^h [L_c^h (iF, jF, k) e_{iF,jF,k}^h \\ &+ L_{nw}^h (iF, jF, k) e_{iF-1,jF+1,k}^h + L_{sw}^h (iF, jF, k) e_{iF-1,jF-1,k}^h \\ &+ L_{se}^h (iF, jF, k) e_{iF+1,jF-1,k}^h + L_{ne}^h (iF, jF, k) e_{iF+1,jF+1,k}^h \\ &+ L_n^h (iF, jF, k) e_{iF,jF+1,k}^h + L_w^h (iF, jF, k) e_{iF-1,jF,k}^h \\ &+ L_s^h (iF, jF, k) e_{iF,jF-1,k}^h + L_e^h (iF, jF, k) e_{iF+1,jF,k}^h] \end{aligned}$$

- The influence of L^h on the east point $(i+1, j)$ (shown as Figure A.1 (b)):

$$\begin{aligned} L^h \langle E_{iF,jF,k}^h e_{iF+1,jF,k}^h \rangle &= E_{iF,jF,k}^h L^h \langle e_{iF+1,jF,k}^h \rangle \\ &= E_{iF,jF,k}^h [L_c^h (iF+1, jF, k) e_{iF+1,jF,k}^h \\ &+ L_{nw}^h (iF+1, jF, k) e_{iF,jF+1,k}^h + L_{sw}^h (iF+1, jF, k) e_{iF,jF-1,k}^h \\ &+ L_{se}^h (iF+1, jF, k) e_{iF+2,jF-1,k}^h + L_{ne}^h (iF+1, jF, k) e_{iF+2,jF+1,k}^h \\ &+ L_n^h (iF+1, jF, k) e_{iF+1,jF+1,k}^h + L_w^h (iF+1, jF, k) e_{iF,jF,k}^h \\ &+ L_s^h (iF+1, jF, k) e_{iF+1,jF-1,k}^h + L_e^h (iF+1, jF, k) e_{iF+2,jF,k}^h] \end{aligned}$$

- The influence of L^h on the north-east point $(i+1, j+1)$ (shown as Figure A.1 (c)):

$$\begin{aligned}
L^h\langle NE^h_{iF,jF,k}e^h_{iF+1,jF+1,k}\rangle &= NE^h_{iF,jF,k}L^h\langle e^h_{iF+1,jF+1,k}\rangle \\
&= NE^h_{iF,jF,k}[L^h_c(iF+1,jF+1,k)e^h_{iF+1,jF+1,k} \\
&+ L^h_{nw}(iF+1,jF+1,k)e^h_{iF,jF+2,k} \\
&+ L^h_{sw}(iF+1,jF+1,k)e^h_{iF,jF,k} \\
&+ L^h_{se}(iF+1,jF+1,k)e^h_{iF+2,jF,k} \\
&+ L^h_{ne}(iF+1,jF+1,k)e^h_{iF+2,jF+2,k} \\
&+ L^h_{n}(iF+1,jF+1,k)e^h_{iF+1,jF+2,k} \\
&+ L^h_{w}(iF+1,jF+1,k)e^h_{iF,jF+1,k} \\
&+ L^h_{s}(iF+1,jF+1,k)e^h_{iF+1,jF,k} \\
&+ L^h_{e}(iF+1,jF+1,k)e^h_{iF+2,jF+1,k}]
\end{aligned}$$

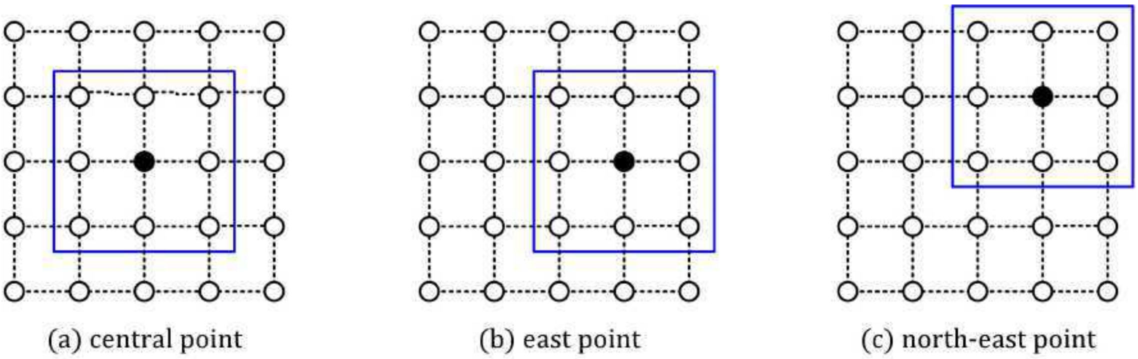
(a) central point
(b) east point
(c) north-east point

Figure A.1: Influences of the coarse grid operator L^h on central point, east point and north-east point.

From the three equations above one observes that the operator L_h influences fifteen points around point (i, j) in total. By that analogy, with respect to nine terms in Equation A.3 twenty five points around point (i, j) are affected by the operator L_h. Coefficients of 25 points around (i, j) is denoted as:

$$\begin{bmatrix}
IC(iF-2,jF+2,k) & IC(iF-1,jF+2,k) & IC(iF,jF+2,k) & IC(iF+1,jF+2,k) & IC(iF+2,jF+2,k) \\
IC(iF-2,jF+1,k) & IC(iF-1,jF+1,k) & IC(iF,jF+1,k) & IC(iF+1,jF+1,k) & IC(iF+2,jF+1,k) \\
IC(iF-2,jF,k) & IC(iF-1,jF,k) & IC(iF,jF,k) & IC(iF+1,jF,k) & IC(iF+2,jF,k) \\
IC(iF-2,jF-1,k) & IC(iF-1,jF-1,k) & IC(iF,jF-1,k) & IC(iF+1,jF-1,k) & IC(iF+2,jF-1,k) \\
IC(iF-2,jF-2,k) & IC(iF-1,jF-2,k) & IC(iF,jF-2,k) & IC(iF+1,jF-2,k) & IC(iF+2,jF-2,k)
\end{bmatrix} \quad \text{(A.4)}$$

where:

$$IC(iF-2,jF+2,k) = NW^h_{iF,jF,k}L^h_{nw}(iF-1,jF+1,k)$$

$$IC(iF-2,jF+1,k) = NW^h_{iF,jF,k}L^h_w(iF-1,jF+1,k)$$

$$\begin{aligned} IC(iF-2,jF,k) = {} & NW^h_{iF,jF,k}L^h_{sw}(iF-1,jF+1,k) \\ & + SW^h_{iF,jF,k}L^h_{nw}(iF-1,jF-1,k) + W^h_{iF,jF,k}L^h_{sw}(iF-1,jF,k) \end{aligned}$$

$$IC(iF-2,jF-1,k) = SW^h_{iF,jF,k}L^h_w(iF-1,jF-1,k) + W^h_{iF,jF,k}L^h_{sw}(iF-1,jF,k)$$

$$IC(iF-2,jF-2,k) = SW^h_{iF,jF,k}L^h_{sw}(iF-1,jF-1,k)$$

$$IC(iF-1,jF+2,k) = NW^h_{iF,jF,k}L^h_n(iF-1,jF+1,k) + N^h_{iF,jF,k}L^h_{nw}(iF,jF+1,k)$$

$$\begin{aligned} IC(iF-1,jF+1,k) = {} & C^h_{iF,jF,k}L^h_{nw}(iF,jF,k) + NW^h_{iF,jF,k}L^h_c(iF-1,jF+1,k) \\ & + N^h_{iF,jF,k}L^h_w(iF,jF+1,k) + W^h_{iF,jF,k}L^h_n(iF-1,jF,k) \end{aligned}$$

$$\begin{aligned} IC(iF-1,jF,k) = {} & C^h_{iF,jF,k}L^h_w(iF,jF,k) + NW^h_{iF,jF,k}L^h_s(iF-1,jF+1,k) \\ & + SW^h_{iF,jF,k}L^h_n(iF-1,jF-1,k) + N^h_{iF,jF,k}L^h_{sw}(iF,jF+1,k) \\ & + S^h_{iF,jF,k}L^h_{nw}(iF,jF-1,k) + W^h_{iF,jF,k}L^h_c(iF-1,jF,k) \end{aligned}$$

$$\begin{aligned} IC(iF-1,jF-1,k) = {} & C^h_{iF,jF,k}L^h_{sw}(iF,jF,k) + SW^h_{iF,jF,k}L^h_c(iF-1,jF-1,k) \\ & + S^h_{iF,jF,k}L^h_w(iF,jF-1,k) + W^h_{iF,jF,k}L^h_s(iF-1,jF,k) \end{aligned}$$

$$IC(iF-1,jF-2,k) = SW^h_{iF,jF,k}L^h_s(iF-1,jF-1,k) + S^h_{iF,jF,k}L^h_{sw}(iF,jF-1,k)$$

$$\begin{aligned} IC(iF,jF+2,k) = {} & NW^h_{iF,jF,k}L^h_{ne}(iF-1,jF+1,k) + NE^h_{iF,jF,k}L^h_w(iF,jF-1,k) \\ & + N^h_{iF,jF,k}L^h_n(iF,jF+1,k) \end{aligned}$$

$$\begin{aligned} IC(iF,jF+1,k) = {} & C^h_{iF,jF,k}L^h_n(iF,jF,k) + NW^h_{iF,jF,k}L^h_e(iF-1,jF+1,k) \\ & + NE^h_{iF,jF,k}L^h_w(iF+1,jF+1,k) + N^h_{iF,jF,k}L^h_c(iF,jF+1,k) \\ & + W^h_{iF,jF,k}L^h_{ne}(iF-1,jF,k) + E^h_{iF,jF,k}L^h_{nw}(iF+1,jF,k) \end{aligned}$$

$$\begin{aligned} IC(iF,jF,k) = {} & C^h_{iF,jF,k}L^h_c(iF,jF,k) + NW^h_{iF,jF,k}L^h_{se}(iF-1,jF+1,k) \\ & + SW^h_{iF,jF,k}L^h_{ne}(iF-1,jF-1,k) \\ & + SE^h_{iF,jF,k}L^h_{nw}(iF+1,jF-1,k) + NE^h_{iF,jF,k}L^h_{sw}(iF+1,jF+1,k) \\ & + N^h_{iF,jF,k}L^h_s(iF,jF+1,k) + S^h_{iF,jF,k}L^h_n(iF,jF-1,k) \\ & + W^h_{iF,jF,k}L^h_e(iF-1,jF,k) + E^h_{iF,jF,k}L^h_w(iF+1,jF,k) \end{aligned}$$

The last step is to compute $J_h^H\langle L^h I_H^h e_{iC,jC,k}^H\rangle$. The way to extend the restriction coefficients on 25 points in Equation A.4 is the same as that of computing $L^h\langle I_H^h e_{iC,jC,k}^H\rangle$. There is no need to do a restriction for 25 points. As was shown in Figure A.2, besides coincidental points (blue points) themselves, 3 points contribute to each corner point (shown as Figure A.2 (a)), 5 points influence each middle point (shown as Figure A.2 (b)) and 8 points impact on central point (shown as Figure A.2 (c)).

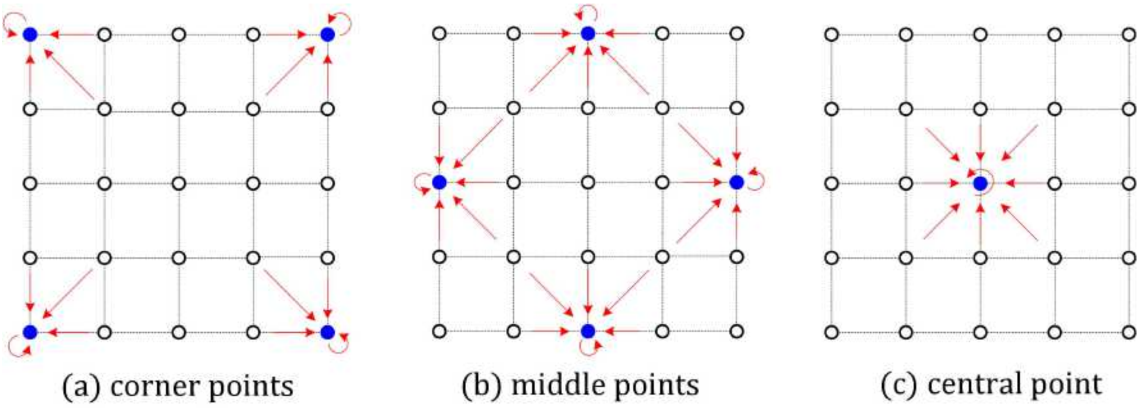
(a) corner points
(b) middle points
(c) central point

Figure A.2: Influences of the injection operator J_h^H on nine coincidental points (blue points).

Hence, the coarse grid operator whose stencil is:

$$L^H = \begin{bmatrix} L_{nw}^H(iC,jC,k) & L_n^H(iC,jC,k) & L_{ne}^H(iC,jC,k) \\ L_w^H(iC,jC,k) & L_c^H(iC,jC,k) & L_e^H(iC,jC,k) \\ L_{sw}^H(iC,jC,k) & L_s^H(iC,jC,k) & L_{se}^H(ic,jC,k) \end{bmatrix} \tag{A.5}$$

in which:

$$\begin{aligned} L_{nw}^H(iC,jC,k) = {} & IC(iF-2,jF+2,k)c_{iF-2,jF+2,k}^h + IC(iF-1,jF+2,k)w_{iF-1,jF+2,k}^h \\ & + IC(iF-2,jF+1,k)n_{iF-2,jF+1,k}^h + IC(iF-1,jF+1,k)nw_{iF-1,jF+1,k}^h \end{aligned}$$

$$\begin{aligned} L_{sw}^H(iC,jC,k) = {} & IC(iF-2,jF-2,k)c_{iF-2,jF-2,k}^h + IC(iF-2,jF-1,k)s_{iF-2,jF-1,k}^h \\ & + IC(iF-1,jF-2,k)w_{iF-1,jF-2,k}^h + IC(iF-1,jF-1,k)sw_{iF-1,jF-1,k}^h \end{aligned}$$

$$\begin{aligned} L_{se}^H(iC,jC,k) = {} & IC(iF+2,jF-2,k)c_{iF+2,jF-2,k}^h + IC(iF+1,jF-2,k)e_{iF+1,jF-2,k}^h \\ & + IC(iF+2,jF-1,k)s_{iF+2,jF-1,k}^h + IC(iF+1,jF-1,k)se_{iF+1,jF-1,k}^h \end{aligned}$$

$$\begin{aligned} L_{ne}^H(iC,jC,k) = {} & IC(iF+2,jF+2,k)c_{iF+2,jF+2,k}^h + IC(iF+1,jF+2,k)e_{iF+1,jF+2,k}^h \\ & + IC(iF+2,jF+1,k)n_{iF+2,jF+1,k}^h + IC(iF+1,jF+1,k)ne_{iF+1,jF+1,k}^h \end{aligned}$$

$$\begin{aligned}L_n^H(iC,jC,k) = {} & IC(iF,jF+2,k)c^h_{iF,jF+2,k} + IC(iF-1,jF+2,k)e^h_{iF-1,jF+2,k}\\ & + IC(iF+1,jF+2,k)w^h_{iF+1,jF+2,k} + IC(iF,jF+1,k)n^h_{iF,jF+1,k}\\ & + IC(iF-1,jF+1,k)ne^h_{iF-1,jF+1,k} + IC(iF+1,jF+1,k)nw^h_{iF+1,jF+1,k}\end{aligned}$$

$$\begin{aligned}L_s^H(iC,jC,k) = {} & IC(iF,jF-2,k)c^h_{iF,jF-2,k} + IC(iF-1,jF-2,k)e^h_{iF-1,jF-2,k}\\ & + IC(iF+1,jF-2,k)w^h_{iF+1,jF-2,k} + IC(iF,jF-1,k)s^h_{iF,jF-1,k}\\ & + IC(iF-1,jF-1,k)se^h_{iF-1,jF-1,k} + IC(iF+1,jF-1,k)sw^h_{iF+1,jF-1,k}\end{aligned}$$

$$\begin{aligned}L_w^H(iC,jC,k) = {} & IC(iF-2,jF,k)c^h_{iF-2,jF,k} + IC(iF-2,jF+1,k)s^h_{iF-2,jF+1,k}\\ & + IC(iF-2,jF-1,k)n^h_{iF-2,jF-1,k} + IC(iF-1,jF,k)w^h_{iF-1,jF,k}\\ & + IC(iF-1,jF+1,k)sw^h_{iF-1,jF+1,k} + IC(iF-1,jF-1,k)nw^h_{iF-1,jF-1,k}\end{aligned}$$

$$\begin{aligned}L_e^H(iC,jC,k) = {} & IC(iF+2,jF,k)c^h_{iF+2,jF,k} + IC(iF+2,jF+1,k)s^h_{iF+2,jF+1,k}\\ & + IC(iF+2,jF-1,k)n^h_{iF+2,jF-1,k} + IC(iF+1,jF,k)e^h_{iF+1,jF,k}\\ & + IC(iF+1,jF+1,k)se^h_{iF+1,jF+1,k} + IC(iF+1,jF-1,k)ne^h_{iF+1,jF-1,k}\end{aligned}$$

$$\begin{aligned}L_c^H(iC,jC,k) = {} & IC(iF,jF,k)c^h_{iF,jF,k} + IC(iF,jF+1,k)s^h_{iF,jF+1,k} + IC(iF,jF-1,k)n^h_{iF,jF-1,k}\\ & + IC(iF-1,jF,k)e^h_{iF-1,jF,k} + IC(iF+1,jF,k)w^h_{iF+1,jF,k}\\ & + IC(iF-1,jF+1,k)se^h_{iF-1,jF+1,k} + IC(iF-1,jF-1,k)ne^h_{iF-1,jF-1,k}\\ & + IC(iF+1,jF-1,k)nw^h_{iF+1,jF-1,k} + IC(iF+1,jF+1,k)sw^h_{iF+1,jF+1,k}\end{aligned}$$

Appendix B

Derivation of matrix A^j for line relaxation

According to the discrete Reynolds equation in Chapter 2, the dynamic residual $r^l_{i,j,k}$ is defined as:

$$\begin{aligned} r^l_{i,j,k} = pf^l_{i,j,k} - (& L^l_c P^l_{i,j,k} + L^l_n P^l_{i,j+1,k} + L^l_w P^l_{i-1,j,k} + L^l_s P^l_{i,j-1,k} + L^l_e P^l_{i+1,j,k} \\ & + L^l_{nw} P^l_{i-1,j+1,k} + L^l_{sw} P^l_{i-1,j-1,k} + L^l_{se} P^l_{i+1,j-1,k} + L^l_{ne} P^l_{i+1,j+1,k}) \\ & + h^l (1.5\bar{\rho}^l_{i,j,k} H^l_{i,j,k} - 2.0\bar{\rho}^l_{i-1,j,k} H^l_{i-1,j,k} + 0.5\bar{\rho}^l_{i-2,j,k} H^l_{i-2,j,k}) \\ & + \frac{(h^l)^2}{ht}(1.5\bar{\rho}_{i,j,k} H_{i,j,k}) \end{aligned} \tag{B.1}$$

and the *left hand side equation* is:

$$\begin{aligned} L^l_{i,j,k}\langle \underline{P}^l \rangle = (& L^l_c P^l_{i,j,k} + L^l_n P^l_{i,j+1,k} + L^l_w P^l_{i-1,j,k} + L^l_s P^l_{i,j-1,k} + L^l_e P^l_{i+1,j,k} \\ & + L^l_{nw} P^l_{i-1,j+1,k} + L^l_{sw} P^l_{i-1,j-1,k} + L^l_{se} P^l_{i+1,j-1,k} + L^l_{ne} P^l_{i+1,j+1,k}) \\ & - h^l (1.5\bar{\rho}^l_{i,j,k} H^l_{i,j,k} - 2.0\bar{\rho}^l_{i-1,j,k} H^l_{i-1,j,k} + 0.5\bar{\rho}^l_{i-2,j,k} H^l_{i-2,j,k}) \\ & - \frac{(h^l)^2}{ht}(1.5\bar{\rho}_{i,j,k} H_{i,j,k}). \end{aligned} \tag{B.2}$$

Reference [10] recommend that the switch parameter $\xi^l_{\text{limit}} = 0.3$ is a good choice to have an efficient smooth performance.

B.0.1 Gauss-Seidel line relaxation

When the *local* coefficient ξ^l satisfies the below condition, the Gauss-Seidel line relaxation is applied.

$$\frac{\xi^l_{i\pm1/2,j,k}}{(h^l)^2} > \xi^l_{\text{limit}} \quad \text{and} \quad \frac{\xi^l_{i,j\pm1/2,k}}{(h^l)^2} > \xi^l_{\text{limit}}. \tag{B.3}$$

Then the matrix $A^j_{i,m}$ is given by:

$$A^j_{i,m} = \left(\frac{\partial L^l_{i,j,k}\langle \underline{P}^l \rangle}{\partial P^l_{m,j,k}}\right)_{\underline{P}^h = \underline{\tilde{P}}^h} \tag{B.4}$$

for $0 < m < n_x$ and $0 < i < n_x$.

The matrix $A^j_{i,m}$ have different expressions for different conditions:

- if $|i-m| > 1$:

$$\begin{aligned} A^j_{i,m} = & - h^l (1.5\bar{\rho}^l_{i,j,k} K^{ll}_{|i-m|,0} - 2.0\bar{\rho}^l_{i-1,j,k} K^{ll}_{|i-m-1|,0} + 0.5\bar{\rho}^l_{i-2,j,k} K^{ll}_{|i-m-2|,0}) \\ & - \frac{(h^l)^2}{ht}(1.5\bar{\rho}_{i,j,k} K^{ll}_{|i-m|,0}) \end{aligned} \tag{B.5}$$

- if $i = m$:

$$\begin{aligned} A^j_{i,i} = L^l_c & - h^l (1.5\bar{\rho}^l_{i,j,k} K^{ll}_{0,0} - 2.0\bar{\rho}^l_{i-1,j,k} K^{ll}_{1,0} + 0.5\bar{\rho}^l_{i-2,j,k} K^{ll}_{2,0}) \\ & - \frac{(h^l)^2}{ht}(1.5\bar{\rho}_{i,j,k} K^{ll}_{0,0}) \end{aligned} \tag{B.6}$$

- if $i > 1$:

$$\begin{aligned} A^j_{i,i-1} = L^l_w - h^l(1.5\bar{\rho}^l_{i,j,k}K^{ll}_{1,0} - 2.0\bar{\rho}^l_{i-1,j,k}K^{ll}_{0,0} + 0.5\bar{\rho}^l_{i-2,j,k}K^{ll}_{1,0}) \\ - \frac{(h^l)^2}{ht}(1.5\bar{\rho}_{i,j,k}K^{ll}_{1,0}) \end{aligned} \tag{B.7}$$

- if $i < n_x - 1$:

$$\begin{aligned} A^j_{i,i+1} = L^l_e - h^l(1.5\bar{\rho}^l_{i,j,k}K^{ll}_{1,0} - 2.0\bar{\rho}^l_{i-1,j,k}K^{ll}_{2,0} + 0.5\bar{\rho}^l_{i-2,j,k}K^{ll}_{3,0}) \\ - \frac{(h^l)^2}{ht}(1.5\bar{\rho}_{i,j,k}K^{ll}_{1,0}). \end{aligned} \tag{B.8}$$

B.0.2 Jacobi distributive line relaxation

When the *local* coefficient ξ^l can not satisfy the condition Equation B.3, the Jacobi distributive line relaxation is used.

Subsequently, the matrix $A^j_{i,m}$ is:

$$A^j_{i,m} = [\frac{\partial L^l_{i,j,k}\langle \underline{P}^l \rangle}{\partial P^l_{m,j,k}} - \frac{1}{4}(\frac{\partial L^l_{i,j,k}\langle \underline{P}^l \rangle}{\partial P^l_{m+1,j,k}} + \frac{\partial L^l_{i,j,k}\langle \underline{P}^l \rangle}{\partial P^l_{m-1,j,k}} + \frac{\partial L^l_{i,j,k}\langle \underline{P}^l \rangle}{\partial P^l_{m,j+1,k}} + \frac{\partial L^l_{i,j,k}\langle \underline{P}^l \rangle}{\partial P^l_{m,j-1,k}})]_{\underline{P}^h = \underline{\bar{P}}^h} \tag{B.9}$$

for $0 < m < n_x$ and $0 < i < n_x$. For convenience, introducing a parameter $\Delta K_{m,j}$ to simply the expression of $A^j_{i,m}$:

$$\Delta K^{ll}_{m,n} = K^{ll}_{m,n} - \frac{1}{4}(K^{ll}_{m-1,n} + K^{ll}_{m+1,n} + K^{ll}_{m,n+1} + K^{ll}_{m,n-1}). \tag{B.10}$$

For different i values, the matrix of $A^j_{i,m}$ are represented as:

- for $|i-m| > 2$:

$$\begin{aligned} A^j_{i,m} = -h^l(1.5\bar{\rho}^l_{i,j,k}\Delta K^{ll}_{|i-m|,0} - 2.0\bar{\rho}^l_{i-1,j,k}\Delta K^{ll}_{|i-m-1|,0} + 0.5\bar{\rho}^l_{i-2,j,k}\Delta K^{ll}_{|i-m-2|,0}) \\ - \frac{(h^l)^2}{ht}(1.5\bar{\rho}_{i,j,k}\Delta K^{ll}_{|i-m|,0}) \end{aligned} \tag{B.11}$$

- for $i = m$:

$$\begin{aligned} A^j_{i,i} = L^l_c - \frac{1}{4}(L^l_e + L^l_w + L^l_n + L^l_s) \\ - h^l(1.5\bar{\rho}^l_{i,j,k}\Delta K^{ll}_{0,0} - 2.0\bar{\rho}^l_{i-1,j,k}\Delta K^{ll}_{1,0} + 0.5\bar{\rho}^l_{i-2,j,k}\Delta K^{ll}_{2,0}) \\ - \frac{(h^l)^2}{ht}(1.5\bar{\rho}_{i,j,k}\Delta K^{ll}_{0,0}) \end{aligned} \tag{B.12}$$

- for $i > 2$:

$$\begin{aligned} A^j_{i,i-2} = -\frac{1}{4}L^l_w - h^l(1.5\bar{\rho}^l_{i,j,k}\Delta K^{ll}_{2,0} - 2.0\bar{\rho}^l_{i-1,j,k}\Delta K^{ll}_{1,0} + 0.5\bar{\rho}^l_{i-2,j,k}\Delta K^{ll}_{0,0}) \\ - \frac{(h^l)^2}{ht}(1.5\bar{\rho}_{i,j,k}\Delta K^{ll}_{2,0}) \end{aligned} \tag{B.13}$$

- for $i > 1$:

$$\begin{aligned} A^j_{i,i-1} = L^l_w - \frac{1}{4}(L^l_c + L^l_n w + L^l_s w) \\ - h^l(1.5\bar{\rho}^l_{i,j,k}\Delta K^{ll}_{1,0} - 2.0\bar{\rho}^l_{i-1,j,k}\Delta K^{ll}_{0,0} + 0.5\bar{\rho}^l_{i-2,j,k}\Delta K^{ll}_{1,0}) \\ - \frac{(h^l)^2}{ht}(1.5\bar{\rho}_{i,j,k}\Delta K^{ll}_{1,0}) \end{aligned} \tag{B.14}$$

- for $i < n_x - 1$:

$$\begin{aligned} A^{j}_{i,i+1} = L^{l}_{e} - \frac{1}{4}(L^{l}_{c} + L^{l}_{n}e + L^{l}_{s}e) \\ - h^{l}(1.5\bar{\rho}^{l}_{i,j,k}\Delta K^{ll}_{1,0} - 2.0\bar{\rho}^{l}_{i-1,j,k}\Delta K^{ll}_{2,0} + 0.5\bar{\rho}^{l}_{i-2,j,k}\Delta K^{ll}_{3,0}) \\ - \frac{(h^{l})^{2}}{ht}(1.5\bar{\rho}_{i,j,k}\Delta K^{ll}_{1,0}) \end{aligned} \tag{B.15}$$

- for $i < n_x - 2$:

$$\begin{aligned} A^{j}_{i,i+2} = -\frac{1}{4}L^{l}_{e} - h^{l}(1.5\bar{\rho}^{l}_{i,j,k}\Delta K^{ll}_{2,0} - 2.0\bar{\rho}^{l}_{i-1,j,k}\Delta K^{ll}_{3,0} + 0.5\bar{\rho}^{l}_{i-2,j,k}\Delta K^{ll}_{4,0}) \\ - \frac{(h^{l})^{2}}{ht}(1.5\bar{\rho}_{i,j,k}\Delta K^{ll}_{2,0}). \end{aligned} \tag{B.16}$$

Appendix C

Derivation of the scaling parameter θ_2

According to the Barus [115] viscosity-pressure equation, the shear stress ratio can be approximated as:

$$\frac{\tau_r}{\tau_s} \approx e^{\bar{\alpha}\cdot\Delta P} = 1 + \bar{\alpha}\cdot\Delta P + \frac{(\bar{\alpha}\cdot\Delta P)^2}{2!} + \frac{(\bar{\alpha}\cdot\Delta P)^3}{3!} + \frac{(\bar{\alpha}\cdot\Delta P)^4}{4!} + ... \tag{C.1}$$

where the pressure increase ΔP is the following function of the deformation [117], i.e.:

$$\Delta P = \frac{\pi^2 Ai}{2\lambda/a_h}(1 - \frac{Ad}{Ai}).$$

Using a first order approximation of the dimensionless pressure increase ΔP, $\bar{\alpha}\cdot\Delta P$ reduces to:

$$\bar{\alpha}\cdot\Delta P \approx \bar{\alpha}\frac{\pi^2 Ai}{2\lambda/a_h} \approx [\frac{L}{\pi}(\frac{3M}{2})^{1/3}]\frac{\pi^2 Hc}{2\lambda/a_h}(\frac{Hc}{Ai})^{-1} \tag{C.2}$$

where $\bar{\alpha}$ is expressed as $\bar{\alpha} = (L/\pi)(3M/2)^{1/3}$. Defining H_c^D the dimensionless film thickness film thickness value using the well-known Hamrock-Dowson Equation [120], $H_c^D = 1.69G^{0.53}U^{0.67}W_2^{-0.067}(1-0.61\exp(-0.73k))$ with $k = 1.03$ for circle contact (i.e. $H_c^D = 1.2L^{0.53}U^{0.49}M^{-0.067}$). Now the dimensionless central film thickness H_c can be rewritten as:

$$Hc = \frac{R_x^2}{a_h^2}\cdot H_c^D \tag{C.3}$$

in which R_x^2/a_h^2 is expressed as $R_x^2/a_h^2 = (3/2)^{-2/3}M^{-2/3}U^{-1/2}$. Substituting Equation C.3 into Equation C.2 gives:

$$\bar{\alpha}\cdot\Delta P \approx 1.6467[L^{-1.03}M^{-0.4}(\lambda/a_h)^1(Hc/Ai)]^{-1}. \tag{C.4}$$

Applying a second order approximation of ΔP, $\bar{\alpha}\Delta P$ yields:

$$\bar{\alpha}\cdot\Delta P \approx \frac{\pi^2 Ai}{2\lambda/a_h}(1 - \frac{Ad}{Ai}) \approx 0.24[L^{-1.03}M^{-0.1}(\lambda/a_h)^0(Hc/Ai)]^{-1} \tag{C.5}$$

where $Ad/Ai \approx 1 - 0.15\nabla_2 \approx 1 - 0.15(\lambda/a_h)(M/L)^{0.5}$.

Observing Equation C.4 and Equation C.5, the exponent for the parameter M, L and λ/a_h are summarized in Table C.1. Hence the expression of the θ_2 parameter using $M^{0.33}$, $L^{-1.1}$ and $(\lambda/a_h)^{0.67}$ obtained by curve-fitting, has coefficients that fall in the range outlined above.

Table C.1: Range of the exponent for each parameter.

Parameter	Range
M	$-0.10 \sim 0.40$
L	$-1.03 \sim -1.53$
λ/a_h	$0 \sim 1$
Hc/Ai	1

Appendix D

The relation between the elastic deformation and corresponding pressure for 2D wavy surfaces

Reference [117] gives the relation between the elastic deformation and pressure for 1D wavy surfaces is:

$$\delta p = \frac{\pi E' \Delta}{\lambda} \tag{D.1}$$

and for 2D wavy surfaces, which consists of two separate components:

$$\delta p = \frac{\pi E' \Delta_x}{\lambda_x} + \frac{\pi E' \Delta_y}{\lambda_y}. \tag{D.2}$$

For the surface waviness expressed as Eq.3.1, there is no explicit equation to describe this relation. Hence, it is necessary to give such relation. Assuming a pressure distribution:

$$p(x,y) = A_i^p \cos(\frac{2\pi x}{\lambda_x}) \cos(\frac{2\pi y}{\lambda_y}) \tag{D.3}$$

with $x \in [-4,4]$ and $y \in [-4,4]$. Where A_i^p is the initial amplitude of the pressure distribution. The equation to compute the corresponding elastic deformation is:

$$D(x,y) = \frac{2}{\pi E'} \iint \frac{p(x',y')}{\sqrt{(x-x')^2 + (y-y')^2}} dx' dy'. \tag{D.4}$$

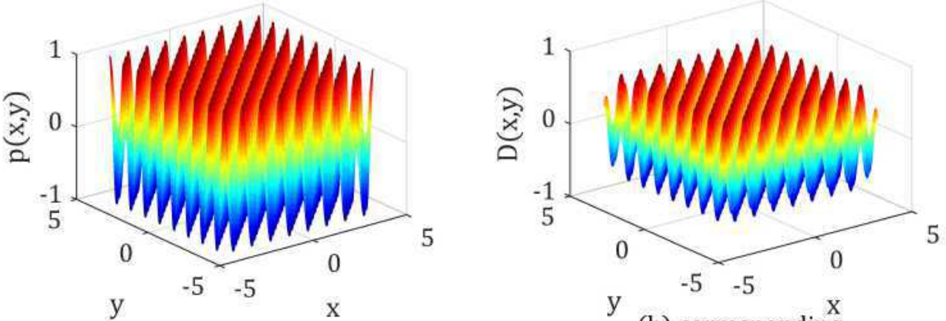

(a) pressure distribution

(b) corresponding deformation distribution

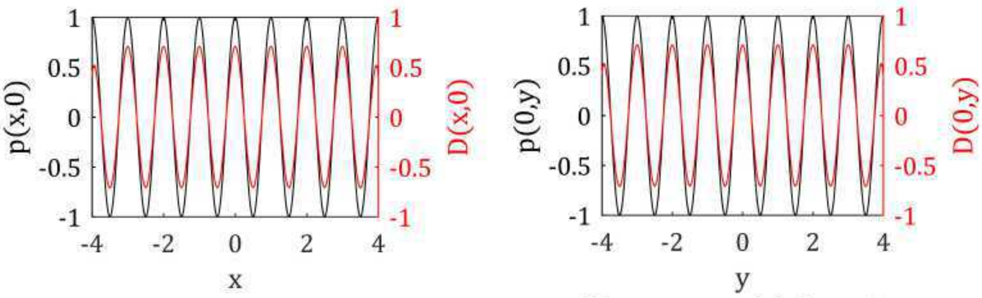

(c) pressure and deformation distributions along x direction

(d) pressure and deformation distributions along y direction

Figure D.1: Pressure distribution and the corresponding elastic deformation.

Figure D.1 shows that the elastic deformation due to the pressure shown as Figure D.1 (a) has the same harmonic waviness. Thus the elastic deformation Equation D.4 can be re-written as:

$$D(x,y) = A_d^D \cos(\frac{2\pi x}{\lambda_x})\cos(\frac{2\pi y}{\lambda_y}) \tag{D.5}$$

in which A_d^D is the amplitude of the elastic deformation.

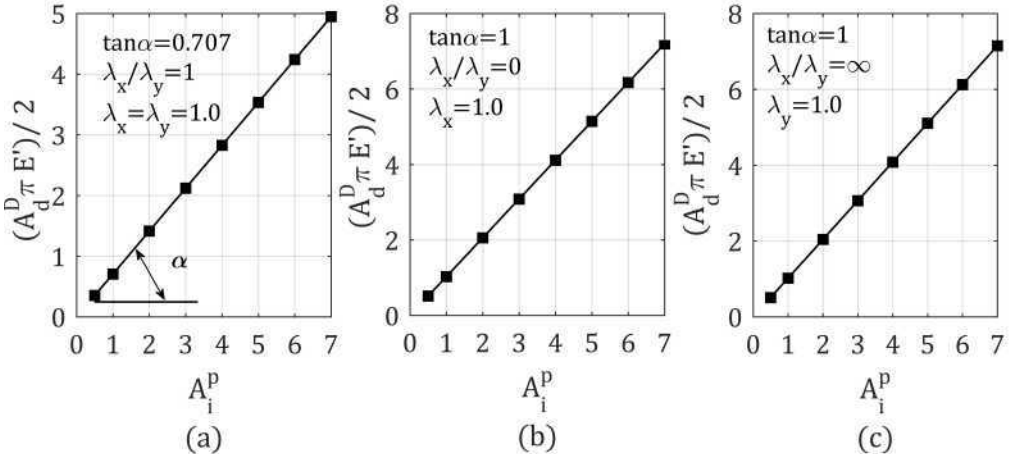

Figure D.2: Amplitude of the elastic deformation A_d^D as a function of initial pressure amplitude A_i^p for the following cases: (a) isotropic, (b) purely transverse, (c) purely longitudinal.

Figure D.2 shows the relation between the amplitude of the elastic deformation A_d^D and the initial pressure amplitude A_i^p for three r values. From this figure, it is can be found that the deformation amplitude A_d^D is proportional to the initial pressure amplitude A_i^p:

$$A_d^D \pi E' \propto A_i^p. \tag{D.6}$$

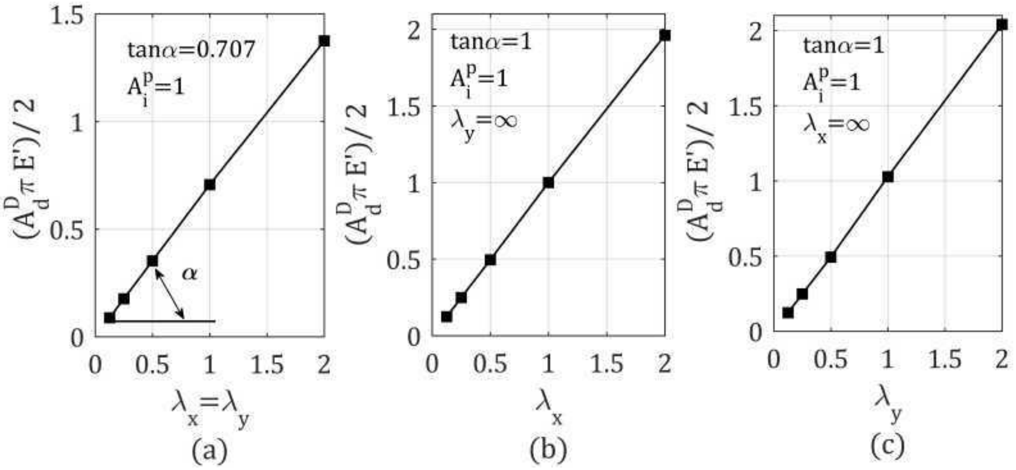

Figure D.3: Amplitude of the elastic deformation A_d^D as a function of wavelength λ ($\lambda = \min(\lambda_x, \lambda_y)$) for the following cases: (a) isotropic, (b) purely transverse, (c) purely longitudinal.

Figure D.3 shows the relation between the amplitude of the elastic deformation A_d^D and the wavelength λ for three r values. From this figure, it is can be found that the deformation amplitude A_d^D is proportional to the the wavelength λ:

$$A_d^D \pi E' \propto \lambda. \tag{D.7}$$

Figure D.4 shows the relation between the amplitude of the elastic deformation A_d^D and the anisotropy parameter r. From this figure, it is can be found that the deformation amplitude A_d^D is proportional to a curve-fitting function $k(r)$:

$$A_d^D \pi E' \propto k(r) \tag{D.8}$$

where

$$k(r) = \begin{cases} -0.3r^{1.7} + 1.0, & \text{if } 0 \leqslant r \leqslant 1 \\ -0.3r^{-1.7} + 1.0, & r > 1 \end{cases} \tag{D.9}$$

with $r = \lambda_x / \lambda_y$.

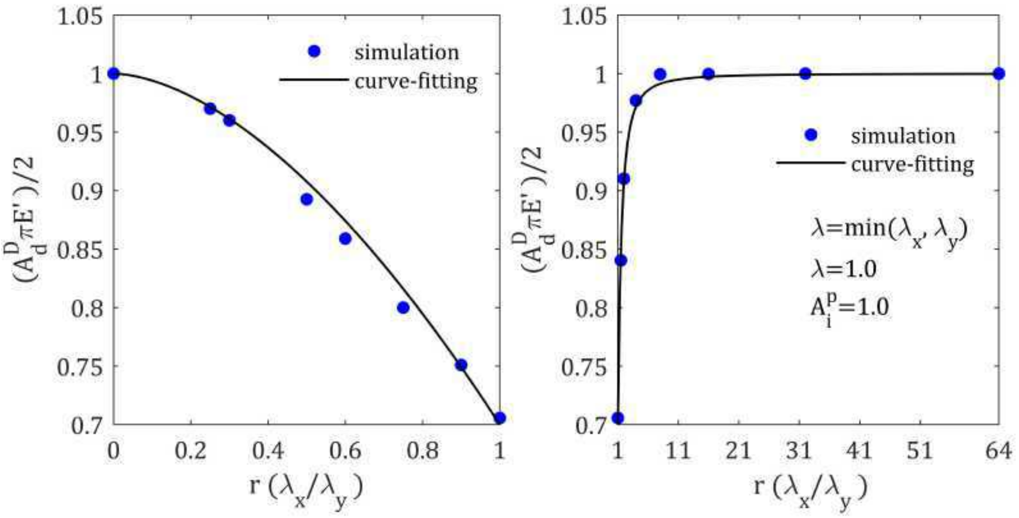

Figure D.4: Amplitude of the elastic deformation A_d^D as a function of anisotropy parameter $r = \lambda_x / \lambda_y$.

Combing Equation D.6, Equation D.7, Equation D.8 and Equation D.9, the relation between the initial amplitude of pressure A_i^p and the corresponding elastic deformation A_d^D is:

$$A_i^p = \frac{\pi E'}{2k(r)\lambda} A_d^D \tag{D.10}$$

with $\lambda = \min(\lambda_x, \lambda_y)$ and

$$k(r) = \begin{cases} -0.3r^{1.7} + 1.0, & \text{if } 0 \leqslant r \leqslant 1 \\ -0.3r^{-1.7} + 1.0, & r > 1 \end{cases}$$

where $r = \lambda_x / \lambda_y$.

Acknowledgments

To all those people who have supported me in carrying out my PhD study.

Firstly, I would like to express my sincere gratitude to my supervisor Professor Antonius Lubrecht for his guidance, encouragement and support of this research work. I would also like to thank my supervisor for opportunities I have been given to participate in scientific conferences as well as two months academic exchanges. Meanwhile, I am very grateful to my supervisor for caring my life in Lyon. During these three years, my supervisor has taught me more than this specific subject, he has taught me how to think more logically and how to solve problems more efficiently. Without his persistent help, this work would not have materialized.

I would also like to extend my thanks to Professor Cornelis Venner and his group for their warmly welcome and help in the MultiGrid method studying and the first manuscript writing during the period I have visited the University of Twente. I also want to thank my friends: Mr. Haichao Liu, Mr. Balan Ramani and Mrs. Xiaozhen He for their help when I was in the University of Twente. Special thanks to Mr. Binbin Zhang for taking care of me in Enschede.

I would like to show my appreciations to my colleagues: Dr. Romain Bugnicourt, Mr. Martin Denni, Ms. Simona Dahdah and Ms. Marjolaine Gonon-Caux. With them, we built a pleasant and friendly working environment. I would like to offer my special thanks to Dr. Marie-Pierre Noutary for teaching me the coarse grid construction method. I also thankful to Dr. Nans Biboulet for his time and advice of my work. I would like to thank the members of the secretary group of LaMCoS for their help over the last three years.

Thanks to my following dear friends with whom I spent a happy time: Ms. Jing Lu, Ms. Pei Niu, Mr. Minhu Lv, Dr. Xiaoyang Zhu, Mr. Minyang Lou et al. I would especially like to thank Dr. Hanfeng Gu and Dr. Teng Zhang, for their selfless help when I first came to Lyon.

This research work is financially supported by the China Scholarship Council (CSC).

Finally, my deepest appreciation goes to my parents: Mr. Ming Zhang and Mrs. Shulan Zeng. Meanwhile, I also thank my boyfriend for his support and waiting.

Thank you for all of you again.

Bibliography

[1] K. Holmberg, P. Andersson, and A. Erdemir, “Global energy consumption due to friction in passenger cars,” *Tribology International*, vol. 47, pp. 221–234, 2012.

[2] K. Holmberg, R. Siilasto, T. Laitinen, P. Andersson, and A. Jäsberg, “Global energy consumption due to friction in paper machines,” *Tribology International*, vol. 62, pp. 58–77, 2013.

[3] K. Holmberg, P. Andersson, N.-O. Nylund, K. Mäkelä, and A. Erdemir, “Global energy consumption due to friction in trucks and buses,” *Tribology International*, vol. 78, pp. 94–114, 2014.

[4] K. Holmberg, P. Kivikytö-Reponen, P. Härkisaari, K. Valtonen, and A. Erdemir, “Global energy consumption due to friction and wear in the mining industry,” *Tribology International*, vol. 115, pp. 116–139, 2017.

[5] P. M. Lee and R. Carpick, “Tribological opportunities for enhancing america’s energy efficiency.,” Tech. Rep. DE-AR00282, A Report to the Advanced Research Project Agency-Energy (ARPA-E) at the U.S. Department of Energy, 2017.

[6] K. Holmberg and A. Erdemir, “Global impact of friction on energy consumption, economy and environment,” *FME Trans*, vol. 43, no. 3, pp. 181–5, 2015.

[7] K. Holmberg and A. Erdemir, “Influence of tribology on global energy consumption, costs and emissions,” *Friction*, vol. 5, no. 3, pp. 263–284, 2017.

[8] V. W. Wong and S. C. Tung, “Overview of automotive engine friction and reduction trends–effects of surface, material, and lubricant-additive technologies,” *Friction*, vol. 4, no. 1, pp. 1–28, 2016.

[9] P. M. Lugt and G. E. Morales-Espejel, “A review of elasto-hydrodynamic lubrication theory,” *Tribology Transactions*, vol. 54, no. 3, pp. 470–496, 2011.

[10] C. H. Venner and A. A. Lubrecht, *Multi-Level Methods in Lubrication*. Elsevier, 2000.

[11] D. Dowson and G. R. Higginson, “A numerical solution to the elasto-hydrodynamic problem,” *Journal of Mechanical Engineering Science*, vol. 1, no. 1, pp. 6–15, 1959.

[12] R. Wolff and A. Kubo, “The application of newton-raphson method to thermal elastohydrodynamic lubrication of line contacts,” *Journal of tribology*, vol. 116, no. 4, pp. 733–740, 1994.

[13] E. Nurgat, M. Berzins, and L. Scales, “Solving ehl problems using iterative, multigrid, and homotopy methods,” *Journal of tribology*, vol. 121, no. 1, pp. 28–33, 1999.

[14] K. P. Oh and S. M. Rohde, “Numerical solution of the point contact problem using the finite element method,” *International Journal for Numerical Methods in Engineering*, vol. 11, no. 10, pp. 1507–1518, 1977.

[15] A. A. Lubrecht, W. E. Ten Napel, and R. Bosma, “Multigrid, an alternative method for calculating film thickness and pressure profiles in elastohydrodynamically lubricated line contacts,” *Journal of tribology*, vol. 108, no. 4, pp. 551–556, 1986.

[16] A. A. Lubrecht, W. E. Ten Napel, and R. Bosma, "Multigrid, an alternative method of solution for two-dimensional elastohydrodynamically lubricated point contact calculations," *Journal of tribology*, vol. 109, no. 3, pp. 437–443, 1987.

[17] T. Almqvist and R. Larsson, "The navier–stokes approach for thermal ehl line contact solutions," *Tribology International*, vol. 35, no. 3, pp. 163–170, 2002.

[18] Q. J. Wang and Y.-W. Chung, eds., *History of EHL Development*, pp. 1684–1684. Boston, MA: Springer US, 2013.

[19] H. Christensen and K. Tonder, "The hydrodynamic lubrication of rough bearing surfaces of finite width," *Journal of Lubrication Technology*, vol. 93, no. 3, pp. 324–329, 1971.

[20] H. Christensen, "Some aspects of the functional influence of surface roughness in lubrication," *Wear*, vol. 17, no. 2, pp. 149–162, 1971.

[21] N. Patir and H. Cheng, "An average flow model for determining effects of three-dimensional roughness on partial hydrodynamic lubrication," *Journal of lubrication Technology*, vol. 100, no. 1, pp. 12–17, 1978.

[22] N. Patir and H. Cheng, "Application of average flow model to lubrication between rough sliding surfaces," *Journal of Lubrication Technology*, vol. 101, no. 2, pp. 220–229, 1979.

[23] J. Tripp, "Surface roughness effects in hydrodynamic lubrication: the flow factor method," *Journal of lubrication technology*, vol. 105, no. 3, pp. 458–463, 1983.

[24] Y. Hu and L. Zheng, "Some aspects of determining the flow factors," *Journal of tribology*, vol. 111, no. 3, pp. 525–531, 1989.

[25] L. Lunde and K. Tonder, "Pressure and shear flow in a rough hydrodynamic bearing, flow factor calculation," *Journal of tribology*, vol. 119, no. 3, pp. 549–555, 1997.

[26] D. Zhu and H. Cheng, "Effect of surface roughness on the point contact ehl," *Journal of tribology*, vol. 110, no. 1, pp. 32–37, 1988.

[27] S. R. Harp and R. F. Salant, "An average flow model of rough surface lubrication with inter-asperity cavitation," *Journal of Tribology*, vol. 123, no. 1, pp. 134–143, 2001.

[28] G. Bayada, V. Carlos, *et al.*, "An average flow model of the reynolds roughness including a mass-flow preserving cavitation model," *Journal of Tribology*, vol. 127, no. 4, pp. 793–802, 2005.

[29] N. Letalleur, F. Plouraboueé, and M. Prat, "Average flow model of rough surface lubrication: flow factors for sinusoidal surfaces," *Journal of tribology*, vol. 124, no. 3, pp. 539–546, 2002.

[30] F. Sahlin, A. Almqvist, R. Larsson, and S. Glavatskih, "Rough surface flow factors in full film lubrication based on a homogenization technique," *Tribology International*, vol. 40, no. 7, pp. 1025–1034, 2007.

[31] P. Goglia, T. Conry, and C. Cusano, "The effects of surface irregularities on the elastohydrodynamic lubrication of sliding line contacts. part i—single irregularities," *Journal of Tribology*, vol. 106, no. 1, pp. 104–112, 1984.

[32] P. Goglia, C. Cusano, and T. Conry, “The effects of surface irregularities on the elastohydrodynamic lubrication of sliding line contacts. part ii—wavy surfaces,” *Journal of Tribology*, vol. 106, no. 1, pp. 113–119, 1984.

[33] L. G. Houpert and B. J. Hamrock, “Elastohydrodynamic lubrication calculations used as a tool to study scuffing,” *Proceedings of the 12th Leeds-Lyon Symposium on Tribology, Tribology Series*, pp. 146–155, 1985.

[34] C. H. Venner and W. E. Ten Napel, “Surface roughness effects in an ehl line contact,” *Journal of tribology*, vol. 114, no. 3, pp. 616–622, 1992.

[35] C. Hooke, “The behaviour of low-amplitude surface roughness under line contacts,” *Proceedings of the Institution of Mechanical Engineers, Part J: Journal of Engineering Tribology*, vol. 213, no. 4, pp. 275–285, 1999.

[36] A. A. Lubrecht, “The numerical solution of the elastohydrodynamically lubricated line- and point contact problem using multigrid techniqes,” *PhD. Thesis, University of Twente*, 1987.

[37] A. A. Lubrecht, W. Ten Napel, and R. Bosma, “The influence of longitudinal and transverse roughness on the elastohydrodynamic lubrication of circular contacts,” *Journal of tribology*, vol. 110, no. 3, pp. 421–426, 1988.

[38] C. Kweh, H. Evans, and R. Snidle, “Micro-elastohydrodynamic lubrication of an elliptical contact with transverse and three-dimensional sinusoidal roughness,” *Journal of Tribology*, vol. 111, no. 4, pp. 577–584, 1989.

[39] C. C. Kweh, M. Patching, H. Evans, and R. Snidle, “Simulation of elastohydrodynamic contacts between rough surfaces,” *Journal of tribology*, vol. 114, no. 3, pp. 412–419, 1992.

[40] X. Ai and H. S. Cheng, “A transient ehl analysis for line contacts with measured surface roughness using multigrid technique,” *Journal of tribology*, vol. 116, no. 3, pp. 549–556, 1994.

[41] L. Chang, M. Webster, and A. Jackson, “On the pressure rippling and roughness deformation in elastohydrodynamic lubrication of rough surfaces,” *Journal of tribology*, vol. 115, no. 3, pp. 439–444, 1993.

[42] L. Chang and M. Webster, “A study of elastohydrodynamic lubrication of rough surfaces,” *Journal of Tribology*, vol. 113, no. 1, pp. 110–115, 1991.

[43] J. Greenwood and K. Johnson, “The behaviour of transverse roughness in sliding elastohydrodynamically lubricated contacts,” *Wear*, vol. 153, no. 1, pp. 107–117, 1992.

[44] J. Greenwood and G. Morales-Espejel, “The behaviour of transverse roughness in ehl contacts,” *Proceedings of the Institution of Mechanical Engineers, Part J: Journal of Engineering Tribology*, vol. 208, no. 2, pp. 121–132, 1994.

[45] A. A. Lubrecht and C. H. Venner, “Aspects of two-sided surface waviness in an ehl line contact,” *Tribology Series*, vol. 25, pp. 205–205, 1993.

[46] G. E. Morales Espejel, *Elastohydrodynamic lubrication of smooth and rough surfaces*. PhD thesis, University of Cambridge, 1993.

[47] K. F. Osborn and F. Sadeghi, "Time dependent line ehd lubrication using the multigrid/multilevel technique," *Journal of tribology*, vol. 114, no. 1, pp. 68–74, 1992.

[48] C. H. Venner, A. A. Lubrecht, and W. E. Ten Napel, "Numerical simulation of the overrolling of a surface feature in an ehl line contact," *Journal of tribology*, vol. 113, no. 4, pp. 777–783, 1991.

[49] C. H. Venner, *Multilevel solution of the EHL line and point contact problems.* PhD thesis, Netherlands, 1991.

[50] C. H. Venner and A. A. Lubrecht, "Numerical simulation of a transverse ridge in a circular ehl contact under rolling/sliding," *Journal of tribology*, vol. 116, no. 4, pp. 751–761, 1994.

[51] C. H. Venner and A. A. Lubrecht, "Numerical simulation of waviness in a circular ehl contact, under rolling/sliding," in *Tribology Series*, vol. 30, pp. 259–272, Elsevier, 1995.

[52] C. H. Venner, F. Couhier, A. A. Lubrecht, and J. A. Greenwood, "Amplitude reduction of waviness in transient ehl line contacts," *Tribology Series*, vol. 32, pp. 103–112, 1997.

[53] C. H. Venner and A. A. Lubrecht, "Amplitude reduction of non-isotropic harmonic patterns in circular ehl contacts, under pure rolling," in *Tribology Series*, vol. 36, pp. 151–162, Elsevier, 1999.

[54] A. A. Lubrecht, D. Graille, C. H. Venner, and J. A. Greenwood, "Waviness amplitude reduction in ehl line contacts under rolling-sliding," *Journal of tribology*, vol. 120, no. 4, pp. 705–709, 1998.

[55] C. H. Venner and G. E. Morales-Espejel, "Amplitude reduction of small-amplitude waviness in transient elastohydrodynamically lubricated line contacts," *Proceedings of the Institution of Mechanical Engineers, Part J: Journal of Engineering Tribology*, vol. 213, no. 6, pp. 487–504, 1999.

[56] A. A. Lubrecht and C. H. Venner, "Elastohydrodynamic lubrication of rough surfaces," *Proceedings of the institution of mechanical engineers, Part J: Journal of Engineering Tribology*, vol. 213, no. 5, pp. 397–404, 1999.

[57] B. Jacod, P. M. Lugt, M. L. Dumont, J. H. Tripp, and C. H. Venner, "Amplitude reduction of waviness in elastohydrodynamic lubrication using an eyring fluid model," *Proceedings of the Institution of Mechanical Engineers, Part J: Journal of Engineering Tribology*, vol. 214, no. 4, pp. 343–350, 2000.

[58] C. H. Venner and A. A. Lubrecht, "An engineering tool for the quantitative prediction of general roughness deformation in ehl contacts based on harmonic waviness attenuation," *Proceedings of the Institution of Mechanical Engineers, Part J: Journal of Engineering Tribology*, vol. 219, no. 5, pp. 303–312, 2005.

[59] A. D. Chapkov, C. H. Venner, and A. A. Lubrecht, "Roughness amplitude reduction under non-newtonian ehd lubrication conditions," *Journal of tribology*, vol. 128, no. 4, pp. 753–760, 2006.

[60] J. Wang, C. H. Venner, and A. A. Lubrecht, "Amplitude reduction in ehl line contacts under rolling sliding conditions," *Tribology international*, vol. 44, no. 12, pp. 1997–2001, 2011.

[61] P. Šperka, I. Křupka, and M. Hartl, "Experimental study of real roughness attenuation in concentrated contacts," *Tribology International*, vol. 43, no. 10, pp. 1893–1901, 2010.

[62] M. Holmes, H. P. Evans, T. G. Hughes, and R. W. Snidle, "Transient elastohydrodynamic point contact analysis using a new coupled differential deflection method part 1: theory and validation," *Proceedings of the Institution of Mechanical Engineers, Part J: Journal of Engineering Tribology*, vol. 217, no. 4, pp. 289–304, 2003.

[63] H. P. Evans, R. W. Snidle, and K. J. Sharif, "Deterministic mixed lubrication modelling using roughness measurements in gear applications," *Tribology International*, vol. 42, no. 10, pp. 1406–1417, 2009.

[64] Y. Zhang, H. Liu, C. Zhu, C. Song, and Z. Li, "Influence of lubrication starvation and surface waviness on the oil film stiffness of elastohydrodynamic lubrication line contact," *Journal of Vibration and Control*, vol. 24, no. 5, pp. 924–936, 2018.

[65] Z. Gu, C. Zhu, H. Liu, and X. Du, "A comparative study of tribological performance of helical gear pair with various types of tooth surface finishing," *Industrial Lubrication and Tribology*, 2018.

[66] R. E. Alcouffe, A. Brandt, J. E. Dendy, Jr, and J. W. Painter, "The multi-grid method for the diffusion equation with strongly discontinuous coefficients," *SIAM Journal on Scientific and Statistical Computing*, vol. 2, no. 4, pp. 430–454, 1981.

[67] A. Crook, "The lubrication of rollers iv. measurements of friction and effective viscosity," *Phil. Trans. R. Soc. Lond. A*, vol. 255, no. 1056, pp. 281–312, 1963.

[68] K. L. Johnson and R. Cameron, "Fourth paper: shear behaviour of elastohydrodynamic oil films at high rolling contact pressures," *Proceedings of the Institution of Mechanical Engineers*, vol. 182, no. 1, pp. 307–330, 1967.

[69] K. L. Johnson and A. D. Roberts, "Observations of viscoelastic behaviour of an elastohydrodynamic lubricant film," *Proc. R. Soc. Lond. A*, vol. 337, no. 1609, pp. 217–242, 1974.

[70] C. R. Evans and K. L. Johnson, "Regimes of traction in elastohydrodynamic lubrication," *Proceedings of the Institution of Mechanical Engineers, Part C: Journal of Mechanical Engineering Science*, vol. 200, no. 5, pp. 313–324, 1986.

[71] Z. Zhang, X. Qiu, and Y. Hong, "Ehl analysis of rib-roller end contact in tapered roller bearings," *Tribology transactions*, vol. 31, no. 4, pp. 461–467, 1988.

[72] H. Yu and J. B. Medley, "Influence of lubricant additives on friction in a disc machine," *Tribology Series*, vol. 32, pp. 475–486, 1997.

[73] B. Jacod, C. H. Venner, and P. M. Lugt, "A generalized traction curve for ehl contacts," *Journal of tribology*, vol. 123, no. 2, pp. 248–253, 2001.

[74] J. De Vicente, J. R. Stokes, and H. A. Spikes, "The frictional properties of newtonian fluids in rolling–sliding soft-ehl contact," *Tribology Letters*, vol. 20, no. 3-4, pp. 273–286, 2005.

[75] H. Liu, C. Zhu, Z. Sun, and C. Song, "Starved lubrication of a spur gear pair," *Tribology International*, vol. 94, pp. 52–60, 2016.

[76] M. Björling, K. Berglund, A. Spencer, and R. Larsson, "The effect of ageing on elastohydrodynamic friction in heavy-duty diesel engine oils," *Proceedings of the Institution of Mechanical Engineers, Part J: Journal of Engineering Tribology*, vol. 231, no. 6, pp. 708–715, 2017.

[77] J. Zhang, A. Tan, and H. Spikes, “Effect of base oil structure on elastohydrodynamic friction,” *Tribology Letters*, vol. 65, no. 1, p. 13, 2017.

[78] W. C. Emmens, “The influence of surface roughness on friction,” in *International Conference on Controlling Sheet Metal Forming Processes, Michigan*, pp. 63–70, 1988.

[79] S. Wu and H. S. Cheng, “A friction model of partial-ehl contacts and its application to power loss in spur gears,” *Tribology Transactions*, vol. 34, no. 3, pp. 398–407, 1991.

[80] B. H. Lee, Y. T. Keum, and R. H. Wagoner, “Modeling of the friction caused by lubrication and surface roughness in sheet metal forming,” *Journal of materials processing technology*, vol. 130, pp. 60–63, 2002.

[81] R. H. Thurston, *Friction and Lubrication: Determinations of the Laws and Coëfficients of Friction by New Methods and with New Apparatus.* Railroad gazette, 1879.

[82] D. Dowson, *History of tribology.* Addison-Wesley Longman Limited, 1979.

[83] R. Stribeck, “Die wesentlichen eigenschaften der gleit-und rollenlager,” *Zeitschrift des Vereines Deutscher Ingenieure*, vol. 46, pp. 1341–1348, 1902.

[84] R. Stribeck and M. Schröter, *Die wesentlichen Eigenschaften der Gleit-und Rollenlager: Untersuchung einer Tandem-Verbundmaschine von 1000 PS.* Springer, 1903.

[85] L. Gümbel, “Das problem der lagerreibung,” *Mbl. Berlin. Bez. Ver. dtsch. Ing*, vol. 5, 1914.

[86] M. D. Hersey, “The laws of lubrication of horizontal journal bearings,” *Journal of the Washington Academy of Sciences*, vol. 4, no. 19, pp. 542–552, 1914.

[87] R. E. Wilson and D. P. Barnard, “The mechanism of lubrication,” in *SAE Technical Paper*, SAE International, 1922.

[88] S. A. McKee, “The effect of running-in on journal bearing performance,” *Mech. Eng*, vol. 49, pp. 1335–1340, 1927.

[89] G. Vogelpohl, “Die stribeck-kurve als kennzeichen des allgemeinen reibungsverhaltens geschmierter gleitflächen,” *Z. VDI*, vol. 96, no. 9, pp. 261–68, 1954.

[90] K. L. Johnson, “Regimes of elastohydrodynamic lubrication,” *Journal of Mechanical Engineering Science*, vol. 12, no. 1, pp. 9–16, 1970.

[91] H. A. Spikes, “Mixed lubrication—an overview,” *Lubrication Science*, vol. 9, no. 3, pp. 221–253, 1997.

[92] B. A. Shotter, “Experiments with a disc machine to determine the possible influence of surface finish on gear tooth performance,” in *Proc. Int. Conf. Gearing*, vol. 120, Instn Mech. Engrs London, 1958.

[93] T. E. Tallian, Y. P. Chiu, D. F. Huttenlocher, J. A. Kamenshine, L. B. Sibley, and N. E. Sindlinger, “Lubricant films in rolling contact of rough surfaces,” *ASLE TRANSACTIONS*, vol. 7, no. 2, pp. 109–126, 1964.

[94] T. E. Tallian, J. I. McCool, and L. B. Sibley, “Paper 14: Partial elastohydrodynamic lubrication in rolling contact,” in *Proceedings of the Institution of Mechanical Engineers, Conference Proceedings*, vol. 180, pp. 169–186, SAGE Publications Sage UK: London, England, 1965.

[95] S. Y. Poon and D. J. Haines, “Third paper: frictional behaviour of lubricated rolling-contact elements,” *Proceedings of the Institution of Mechanical Engineers*, vol. 181, no. 1, pp. 363–389, 1966.

[96] S. Bair and W. O. Winer, “Regimes of traction in concentrated contact lubrication,” *Journal of Lubrication Technology*, vol. 104, no. 3, pp. 382–386, 1982.

[97] G. Stachowiak and A. W. Batchelor, *Engineering tribology*. Butterworth-Heinemann, 2013.

[98] P. M. Cann, E. Ioannides, B. Jacobson, and A. Lubrecht, “The lambda ratio—a critical re-examination,” *Wear*, vol. 175, no. 1-2, pp. 177–188, 1994.

[99] D. J. Schipper and A. De Gee, “On the transitions in the lubrication of concentrated contacts,” *Journal of tribology*, vol. 117, no. 2, pp. 250–254, 1995.

[100] E. Gelinck and D. J. Schipper, “Calculation of stribeck curves for line contacts,” *Tribology International*, vol. 33, no. 3-4, pp. 175–181, 2000.

[101] K. L. Johnson, J. A. Greenwood, and S. Y. Poon, “A simple theory of asperity contact in elastohydro-dynamic lubrication,” *Wear*, vol. 19, no. 1, pp. 91–108, 1972.

[102] X. Lu, M. M. Khonsari, and E. R. Gelinck, “The stribeck curve: experimental results and theoretical prediction,” *Journal of tribology*, vol. 128, no. 4, pp. 789–794, 2006.

[103] W. Wang, S. Wang, F. Shi, Y. Wang, H. Chen, H. Wang, and Y. Hu, “Simulations and measurements of sliding friction between rough surfaces in point contacts: From ehl to boundary lubrication,” *Journal of Tribology*, vol. 129, no. 3, pp. 495–501, 2007.

[104] M. Kalin, I. Velkavrh, and J. Vižintin, “The stribeck curve and lubrication design for non-fully wetted surfaces,” *Wear*, vol. 267, no. 5-8, pp. 1232–1240, 2009.

[105] M. Kalin and I. Velkavrh, “Non-conventional inverse-stribeck-curve behaviour and other characteristics of dlc coatings in all lubrication regimes,” *Wear*, vol. 297, no. 1-2, pp. 911–918, 2013.

[106] X. Zhang, Z. Li, and J. Wang, “Friction prediction of rolling-sliding contact in mixed ehl,” *Measurement*, vol. 100, pp. 262–269, 2017.

[107] J. Bonaventure, J. Cayer-Barrioz, and D. Mazuyer, “Transition between mixed lubrication and elastohydrodynamic lubrication with randomly rough surfaces,” *Tribology Letters*, vol. 64, no. 3, p. 44, 2016.

[108] D. Dowson, J. F. Dunn, and C. M. Taylor, “The piezo-viscous fluid, rigid solid regime of lubrication,” *Proceedings of the Institution of Mechanical Engineers, Part C: Journal of Mechanical Engineering Science*, vol. 197, no. 1, pp. 43–52, 1983.

[109] T. D. Jacobs, T. Junge, and L. Pastewka, “Quantitative characterization of surface topography using spectral analysis,” *Surface Topography: Metrology and Properties*, vol. 5, no. 1, p. 013001, 2017.

[110] C. H. Venner, W. E. t. ten Napel, and R. Bosma, “Advanced multilevel solution of the ehl line contact problem,” *Journal of Tribology*, vol. 112, no. 3, pp. 426–431, 1990.

[111] C. H. Venner, “Higher-order multilevel solvers for the ehl line and point contact problem,” *Journal of tribology*, vol. 116, no. 4, pp. 741–750, 1994.

[112] C. H. Venner and A. A. Lubrecht, “Multigrid techniques: a fast and efficient method for the numerical simulation of elastohydrodynamically lubricated point contact problems,” *Proceedings of the Institution of Mechanical Engineers, Part J: Journal of Engineering Tribology*, vol. 214, no. 1, pp. 43–62, 2000.

[113] A. A. Lubrecht and E. Ioannides, “A fast solution of the dry contact problem and the associated sub-surface stress field, using multilevel techniques,” *Journal of tribology*, vol. 113, no. 1, pp. 128–133, 1991.

[114] D. Dowson and G. R. Higginson, “Elasto-hydrodynamic lubrication: the fundamentals of roller and gear lubrication. vol. 23,” 1966.

[115] C. Barus, “Isothermals, isopiestics and isometrics relative to viscosity,” *American Journal of Science (1880-1910)*, vol. 45, no. 266, p. 87, 1893.

[116] C. J. A. Roelands, “Correlational aspects of the viscosity-temperature-pressure relationship of lubricating oils,” *Doctoral thesis, Technische Hogeschool te Delt*, 1966.

[117] K. L. Johnson, *Contact Mechanics.* Cambridge university press, 1987.

[118] H. Moes, “Discussion on a contribution by K. Jakobsen and H. Christensen,” *Proc. Inst. Mech. Eng., Part J: J. Eng. Tribol*, vol. 183, no. 3, pp. 205–206, 1969.

[119] H. Moes and R. Bosma, “Design charts for optimum bearing configurations: 1—the full journal bearing,” *Journal of Lubrication Technology*, vol. 93, no. 2, pp. 302–305, 1971.

[120] B. J. Hamrock and D. Dowson, “Isothermal elastohydrodynamic lubrication of point contacts: Part 1—theoretical formulation,” *Journal of Lubrication Technology*, vol. 98, no. 2, pp. 223–228, 1976.

[121] K. F. Riley, M. P. Hobson, and S. J. Bence, “Mathematical methods for physics and engineering,” 1999.

[122] W. McGuire, R. H. Gallagher, and R. D. Ziemian, *Matrix structural analysis.* 2000.

[123] M.-P. Noutary, N. Biboulet, and A. A. Lubrecht, “A robust piston ring lubrication solver: Influence of liner groove shape, depth and density,” *Tribology International*, vol. 100, pp. 35–40, 2016.

[124] M.-P. Noutary, *A robust Reynolds solver for textured surfaces in the piston ring cylinder liner contact.* Theses, Université de Lyon, Nov. 2017.

[125] A. Ponjavic, *Local rheology of lubricants in the elastohydrodynamic regime.* PhD thesis, Imperial College London, 2014.

[126] A. V. Olver and H. A. Spikes, “Prediction of traction in elastohydrodynamic lubrication,” *Proceedings of the Institution of Mechanical Engineers, Part J: Journal of Engineering Tribology*, vol. 212, no. 5, pp. 321–332, 1998.

[127] S. Bair and W. O. Winer, “The high pressure high shear stress rheology of liquid lubricants,” *Journal of tribology*, vol. 114, no. 1, pp. 1–9, 1992.

[128] S. Bair, "Shear thinning correction for rolling/sliding elastohydrodynamic film thickness," *Proceedings of the Institution of Mechanical Engineers, Part J: Journal of Engineering Tribology*, vol. 219, no. 1, pp. 69–74, 2005.

[129] P. Kumar, M. M. Khonsari, and S. Bair, "Full ehl simulations using the actual ree-eyring model for shear-thinning lubricants," *Journal of Tribology*, vol. 131, no. 1, p. 011802, 2009.

[130] S. Bair, "The rheological assumptions of classical ehl: What went wrong?," *Tribology International*, vol. 131, pp. 45–50, 2019.

[131] K. L. Johnson and J. L. Tevaarwerk, "Shear behaviour of elastohydrodynamic oil films," *Proceedings of the Royal Society of London. A. Mathematical and Physical Sciences*, vol. 356, no. 1685, pp. 215–236, 1977.

[132] S. Huge and J. Zhang, "History, origins and prediction of elastohydrodynamic friction," *Tribology Letters*, vol. 56, no. 1, pp. 1–25, 2014.

[133] S. Bair and W. O. Winer, "A rheological model for elastohydrodynamic contacts based on primary laboratory data," *Journal of Lubrication Technology*, vol. 101, no. 3, pp. 258–264, 1979.

[134] K. Yasuda, R. C. Armstrong, and R. E. Cohen, "Shear flow properties of concentrated solutions of linear and star branched polystyrenes," *Rheologica Acta*, vol. 20, pp. 163–178, Mar 1981.

[135] R.-T. Lee and B. Hamrock, "A circular non-newtonian fluid model: Part i—used in elastohydrodynamic lubrication," *Journal of Tribology*, vol. 112, no. 3, pp. 486–495, 1990.

[136] S. Bair, "The actual eyring models for thixotropy and shear-thinning: Experimental validation and application to ehd," in *ASME/STLE 2004 International Joint Tribology Conference*, pp. 439–445, American Society of Mechanical Engineers, 2004.

[137] P. Kumar and M. M. Khonsari, "On the role of lubricant rheology and piezo-viscous properties in line and point contact ehl," *Tribology International*, vol. 42, no. 11-12, pp. 1522–1530, 2009.

[138] H. Rahnejat, *Tribology and dynamics of engine and powertrain: fundamentals, applications and future trends*. Elsevier, 2010.

[139] S. Wen and P. Huang, *Principles of tribology*. John Wiley & Sons, 2012.

[140] J. Bonaventure, *Influence of random surface roughness on friction in elastohydrodynamic, mixed and boundary lubrication*. PhD thesis, Lyon, 2017.

[141] C. R. Evans, *Measurement and mapping of the rheological properties of elastohydrodynamic lubricants*. PhD thesis, University of Cambridge, 1984.

[142] B. Bhushan, *Modern tribology handbook, two volume set*. CRC press, 2000.

[143] J. C. Stover, *Optical scattering: measurement and analysis*, vol. 2. SPIE optical engineering press Bellingham, 1995.

[144] A.-L. Barabási and H. E. Stanley, *Fractal concepts in surface growth*. Cambridge university press, 1995.

[145] B. Persson, O. Albohr, U. Tartaglino, A. Volokitin, and E. Tosatti, “On the nature of surface roughness with application to contact mechanics, sealing, rubber friction and adhesion,” *Journal of physics: Condensed matter*, vol. 17, no. 1, p. R1, 2004.

[146] P. R. Nayak, “Random process model of rough surfaces,” *Journal of Lubrication Technology*, vol. 93, no. 3, pp. 398–407, 1971.

[147] D. J. Schipper, “Transitions in the lubrication of concentrated contacts, 1988,” *University of Twente: Enschede, The Netherlands*, p. 194, 1988.

FOLIO ADMINISTRATIF

THESE DE L'UNIVERSITE DE LYON OPEREE AU SEIN DE L'INSA LYON

NOM : ZHANG

DATE de SOUTENANCE : 05/09/2019

Prénoms : Yuanyuan

TITRE : La prédiction du frottement des surfaces rugueuses dans un contact avec lubrification élastohydrodynamique

NATURE : Doctorat

Numéro d'ordre : 2019LYSEI063

Ecole doctorale : Mécanique, Energétique, Génie Civil, Acoustique (MEGA)

Spécialité : Génie Mécanique

RESUME :

Le frottement à l'interface des surfaces influence les performances des éléments mécaniques. Le frottement a été étudié expérimentalement dans la plupart des études. Dans ce travail, le frottement est prédit à l'aide d'une simulation numérique dans des conditions de contact rugueux avec une lubrification élastohydrodynamique (EHL). La technique classique Multigrille fonctionne bien pour limiter le temps de calcul et les besoins en mémoire. Cependant, le choix de la grille grossière a une influence importante sur la robustesse du code et son efficacité pour résoudre le problème brut. Dans la première partie de ce travail, une méthode de construction de grille grossière proposée par Alcouffe et al. est implémenté dans le code EHL Multigrille indépendamment du temps. Ensuite ce solveur modifié est étendu aux cas transitoires pour résoudre le problème de contact avec rugosité.
La courbe de frottement est généralement représentée en fonction du « λ ratio », le rapport entre l'épaisseur du film d'huile et la valeur moyenne quadratique de la rugosité de la surface. Cependant, ce paramètre est moins approprié pour tracer les variations de frottement dans des conditions de haute pression (régime élasto piézo-visqueux). Dans la deuxième partie de ce travail, le coefficient de frottement est calculé à l'aide du code EHL modifié pour de nombreuses conditions de fonctionnement ainsi que pour les paramètres d'ondulation de surface. Les résultats de la simulation montrent qu'il n'y a pas de courbe de frottement unique lorsque l'ancien paramètre « λ ratio » est utilisé. En se basant sur la théorie de la réduction d'amplitude, un nouveau paramètre de dimensionnement qui dépend des conditions de fonctionnement et des paramètres d'ondulation est trouvé, ce qui peut donner une courbe de frottement unique pour les situations de haute pression.
Le nouveau paramètre d'échelle et l'augmentation du frottement prédite par la méthode PSD montrent une bonne précision technique pour une utilisation pratique.

MOTS-CLÉS : Lubrification élastohydrodynamique, Simulation numérique, Régime élasto piézo-visqueux, Théorie de réduction d'amplitude, Variation de frottement

Laboratoire (s) de recherche : Laboratoire de Mécanique des Contacts et des Structures
UMR CNRS 5259 - INSA de Lyon
Bâtiment Sophie Germain
Avenue Jean Capelle
69621 Villeurbanne Cedex FRANCE

Directeur de thèse: LUBRECHT Antonius. A

Président de jury : CAYER-BARRIOZ Juliette

Composition du jury :
EVANS Pwt
VENNER Cornelis. H
BIBOULET Nans
KŘUPKA Ivan
CAYER-BARRIOZ Juliette
LUBRECHT Antonius. A